VOLUME 30 MAY 1952 NUMBER 3

Canadian Journal of Physics

Editor: G. M. VOLKOFF

Published by THE NATIONAL RESEARCH COUNCIL
OTTAWA CANADA

CANADIAN JOURNAL OF PHYSICS

(*Formerly Section A, Canadian Journal of Research*)

The CANADIAN JOURNAL OF PHYSICS is published bimonthly by the National Research Council of Canada under the authority of the Chairman of the Committee of the Privy Council on Scientific and Industrial Research. Matters of general policy are the responsibility of a joint Editorial Board consisting of members of the National Research Council of Canada and the Royal Society of Canada.

The National Research Council of Canada publishes also: *Canadian Journal of Botany, Canadian Journal of Chemistry, Canadian Journal of Medical Sciences, Canadian Journal of Technology, Canadian Journal of Zoology.*

EDITORIAL BOARD

Representing
NATIONAL RESEARCH COUNCIL

DR. J. H. L. JOHNSTONE (*Chairman*),
Professor of Physics,
Dalhousie University,
Halifax, N.S.

DR. OTTO MAASS,
Macdonald Professor of
Physical Chemistry,
McGill University,
Montreal, P.Q.

DR. CHARLES W. ARGUE,
Dean of Science,
University of New Brunswick,
Fredericton, N.B.

DR. A. G. MCCALLA,
Dean, Faculty of Agriculture,
University of Alberta,
Edmonton, Alta.

Representing
ROYAL SOCIETY OF CANADA

Section III

DR. G. M. VOLKOFF,
Professor of Physics,
University of British Columbia
Vancouver, B.C.

DR. J. W. T. SPINKS,
Dean, College of Graduate
Studies,
University of Saskatchewan,
Saskatoon, Sask.

Section V

DR. H. S. JACKSON,*
Head, Department of Botany,
University of Toronto,
Toronto, Ont.

DR. E. HORNE CRAIGIE,
Department of Zoology,
University of Toronto,
Toronto, Ont.

Ex officio

DR. LÉO MARION, *Editor-in-Chief*,
Director, Division of Pure Chemistry,
National Research Laboratories,
Ottawa.

DR. H. H. SAUNDERSON,
Director, Division of Information Services,
National Research Council,
Ottawa.

Representing
THE CHEMICAL INSTITUTE OF CANADA

DR. H. G. THODE,
Department of Chemistry,
McMaster University,
Hamilton, Ont.

Manuscripts should be addressed to:

DR. LÉO MARION,
Editor-in-Chief,
Canadian Journal of Physics,
National Research Council,
Ottawa, Canada.

Each manuscript should be typewritten, double-spaced, and the original and one extra copy submitted (see **Notice to Contributors,** inside of back cover).

Subscription, renewals, and orders for back numbers should be addressed to:

Administrative Services,
National Research Council,
Ottawa, Canada.

Subscription rate: $3.00 a year; single numbers: 50 cents. Special rates can be obtained for subscriptions to more than one of the Journals published by the National Research Council.

*Deceased.

Canadian Journal of Physics

Issued by THE NATIONAL RESEARCH COUNCIL OF CANADA

VOLUME 30 MAY, 1952 NUMBER 3

GAMMA–NEUTRON REACTIONS IN O^{16} AND N^{14} [1]

BY R. J. HORSLEY,[2] R. N. H. HASLAM, AND H. E. JOHNS

ABSTRACT

The cross sections for the reactions $O^{16}(\gamma, n)O^{15}$ and $N^{14}(\gamma, n)N^{13}$ have been determined by measurement of the induced positron activities. The oxygen cross-section curve has a slowly increasing initial portion after which it rises rapidly to a maximum peak cross section of 11.4 millibarns at 24.0 Mev. The nitrogen cross-section curve has an initial peak at about 13 Mev. Above 17 Mev., this curve increases sharply to a maximum value of 2.84 millibarns at 24 Mev. In order to explain the shape of the nitrogen curve, a relative total neutron yield curve has been determined from 12 to 20 Mev. by detecting the emitted neutrons with a rhodium foil. This neutron yield curve has the same shape as the nitrogen saturated specific activity curve. The anomalous shapes of the nitrogen and oxygen cross-section curves are explained in terms of the variation of gamma-ray absorption with energy.

INTRODUCTION

The cross-section curves for the reactions $N^{14}(\gamma, n)N^{13}$ and $O^{16}(\gamma, n)O^{15}$ have been determined by measuring the induced activities in N^{13} and O^{15} respectively. These results have been published in a previous letter (1). The cross-section curves obtained present rather unusual features and it was thought worthwhile to examine one of these reactions further. This paper reports briefly the initial work and in detail the investigation of the nitrogen cross-section curve by direct detection of the emitted neutrons with a rhodium foil.

EXPERIMENTAL PROCEDURE IN INITIAL EXPERIMENT

One gram samples of ammonium nitrite were irradiated in a small cadmium thimble by the University of Saskatchewan's betatron. The dose was monitored by a Victoreen 100 'r.' chamber placed in the center of an 8 cm. cube of Lucite. The cadmium thimble, which approximates in size the sensitive volume of the 100 'r.' chamber, was also irradiated in the Lucite cube. At energies below the (γ, n) threshold in O^{16} (16.3 Mev.) a pure 10 min. nitrogen activity was obtained. At energies above 16.3 Mev., the 2 min. O^{15} activity was separated from the 10 min. N^{13} activity by analyzing the decay curve. In this way, using ammonium nitrate, values for both the oxygen and nitrogen activation curves could be obtained simultaneously. Activation points for oxygen and nitrogen were also determined by using powdered boric acid and dicyandiamide respectively. All samples were counted in a fixed geometry.

[1] *Manuscript received November 26, 1951.*
Contribution from the Department of Physics, University of Saskatchewan, Saskatoon, Sask.
[2] *Holder of a National Research Council of Canada Studentship.*

RESULTS

Fig. 1 shows the saturated specific activity curves for O^{16} and N^{14} at a dosage rate of 100 r. per minute per gram of parent isotope. Corrections for self-absorption, back-scattering, isotopic abundance, and geometry have been applied. Normalization against the $Cu^{63}(\gamma, n)Cu^{62}$ (2) activity was carried out at 23 Mev. The energy of the betatron is controlled by an integrator–expander circuit (4) and is stabilized to within 0.1 Mev. The counting error is between 1 and 2% except at energies very close to the threshold. The experimental points which determine the relative shapes of the activity curves are thought to be accurate to better

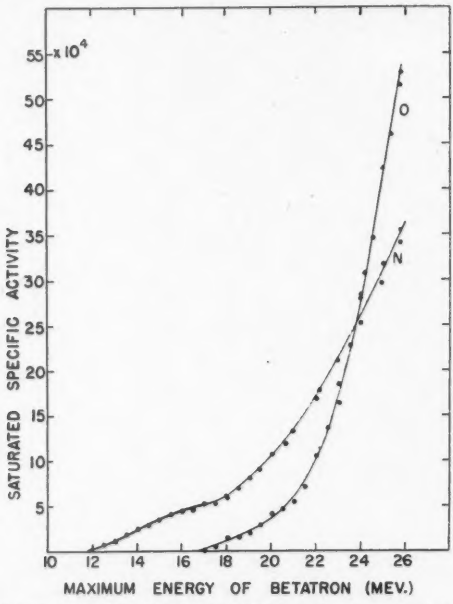

FIG. 1. Saturated activity induced in O^{16} and N^{14} at a dosage rate of 100 r. per minute per gram of parent isotope. Corrections for self-absorption, back-scattering, isotopic abundance, and geometry have been applied.

than 3%. In the normalization against the copper activity, much larger errors may be introduced in correcting for self-absorption. As a result the absolute values as compared to copper may be in error by as much as 20%. The oxygen and nitrogen cross-section curves were determined from the activity curves by the "photon difference" (3) method and are shown in Fig. 2.

The first portions of both cross-section curves show unusual behavior. The oxygen curve has a more slowly increasing initial portion than is normally found and the nitrogen curve has a small apparent peak at about 13 Mev. An explanation of the shape of these curves was offered in the first reference in terms of the variation with energy of electric quadrupole, magnetic dipole, and electric

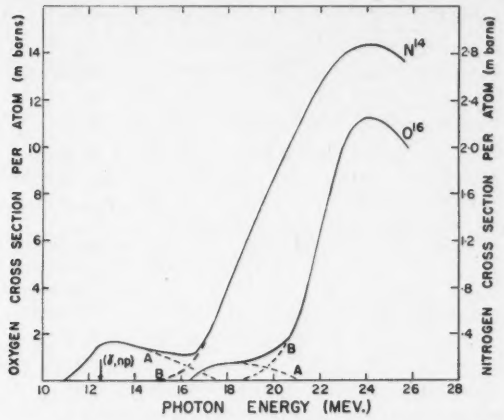

FIG. 2. Cross section vs. photon energy for $N^{14}(\gamma, n)N^{13}$ and $O^{16}(\gamma, n)O^{15}$. The dotted lines marked *A* indicate the falling off of electric quadrupole and magnetic dipole absorption. The dotted lines marked *B* indicate the onset of electric dipole absorption. The threshold for the (γ, np) reaction in N^{14} is indicated.

dipole absorption. The falling off in the nitrogen cross-section curve above 13 Mev., forming an apparent peak, was attributed to a large (γ, np) reaction in nitrogen. However, this dip in the curve could also be explained by the falling off of electric quadrupole and magnetic dipole absorption before the onset of electric dipole absorption as is illustrated in Fig. 2. Here the total cross-section curves have been broken up into components. The first component is attributed to electric quadrupole and magnetic dipole absorption. The second component is attributed to electric dipole absorption.

To decide which explanation is correct for the nitrogen peak at 13 Mev., it was decided to determine the neutron yield from nitrogen as a function of the maximum betatron energy. If the (γ, np) cascade reaction is responsible for the falling off in the nitrogen saturated specific activity curve, the dip should not be present in the neutron yield curve. Since neutrons which originate in both (γ, n) and (γ, np) reactions are detected, a smooth yield curve rising more rapidly than the saturated specific activity curve should be obtained.

EXPERIMENTAL ARRANGEMENT

The experimental arrangement is illustrated in Fig. 3. Three wooden boxes 24 in. square and 12 in. deep were filled with a mixture of paraffin and boric acid. A 6 in. channel was provided to allow the X-ray beam to strike the target without hitting the wax. A $2\frac{1}{4}$ in. diameter opening, running vertically through the center of the middle container, permits neutrons emitted from the target to reach the detector directly. The detector consists of a Victoreen thyrode counter enclosed by a 5 cm. sleeve of rhodium foil. Surrounding the tube and foil is a $2\frac{3}{4}$ in. diameter cylinder of paraffin which in turn is covered by cadmium foil. Neutrons emitted from the target, with energies greater than a few electron volts, pass

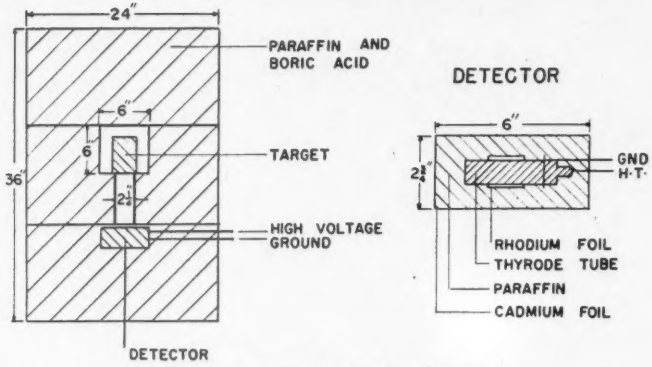

FIG. 3. Apparatus for neutron detection.

through the cadmium foil, are moderated by the paraffin cylinder, and some of them are captured by the rhodium foil. The resulting 44 sec. and 4.2 min. neutron induced activities in Rh^{104} are then counted by the thyrode counter.

The experimental procedure was to radiate the target for 132 sec., shut off the betatron, and then apply the high voltage to the thyrode $\frac{1}{2}$ sec. later. A count was taken for three minutes. The total count per roentgen, as determined by a Victoreen 'r.' chamber placed in an 8 cm. cube of Lucite, was plotted as a function of the maximum betatron energy.

RESULTS

The neutron background with no target in place was found to vary linearly with the maximum betatron energy up to 20 Mev., and then level off. In order

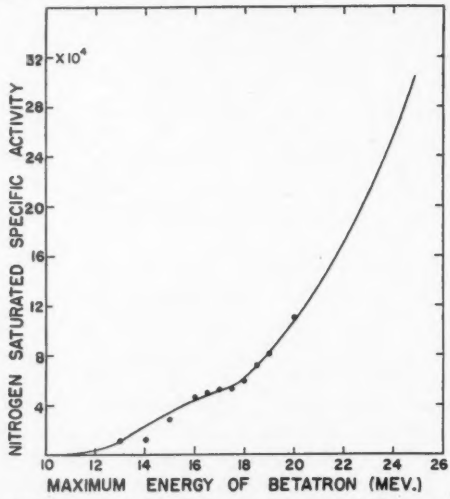

FIG. 4. The solid circles represent the relative total neutron yields from nitrogen at maximum betatron energies up to 20 Mev. These values have been normalized to the nitrogen saturated specific curve at 19 Mev.

to establish how many neutrons from the beam were scattered by the target into the detector, a block of paraffin, which approximated in size the nitrogen compound target dicyandiamide, was used as a target. Neutrons arising from photonuclear reactions in the paraffin would not be appreciable below 20 Mev. because of the high (γ, n) threshold in C^{12} (18.7 Mev.). This scattering contribution, which also includes the neutron background, was subtracted from the readings obtained with the dicyandiamide target. The final results were then normalized to the nitrogen saturated specific activity curve redrawn in Fig. 4. The points shown as solid circles are scattered about the initial portion of this activity curve, but are in close agreement above 16 Mev. The neutron yield curve cannot be determined too accurately because of poor statistics. For example at 18 Mev., the total count for three minutes was 1070. However, of this number 523 is attributed to the neutron background and 316 to neutrons scattered by the target into the detector. At least three or more determinations were made at each energy. The final result is thought to be accurate to about 10%. It is certain, however, that a hump does occur in the neutron yield curve at the same energy as it does in the saturated specific activity curve; thus the same type of cross-section curve would be obtained in each case.

ENERGY RESPONSE OF DETECTORS

The energy response characteristics of the detector are not known. It is obvious that, if the response is strongly dependent on energy, variations from a smooth neutron yield curve might be explained in terms of the level structure in N^{13}. The

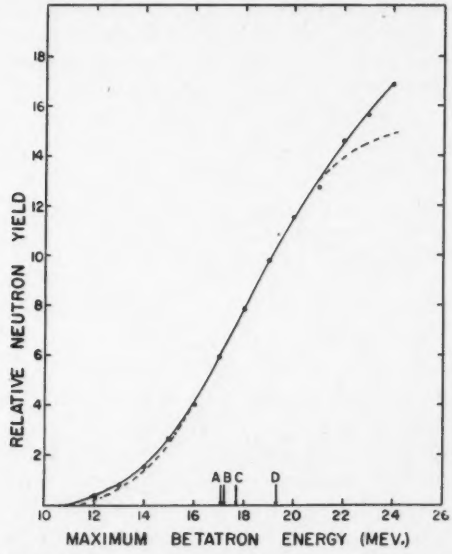

FIG. 5. The relative total neutron yield curve for copper plotted as a function of the maximum betraton energy. The $Cu^{63}(\gamma, n)Cu^{62}$ saturated specific activity curve has been normalized to the neutron yield curve at 18 Mev. *A*, *B*, *C*, and *D* represent the thresholds for the reactions $Cu^{65}(\gamma, np)Ni^{63}$, $Cu^{65}(\gamma, 2n)Cu^{63}$, $Cu^{63}(\gamma, np)Ni^{61}$, and $Cu^{63}(\gamma, 2n)Cu^{61}$ respectively.

authors think that it is extremely unlikely that the shape of the neutron yield curve would agree so closely with the shape of the saturated specific activity curve on this explanation. Further, a total neutron yield curve for copper has been obtained by this latter method (Fig. 5). With a copper target, the counting statistics were improved greatly. For example at 20 Mev., the total count for three minutes was about 40 times background.

The total neutron yield curve for copper should correspond closely to the sum of the neutron yields from the reactions $Cu^{63}(\gamma, n)Cu^{62}$ and $Cu^{65}(\gamma, n)Cu^{64}$, weighted in proportion to their isotopic abundances. If we assume that the shapes of the activation curves for these two reactions are identical, then either one may be compared to the relative total neutron yield curve. In Fig. 5, the $Cu^{63}(\gamma, n)Cu^{62}$ activity curve (2) has been normalized to the neutron yield curve at 18 Mev. The above assumption would not be valid at low energies since the thresholds for the two reactions are different. This might qualitatively explain the difference between the two curves, at low energies. Neutrons produced in $(\gamma, 2n)$ and (γ, np) reactions could prevent the neutron yield curve from falling off as rapidly as the activity curve above 21 Mev. Calculated thresholds for the $(\gamma, 2n)$ and (γ, np) reactions in copper are shown in Fig. 5. If the detector were strongly energy dependent, the activity curve and neutron yield curve should differ strongly over their whole course. However, it is seen that the agreement in shape is excellent, especially in the region between 16 and 21 Mev.

CONCLUSIONS

In view of the above results we conclude that the initial peak in the nitrogen cross-section curve is not caused by a large (γ, np) cascade reaction. This initial peak and also the first portion of the oxygen cross-section curve may be explained by a falling off of the electric quadrupole and magnetic dipole absorption. The sharp increase in the nitrogen cross-section curve at about 17 Mev. and the increase in the oxygen curve at about 20 Mev. may be attributed to the onset of electric dipole absorption.

ACKNOWLEDGMENTS

The authors appreciate the financial assistance of the National Research Council and the National Cancer Institute of Canada. One of the authors (R. J. H.) is indebted to the National Research Council for a studentship. The authors also wish to thank Dr. L. Katz for his helpful discussions.

REFERENCES

1. Johns, H. E., Horsley, R. J., Haslam, R. N. H., and Quinton, A. Phys. Rev. 84:856. 1951.
2. Johns, H. E., Katz, L., Douglas, R. A., and Haslam, R. N. H. Phys. Rev. 80:1062. 1950.
3. Katz, L. and Cameron, A. G. W. Can. J. Phys. 29:518. 1951.
4. Katz, L., McNamara, A. G., Forsyth, P. A., Haslam, R. N. H., and Johns, H. E. Can. J. Phys. 28:113. 1950.

FLUORESCENT SPECTRA OF SOME ORGANIC SOLID SOLUTIONS[1]

By F. R. Lipsett[2] and A. J. Dekker

ABSTRACT

A method to measure the spectral distribution of the luminescence of solids is described. Use is made of a spectrophotometer in combination with a photomultiplier tube. Spectra have been investigated and discussed for solid solutions of naphthacene and 1,2,5,6-dibenzanthracene in naphthalene and anthracene as functions of concentration.

I. INTRODUCTION

Ganguley (4) and Bowen (1) found that, when a small quantity of naphthacene (about one part in 10^5) is added to anthracene, the fluorescence of the anthracene is suppressed and naphthacene fluorescence of high efficiency appears. As the concentration of naphthacene is increased, the intensity of the naphthacene fluorescence increases and that of the anthracene decreases. Finally, at a concentration of 2.93×10^{-4} moles naphthacene per mole anthracene, the naphthacene fluorescence is more than 100 times as intense as the anthracene fluorescence. The same process takes place when small amounts of naphthacene are added to naphthalene, or when anthracene is added to naphthalene, and so on.

In these particular cases, the process takes place only in solid solutions, not in liquid or gelatin solutions. A necessary condition for its presence is that the fluorescence of the impurity molecules takes place at equal or longer wave lengths than the fluorescence of the matrix compound.

The process of the transfer of energy in certain solid and liquid solutions is a common occurrence. Hence, it is surprising that practically no quantitative investigations of this phenomenon, at least in the solid cases, have been carried out. Such studies are obviously needed if a correct explanation of the transfer process is to be made. The reason for this lack of research has been the lack of adequate apparatus. The change in the relative intensities of the matrix and impurity fluorescence is enormous, and cannot be studied adequately by means of photographic plates, and the photocells used in combination with filters by some authors are not adequate for studying the band structure of the fluorescence.

The introduction of the new photomultiplier tubes has obviated the previous difficulties. When used as detectors in a monochromator, these tubes are extremely sensitive to a wide range of intensities, and with suitable calibration they are well adapted to give all the information necessary for quantitative studies of the spectra involved in the transfer process. Results obtained in this manner for naphthalene and anthracene crystals with added naphthacene and 1,2,5,6-dibenzanthracene under X-ray excitation are given in the present paper.

[1] *Manuscript received December 10, 1951.*
Contribution from the Department of Physics, University of British Columbia, Vancouver, B.C.

[2] *Now at the Royal Institution, London, England.*

II. APPARATUS AND EXPERIMENTAL PROCEDURE

The crystal under examination was irradiated with X rays of 65 KVP and 15 ma. from a Profexray portable X-ray unit, in order to produce fluorescent light. The light from the crystal was passed into the entrance slit of a Beckman Model DU Quartz Spectrophotometer, which was used as a monochromator. Fluorescent light of a particular wave length was passed from the exit slit of the spectrophotometer on to the photocathode of a selected 931-A photomultiplier tube. The tube was housed in a light-tight brass box which was screwed directly on to the spectrophotometer in place of the photocells ordinarily used with this instrument. The output of the photomultiplier was amplified by a d-c. amplifier with three overlapping ranges of sensitivity, and the output from the amplifier was read on a microammeter. The reading of the microammeter, when corrected, gave the intensity of the fluorescent light of the crystal at the wave length passed by the spectrophotometer.

The arrangement has many advantages over the conventional use of a spectrograph and a microphotometer. The sensitivity of the photomultiplier tube is much greater than that of a photographic plate, and the range of intensities it will cover is much larger.

The dispersion of the spectrophotometer changes with the wave length of light passed, and the sensitivity of the photomultiplier changes with the wave length of the light falling on the photocathode. Hence, at each wave length at which a reading is taken, it is necessary to employ a calibration curve in order to compensate for these changes. This curve was obtained as follows. Light from a clear tungsten lamp was passed through the spectrophotometer, and readings of the intensity of the light were taken at intervals of 100 Å over the wave length range 3000-6000 Å. The lamp, when operated at its rated voltage, was assumed to be a black body with a temperature of 2850°K. The intensity of radiation of a black body of this temperature, J, was calculated at each wave length at which a reading was taken. The intensity J was then divided by the microammeter reading I at each wave length, and the resulting factor J/I was plotted on a graph. When the spectrum of a crystal was to be obtained, the current read from the microammeter was multiplied at each wave length by the appropriate value of J/I read from the graph. The spectrometer slit was maintained at a constant value for each spectrum.

The procedure adopted for preparing crystals was as follows. About 0.0200 gm. of impurity and 20.00 gm. of matrix compound were carefully weighed on an accurate balance.* These compounds were then placed consecutively in a test

**Naphthalene, naphthacene, and 1,2,5,6-dibenzanthracene were supplied by Eastman Kodak; the naphthalene was sublimed in air before use. The anthracene was from the Reilly Tar and Chemical Corporation. In a study of this kind it is essential to use only materials of the highest purity. For this reason, a sample of anthracene was subjected to further purification in a chromatographic column by Dr. C. Reid, Department of Chemistry, University of British Columbia, but showed no evidence of change. Some naphthalene from a well-known company showed visible fluorescence bands attributable to impurities of naphthacene, 1,2,5,6-dibenzanthracene, and a third unidentifiable impurity. It was discarded in favor of naphthalene supplied by Eastman Kodak Co. Some anthracene purchased from the Reilly Tar and Chemical Corporation subsequent to the execution of the experiment was of much lower purity than that originally purchased. The fluorescence found for naphthacene and 1,2,5,6-dibenzanthracene were in good agreement with those found by Dr. Reid and Ganguley (5).*

tube or special container and reweighed. The mixture was then heated sufficiently to melt the compounds and to allow the impurity to dissolve. The impurities go into solution very quickly. The mixture was then allowed to cool to form a standard polycrystalline solid solution, of accurately known concentration. Mixtures of naphthalene plus an impurity were heated in air by means of a bunsen burner, while the standard mixture of anthracene plus naphthacene was placed in a container which was evacuated with a fore-pump, sealed off, and heated in a furnace. The mixtures were removed from the containers by sawing the glass from around them with a diamond saw.

Individual crystals for experiments were made by combining a small amount of the standard mixture with sufficient of the matrix compound to give a crystal of the required concentration. Some of these mixes were then treated in the same manner as the standard mixtures, while others were grown into single crystals in a furnace designed for this purpose. There was no noticeable difference between the spectra produced by the polycrystalline samples and the single crystal samples.

III. RESULTS AND OBSERVATIONS

Fluorescent spectra under X-ray excitation were obtained for the following solid mixtures at different concentrations of the added compound:

I. Naphthalene + 1,2,5,6-dibenzanthracene (Fig. 1*a*)

II. Naphthalene + naphthacene (Fig. 2*a*)

III. Anthracene + naphthacene (Fig. 3*a*).

A summary of the bands observed in these cases is given in Table I. It is to be

TABLE I

SUMMARY OF OBSERVED BANDS

Matrix	"Impurity"	Matrix bands, Å	"Impurity" bands, Å	Mole concentration for optimum transfer
Naphthalene		3430		
Naphthalene	1,2,5,6-Dibenzanthracene	3410	3520, 3720, 4080 4250, 4690, 5040	1.0×10^{-4}
Naphthalene	Naphthacene	3415	4965, 5285, 5680	3.4×10^{-5}
Anthracene (3650 Å excitation)		4040, 4220, 4460, 4690		
Anthracene (X-ray excitation)		4475, 4710, 5040		
Anthracene	Naphthacene	4445, 4710	5035, 5320, 5735	2.9×10^{-4}

noted that only three bands were observed for "pure" anthracene. Other investigators, on the other hand, usually found more than three bands under ultraviolet excitation. Because of this apparent discrepancy, the fluorescent spectrum of the anthracene single crystal was obtained under X-ray as well as ultraviolet excitation. The result is shown in Fig. 4, and a comparison with the findings of

some other investigators is given in Table II. The authors are not able to offer an explanation of these facts.

TABLE II

BANDS OF SOLID ANTHRACENE OBSERVED BY DIFFERENT AUTHORS

Excitation	Wave lengths, Å		Author
X rays		4475, 4710, 5040	Present authors
U.V.	4040, 4220,	4460, 4690,	" "
U.V.	4000, 4200,	4400, 4700, 4950	Kortum, Finck (7)
U.V. and X rays	4240,	4440, 4700	Roth (10)
U.V.	4030, 4220, 4380, 4450		Ganguley (5)
U.V.	4025, 4220,	4450, 4735, 5090	Pringsheim (8)

The spectra of the crystalline mixtures of Types II and III show that the wave lengths of the naphthacene "impurity" bands are shorter in the naphthalene than in the anthracene matrix. According to measurements by Ganguley (5), the naphthacene bands obtained in an alcoholic solution occur at even shorter wave lengths than those observed presently. A similar shift was observed when the dibenzanthracene bands, as given in Table I, were compared with those obtained by Reid (9) in a solution in ether, isopentane, and alcohol at − 180°C. It may thus be concluded that the wave lengths of the "impurity" bands depend to some extent (not the same for all bands) on the matrix. The observations made here suggest that perhaps in general, for successively shorter wave lengths of the matric fluorescence, the fluorescence of the impurity moves to shorter wave lengths.

The spectra in Figs. 1*a*, 2*a*, and 3*a* show that the proportion of energy transferred to the various "impurity" bands is not equal at all concentrations. For example, in the spectra of Fig. 3*a*, the naphthacene band at 5035Å becomes almost completely obscured by the longer wave lengths bands as the concentration of the naphthacene increases. In the spectra of Fig. 2*a*, the naphthacene band at 4965Å is more intense than the one at 5285 at a concentration of 5×10^{-7} moles, while at larger concentrations, the reverse is true. A similar change is observed in the dibenzanthracene bands at 4080 and 4250Å in Fig. 1*a*.

The intensity of various "impurity" bands as a function of the concentration is shown for the three mixtures in Fig. 1*b* and 1*c* for I; in Fig. 2*b* and 2*c* for II; and in Fig. 3*b* for III.

The concentrations for maximum transfer of energy (Table I) show no obvious relationship to one another, apart from the fact that all these concentrations are very small. The transfer is most efficient in the crystals of anthracene plus naphthacene (Fig. 3). The wave length region between the impurity fluorescent bands and the matrix fluorescent bands is, in this case, the shortest of any of the three combinations investigated. For each of the combinations of matrix plus impurity studied, the two impurity bands of longest wave length form a doublet, the components of which (except in the case of crystals of naphthalene plus naphthacene at very low concentrations) maintain very nearly the same relative intensities to one another over the concentration ranges investigated.

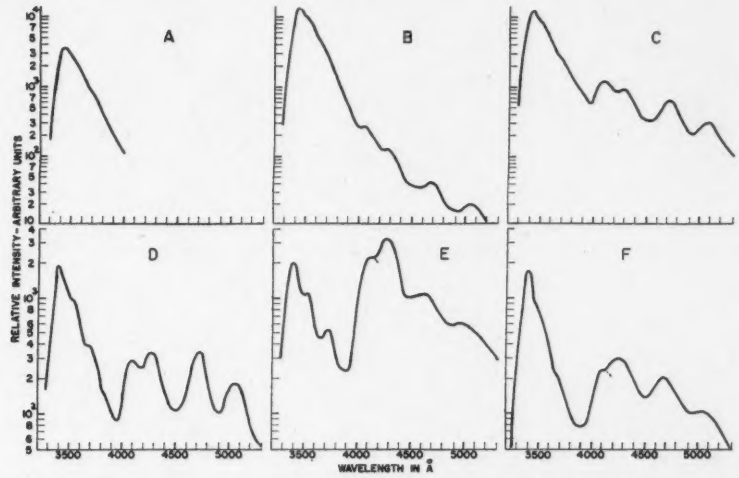

FIG. 1*a*. Spectra of crystals of naphthalene with added 1,2,5,6-dibenzanthracene. Molar concentrations: *A*, 0; *B*, 4.14×10^{-6}; *C*, 1.01×10^{-5}; *D*, 7.42×10^{-5}; *E*, 1.01×10^{-4}; *F*, 1.39×10^{-4}.

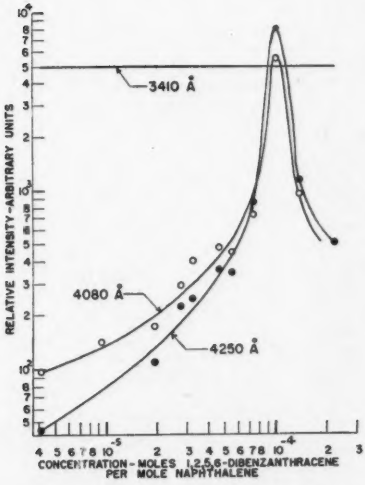

FIG. 1*b*. Intensity of the 4080 and 4250 dibenzanthracene bands relative to the 3410 naphthalene band as function of concentration.

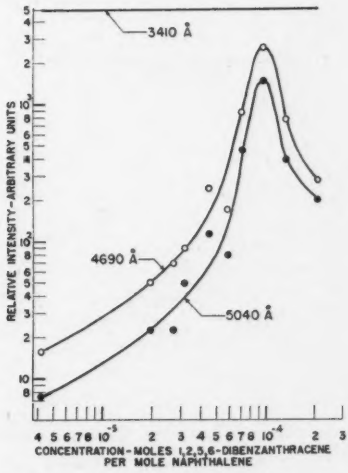

FIG. 1*c*. Intensity of the 4690 and 5040 dibenzanthracene bands relative to the 3410 naphthalene band as function of concentration.

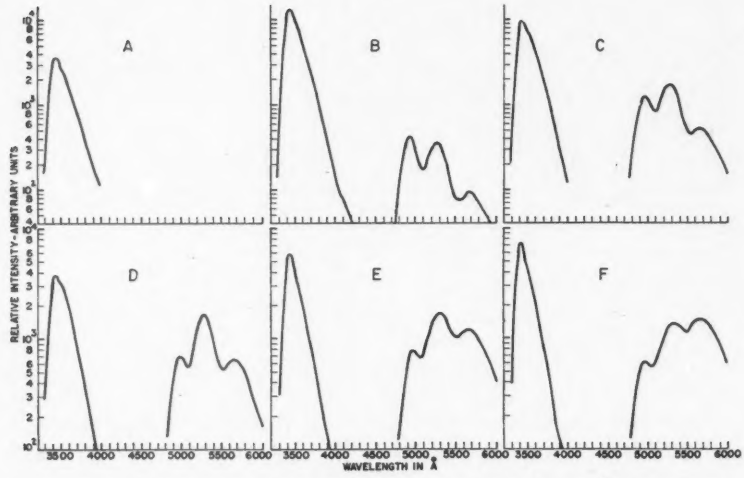

FIG. 2*a*. Spectra of crystals of naphthalene with added naphthacene. Molar concentrations: *A*, 0; *B*, 5.62×10^{-7}; *C*, 5.67×10^{-6}; *D*, 3.38×10^{-5}; *E*, 8.43×10^{-5}; *F*, 1.70×10^{-4}.

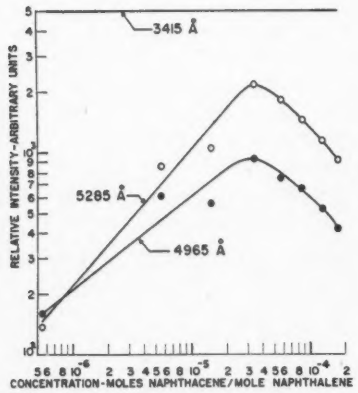

FIG. 2*b*. Intensity of the 4965 and 5285 naphthacene bands relative to the 3415 naphthalene band as function of concentration.

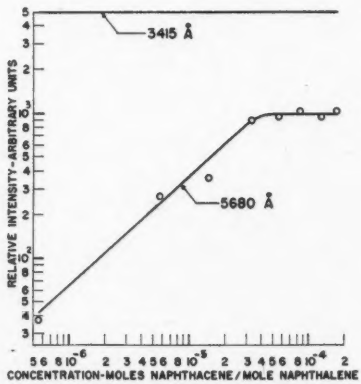

FIG. 2*c*. Intensity of the 5680 naphthacene band relative to the 3415 naphthalene band as function of concentration.

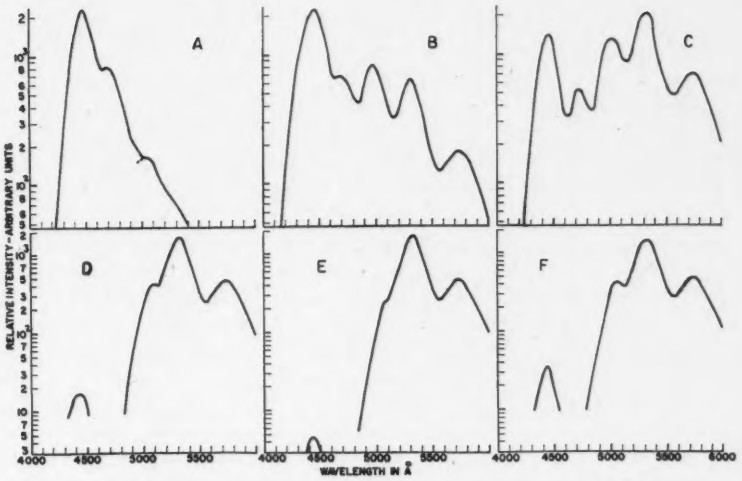

FIG. 3*a*. Spectra of crystals of anthracene with added naphthacene. Molar concentrations: *A*, 0; *B*, 8.68×10^{-7}; *C*, 2.24×10^{-5}; *D*, 1.04×10^{-4}; *E*, 2.93×10^{-4}; *F*, 9.54×10^{-4}.

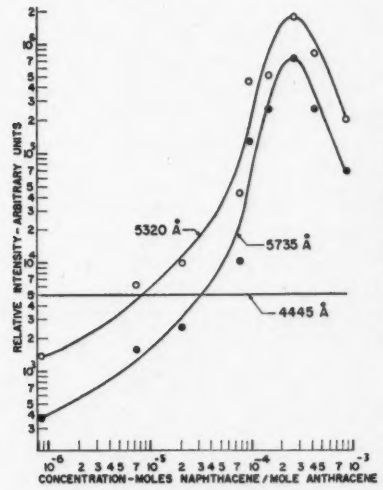

FIG. 3*b*. Intensity of the 5320 and 5735 naphthacene bands relative to the 4445 anthracene band as function of concentration.

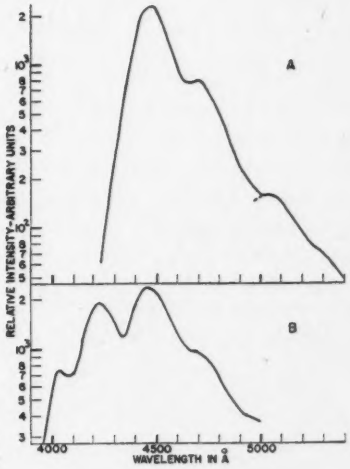

FIG. 4. Spectra of anthracene under X-ray excitation (*A*) and ultraviolet excitation (*B*).

IV. DISCUSSION

The process of energy transfer from one molecule to another has been discussed by Frenkel (3), Franck and Teller (2), and more recently by Kallmann and Furst (6). From the high efficiency of the process even for very low concentrations of the "impurity", it is very unlikely that it is caused by absorption of matrix luminescence and re-emission by the "impurity" molecules. In the case of organic molecules at least, it seems that, in the liquid as well as in the solid state, the transport of energy is due to a migration of excitons with a non-vanishing lifetime. These excitons may then be trapped by impurity molecules and eventually part of the trapped energy is emitted in the form of light. From this picture, it is clear that trapping can occur only if the wave length of the matrix luminescence is shorter than that of the impurity luminescence. For example, incorporation of naphthalene in anthracene would not lead to such a process, whereas anthracene in naphthalene could. Also, the contact between the "impurity" and matrix molecules should be strong enough for such a process to occur. It seems, therefore, that a certain amount of overlapping of the electronic orbits of "impurity" and matrix molecules is necessary. This would explain qualitatively why naphthacene in liquid solutions is much less efficient than in solid anthracene or naphthalene. Because of the required overlapping, it is then not surprising that the wave length of the luminescence of the "impurity" molecules depends to some extent on the matrix or solvent, as found experimentally and mentioned already in Section III.

Except for Fig. 2*c*, all intensity versus concentration curves show a maximum. Similar observations were made by Kallmann and Furst (6) in liquid solutions, although they used counter methods to measure the total light output. The curves of these authors show, however, much less pronounced maxima. Kallmann and Furst explain the decrease of intensity after the optimum concentration has been surpassed on the basis of self-quenching of the impurity molecules. This seems, indeed, the only possible explanation at present.

In solids, the coupling between impurity molecules by means of lattice vibrations is obviously stronger than in liquids, and this may be the reason why the maxima are more pronounced in the former case. It is still difficult, however, to understand the strong dependence on concentration in the neighborhood of the maximum. It seems, therefore, that many more quantitative experimental results will be required before less qualitative considerations on this subject can be given.

ACKNOWLEDGMENTS

The authors are much indebted to the Defence Research Board of Canada for allowing them to publish these investigations. Appreciation is also expressed to the National Research Council, Ottawa, for granting a bursary to one of us (F.R.L.) during the session 1950-1951.

REFERENCES

1. BOWEN, E. J. Nature, 159: 706. 1947.
2. FRANCK, J. and TELLER, E. J. Chem. Phys. 6: 861. 1938.
3. FRENKEL, J. Physik. Z. Sowjetunion, 9: 158. 1936.
4. GANGULEY, S. C. J. Chem. Phys. 13: 128. 1945.
5. GANGULEY, S. C. Nature, 153: 652. 1944.
6. KALLMANN, H. and FURST, M. Phys. Rev. 79: 857. 1950.
7. KORTUM, G. and FINCK, J. L. Z. physik. Chem., B, 52: 263. 1942.
8. PRINGSHEIM, P. Trans. Faraday Soc. 35: 28. 1939.
9. REID, C., Department of Chemistry, University of British Columbia, Vancouver, B.C. Private communication.
10. Roth, L. Phys. Rev. 75: 983. 1949.

SURFACE LOSSES IN ELECTROMAGNETIC CAVITY RESONATORS[1]

By I. Paghis[2]

ABSTRACT

The effective skin resistance of brass has been determined at microwave frequencies, by means of Q measurements. Refinements have allowed the Q measurements to be made with an accuracy of the order of 0.3% over a wide frequency range. The measured values are in essential agreement with theoretical prediction, provided that surface treatment is confined to slow hand polishing. This agreement holds for relaxation calculations on re-entrant type resonators, as well as for rigorously soluble resonators. An attempt has been made to correlate the surface roughness of a resonator with the effective skin resistance. The results obtained are in agreement with theoretical work. The effect of surface scratches is small when compared with the effect of a distortion in the crystal lattice at the surface of the brass, due to surface work. The perturbation of the field distribution of the normal modes by wall losses is usually assumed to be negligible. A calculation by the relaxation method shows that, for the best conductors at room temperatures, the perturbation of the normal modes may become serious at millimeter wave lengths.

INTRODUCTION

The measured resonant frequencies of electromagnetic cavity resonators check closely with theoretical predictions, but the measured resonator losses are invariably higher than predicted. This result is not caused by the anomalous skin effect in metals, since the anomaly only appears at extremely low temperatures. Various authors have suggested that the additional loss is caused by surface roughness, or by a very thin surface layer with an abnormally high resistance (13).

In this research, the relation between surface roughness and resonator losses was investigated. Losses were determined by measuring the quality factor, Q, of a cylindrically symmetric brass resonator, in the frequency range of 550-1050 mc. per sec.

Three general methods of solution of cavity resonators have been described in the literature.

(1) Division of the cavity into solvable sections (4, 5).

(2) Perturbation method, working from a known solution (3).

(3) Southwell's relaxation method (10, 14).

The relaxation method was used in the present calculations.

To interpret Q measurements in terms of surface losses in the resonator, it is convenient to use an equivalent circuit representation derived from a consideration of the normal mode fields. The previously published equivalent circuit (8) is incorrect, and a corrected derivation is presented elsewhere (11). The error does not affect calculations of power relations, but leads to wrong results when frequency parameters are being considered.

EXPERIMENTAL METHODS

A cylindrically symmetric brass resonator fitted with variable re-entrant sections was constructed. The TM_{010} mode of operation was chosen because of

[1] *Manuscript received October 16, 1950, and, as revised, December 6, 1951.*

Contribution from the Department of Physics, University of Toronto, Toronto, Ont. Based on a thesis submitted in partial fulfillment of the requirements governing the award of the degree of Doctor of Philosophy at the University of Toronto.

[2] *Holder of a Fellowship under the National Research Council of Canada, 1948-49, now at the Defence Research Electronics Laboratory, Ottawa, Canada.*

its nondegeneracy and ease of excitation, as well as for the wide frequency range obtainable by moving the re-entrant sections. The resonant frequencies of the TM_{010} mode were measured as a function of the re-entrant cylinder position, Fig. 1. The resonant frequency curves of many other oscillation modes, not shown in the figure, cross this frequency curve. Q measurements were not made near such cross-over points, since cross-coupling between modes invalidates the simple resonance theory. The resonator surfaces were prepared by scratching with various grades of emery paper along specified directions, and the loaded Q, Q_L, was determined by measuring the power output near the TM_{010} resonance.

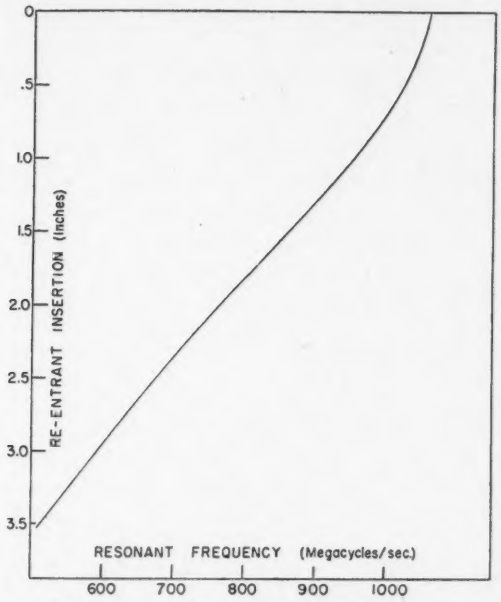

FIG. 1. Resonant frequency of the TM_{010} mode.

A schematic cross section of the resonator is shown in Fig. 2. The circular cylinder A and the circular variable re-entrant cylinders B are standard brass tube stock. The end plates C are of cast brass, while the slotted springs D are silver-plated phosphor bronze. The perimeters of the two ends of cylinder A differ by about 0.006 in., the variation being continuous in one direction. The mean difference between two perpendicular diameters in the same plane is between 0.001 and 0.002 in.

The experimental arrangement for a Q measurement is shown in Fig. 3. Oscillators Nos. 1 and 2 are identical lighthouse triodes, type 2C40, with a beat-note stability of two parts in 10^7 over an average three minute period at 1000 mc. per sec. Oscillator No. 2 was maintained at a fixed frequency, while oscillator No. 1 varied in steps of 10-20 kc. per sec. Power from oscillator No. 1 entered the resonator via an attenuating pad. The resonator output at resonance, and

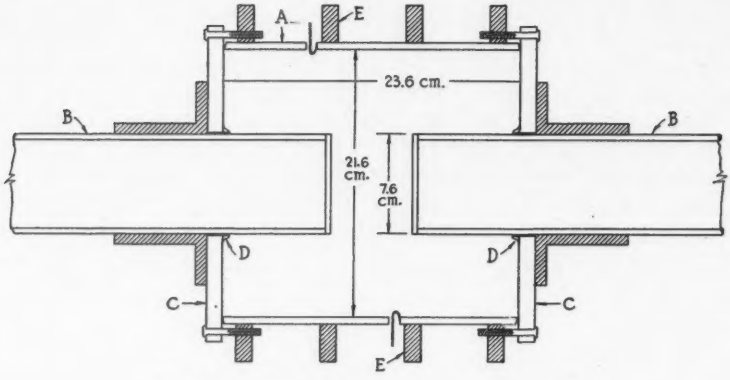

FIG. 2. Schematic cross section of cavity resonator.

down to one-third of the maximum output on each side of resonance, was rectified and continuously recorded. The beat frequency between the two oscillators was measured by comparison with a video signal generator. This beat note wanders for some time after each frequency change, and in order to avoid having to wait for the steady state, the video frequency oscillator was adjusted after each shift of oscillator No. 1 until a stationary Lissajous pattern was observed on an oscilloscope. At this moment, the spark coil was energized. The radiative output of the coil penetrated the shielding of the crystal rectifier, the rectified signal appearing as a frequency marker pip on the recorder trace.

The technique used to roughen the resonator surface is of some importance, since in surface finishing by ordinary machine methods the high speeds and point pressures produce a temperature rise sufficient to melt the surface layers of the metal, and the resultant crystal dislocations reduce the conductivity (6). Accordingly the resonator surface was worked by hand at low speeds and low pressures. First, the surface was "polished" by scratching with aluminum oxide

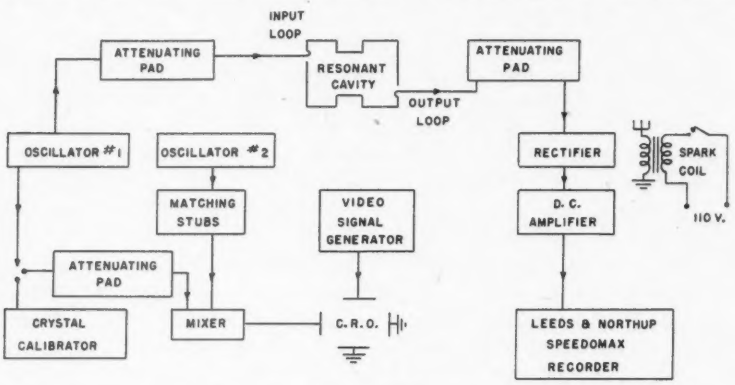

FIG. 3. Block diagram for loaded Q measurement.

of about 1000-mesh size using water lubricant. The final scratch lines were in the direction of the current paths of the TM_{010} mode. The polished cavity was then scratched in turn with 4-0, 2-0, 2, and F8(0) emery paper, using kerosene lubricant. *Scratches were first made across the current paths, and then along them,* so that the measured Q values alternately decreased and increased. In Table I the unloaded Q values, Q_0, are shown as a function of surface scratches, for a series of resonator shapes.

TABLE I

THE EFFECT OF EMERY SCRATCHES ON Q_0 VALUES

Grade of emery paper	See the footnote:	Re-entrant (in.)			
		0	1	2	3
4-0	*a*	16,260	8940	7050	6060
	b	16,100	8780	6720	5890
2-0	*a*	16,060	8805	6830	5990
	b	15,750	8550	6560	5810
2	*a*	16,010	8910	6770	5940
	b	15,450	8540	6530	5640
F8(0)	*a*	15,990	8880	6840	5880
	b	15,590	8500	6380	5680

(*a*) Scratches made along the current paths of the TM_{010} mode.
(*b*) Scratches made across the current paths of the TM_{010} mode.

Sample brass plates were roughened, as above, and the surface topography recorded on a Brush Surface Analyzer. A duplicate set of plates was copper-plated. The surfaces were then sectioned at right angles, embedded in polystyrene, polished, and photographed at a total magnification of 1500, Fig. 4. These microphotographs were taken in the Metallurgical Department of the University of Toronto, with the assistance of Dr. B. H. Thall. The mean depth of the surface scratches was much less than anticipated, and the scratches made by 2-0 emery paper were barely resolved by the optical microscope. The spacing between scratches is somewhat less than the 500 μin. tip radius of the stylus of the Brush Surface Analyzer. Nevertheless, the mean depth indicated by this instrument is in fair agreement with the profile microphotographs.

The contact springs D inside the resonator cause extraneous losses. These springs were removed, solid brass circular plates were inserted flush with the inner surface of the end plates, and Q_L was measured. On replacing springs D, the re-entrant cylinders were inserted up to the zero re-entrant position and Q_L was remeasured. The loss due to the springs alone was 1.7% of the total wall losses.

To check reproducibility, a series of Q measurements were made on the uniform cylindrical resonator with plug inserts replacing the contact springs. The end plates C were removed and replaced prior to each measurement. The mean Q_0 value of five measurements was 16,590 with a maximum deviation of 0.5% and a mean deviation of 0.3%.

CALCULATIONS

The general method of solution of cavity resonators by Southwell's relaxation method has been described by Motz (10). This method was adapted, taking into account the differing d-c. conductivities of the various resonator sections. The Q_0 of the uniform cylindrical resonator was 17,800 $\pm$ 0.5%, on the assumption of a smooth surface and normal modes unperturbed by surface losses. In addition, the Q_0 and resonant frequency ω_0 were calculated for the cavity with re-entrant cylinders inserted 1.5 in. The calculated and experimental Q_0, ω_0 values are compared in Table II. Two problems with known theoretical solutions were solved by the relaxation process (Appendix I) in order to prove that the perturbation of the normal modes by wall losses may be neglected under the experimental conditions. An estimate of the probable error of the relaxation method was also obtained.

TABLE II

COMPARISON OF CALCULATED AND EXPERIMENTAL Q_0 VALUES
(Re-entrant insertion 1.5 in., TM_{010} mode)

	Q_0	ω_0(mc./sec.)
Calculated	8690	866.0
Experimental, 4-0 emery scratches along the current	7610	860.5
Experimental, with corrections for contact spring losses and surface roughness	7810, or 90% of the calculated value	
Experimental, with correction for the frequency change caused by the contact springs		863.5 or 99.7% of the calculated value

All these calculations assume a perfectly smooth surface and correction must be made for surface roughness before the resonator losses can be properly evaluated. Morgan's work on grooved surfaces (9) is not directly applicable here, but his mathematical analysis is a useful guide to an empirical approach. Consider rectangular grooves cut in a metal of skin depth δ at right angles to the current paths, Fig. 5. Morgan finds the effective surface area by solving the field equations in the metal, on the assumption that the magnetic field is constant over the entire grooved surface. In the present calculations, no attempt was made to solve for the field equations inside the metal. Instead, the corners of the grooves were rounded off, to a radius of curvature equal to the skin depth δ, and the resultant surface trace was measured directly. From Table III it is apparent that the two methods are in good agreement for $b \geqslant 2\delta$. The effective geometric surface area, $A(\delta)$, of the experimental resonator was measured by applying the same geometric construction to the irregularly shaped grooves in Fig. 4.

In addition to the correction for surface roughness, some consideration must be given to the ellipticity (eccentricity about 0.02) of the experimental resonator. Chu (1) has studied the losses in elliptic wave guides, as a function of the eccen-

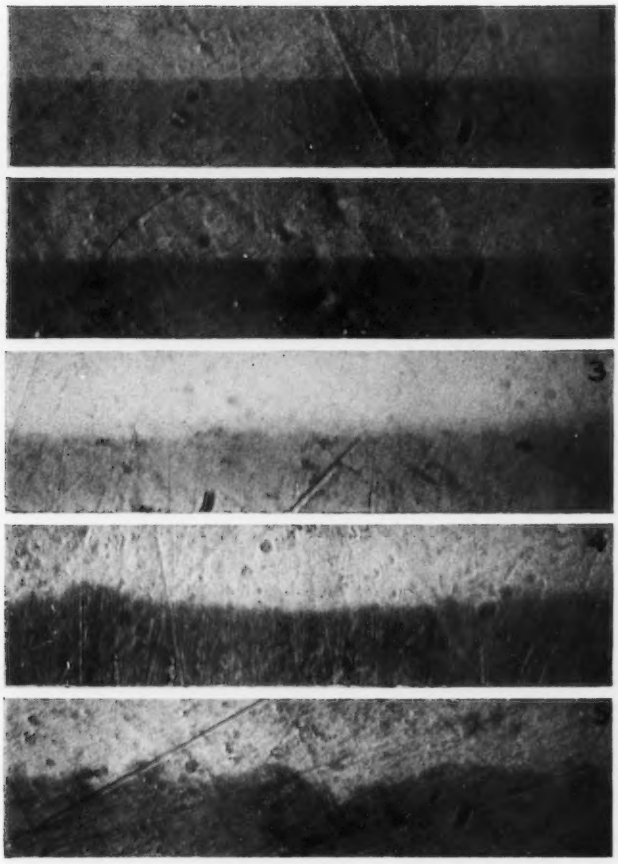

FIG. 4. Profile microphotographs, magnification 1500.

1. "Polished" brass.
2. 4-0 Emery paper scratches on brass.
3. 2-0 Emery paper scratches on brass.
4. 2 Emery paper scratches on brass.
5. F8(0) Emery paper scratches on brass.

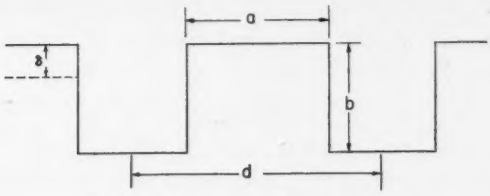

FIG. 5. Surface grooves: cross section.

tricity and operating frequency. Extrapolating boldly from Chu's data, it is found that the Q_0 of the resonator is $2 \pm 2\%$ lower than the corresponding Q_0 for a resonator with a circular cross section.

TABLE III

EFFECTIVE SURFACE AREA FOR GROOVES TRANSVERSE TO THE CURRENT FLOW

(1) Square grooves, ratio $a:b:d = 1:1:2$
(2) Rectangular grooves, ratio $a:b:d = 3:2:4$

Ratio b/δ	Mathematical analysis (Morgan)		Geometric method
	(1)	(2)	(1) and (2)
∞	2.00	2.00	2.00
3.5	1.75	1.72	1.75
2.0	1.57	1.60	1.57
1.0	1.17	1.25	1.14
0	1.00	1.00	1.00

The sum of all the resonator losses was determined from the experimental data on resonator power output near the TM_{010} resonance point. Using the corrected equivalent circuit, and noting that the input and output circuits of the resonator are symmetrical, the relation between power output and the unloaded Q, Q_0, is given by (11)

$$Q_0 = \frac{Q_L}{1 - \sqrt{P(\omega_0)/P(0)}}. \tag{1}$$

$P(0)$ is the power output of the generator into the load when the resonator is removed from the circuit and $P(\omega)$ is the power output into the load at frequency ω. We also have

$$\frac{P(\omega_0)}{P(\omega)} = 1 + \left(Q_L \frac{\Delta\omega}{\omega_0}\right)^2, \tag{2}$$

where $\omega = \omega_0 + \frac{1}{2}\Delta\omega$.

The resonance curve, Equation 2, was transformed into parabolic form and Q_L values calculated by the method of least squares, using facilities provided by the

Computation Centre, University of Toronto. The mean probable error, about 0.3%, was estimated from the dispersion of repeated measurements of the same Q_L. The Q_0 values were then obtained from Equation 1.

DISCUSSION

The measured Q_0 of the polished uniform cylindrical resonator was (93.3 ± 0.8)% of the theoretical value for a perfect cylinder. The measured value becomes (95 ± 3)% of the calculated value when the correction for ellipticity is applied. Other loss factors, such as contamination of the surface, macroscopic surface flaws, misalignment of the end plates, etc., exist but could not be evaluated in this experiment. It is instructive to compare these results with some of the available data on Q_0 measurements, Table IV. In I the resonator was constructed with extreme care, but the surface was finished by a honing process. The resultant distortion of the crystal lattice structure could account for the low ratio of experimental to theoretical Q_0 values. In II the copper surface (commercial No. 16 British s.w.g. wire) was left unpolished, and a relatively high ratio of Q_0 values was obtained. The chief reason for including the silver surfaces III in Table IV is to indicate that the effect under consideration does not depend on frequency in any obvious manner. A literature search did not reveal any precise data on the losses of brass surfaces. It seems reasonable to conclude that a brass, copper, or silver surface will have losses very close to the theoretical value, provided that the crystal lattice structure of the surface has not been seriously distorted by the surface finishing processes. In the present research, the greatest loss due to surface roughening was only 7%.

TABLE IV

MEASUREMENTS OF Q_0

Source	Mode	Resonant frequency (mc./sec.)	Ratio of Q_0 experimental to Q_0 theoretical	Resonator material
I. Essen and Gordon-Smith (2)	TM_{010}	3101	.86 ± .05	Copper
	TM_{011}	3564	.80 ± .05	Copper
II. Pippard (12)	TEM, coaxial	1200	.95	Copper
III. Montgomery (7)	TE_{011}	2800	.84	Silver plate on copper
	TE_{111}	24,000	.98	Silver
IV. Paghis	TM_{010}	1065	.95 ± .03	Brass

All of the data in Table IV refer to uniform cylindrical resonators. When re-entrant cylinders are inserted into the cavity there may be additional loss factors, owing to the misalignment and ellipticity of the re-entrant tubes. Moreover, both the relaxation calculations and the correction for contact spring losses have a larger probable error than in the case of the uniform resonator. The measured

Q_0 of the cavity with re-entrant cylinders inserted 1.5 in., Table II, is 90% of the calculated value. This result is consistent with the 95% ratio obtained for the uniform cylinder.

In Figs. 6 and 7, the measured effective geometric surface area $A(\delta)$ is plotted against the effective surface area $A(Q)$, deduced from the Q_0 values of Table I. When surface grooves are in the direction of the current paths, Morgan's calculations (9) indicate that the increase in $A(Q)$ will be only one-third as large as for grooves perpendicular to the current paths. Figs. 6 and 7 are in qualitative agreement with Morgan's result. The values of $A(Q)$ for both types of grooves average about 1% low, but this is within the experimental error of the $A(\delta)$ measurements.

ACKNOWLEDGMENTS

This problem was suggested by Dr. J. M. Anderson and Dr. R. W. McKay of the University of Toronto. The author wishes to express his appreciation of their help and encouragement during the entire research.

A grant from the Defence Research Board of Canada purchased much of the equipment used. The author is also indebted to the National Research Council for the award of Fellowships which enabled him to carry out this research.

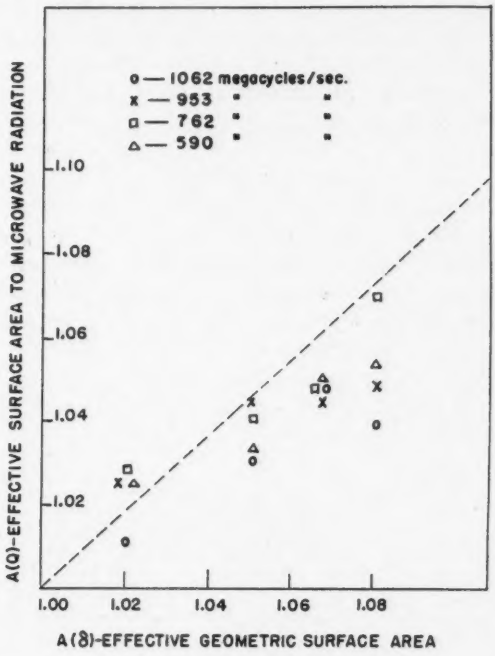

FIG. 6. Scratches across the current paths.

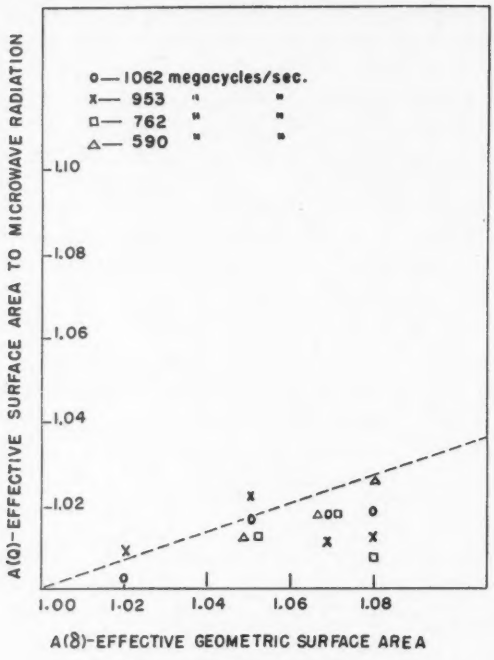

FIG. 7. Scratches along the current paths.

APPENDIX

In all analytic solutions for the electromagnetic radiation inside a cavity, perfect surface conductivity is assumed. The parameters of the cavity, other than the resonant frequency, may then be approximately determined by neglecting the perturbation of the fields caused by the surface losses. Southwell's relaxation method (10) can be applied directly to a lossy resonator, but no references have been found in the literature to calculations of this type.

Consider a uniform cylindrical cavity operating in the TM_{010} mode, with skin depth δ. Let z, r be the axial and radial directions, respectively. The boundary conditions at the walls are:

At surfaces r = constant,

$$\left|\frac{\partial \psi}{\partial r}\right| = \frac{k^2 \delta \psi}{2}.$$

At surfaces z = constant,

$$\left|\frac{\partial \psi}{\partial z}\right| = \frac{k^2 \delta \psi}{2}.$$

In the limit, $\delta \longrightarrow 0$, we obtain the usual boundary conditions for a perfect conductor.

The relaxation process was carried out for a cavity with radius 8 cm., length 16 cm., to an accuracy of 1%, Table V. The values at the bottom of the table

TABLE V

PERTURBATION OF ψ BY WALL LOSSES

z \ r	1	2	3	4	5	6	7	8
Perturbation $\Delta\psi/\delta$								
0	1.9	7.5	16.3	28.0	41.8	56.5	71.7	85.4
1	1.5	5.9	13.0	22.6	34.2	47.2	60.9	74.1
2	1.1	4.5	10.2	18.0	27.7	39.2	51.7	64.4
3	0.8	3.4	7.8	14.1	22.3	32.4	43.9	56.2
4	0.6	2.5	5.9	10.9	17.9	26.9	37.6	49.6
5	0.4	1.8	4.4	8.5	14.5	22.6	32.7	44.5
6	0.3	1.3	3.3	6.8	12.1	19.6	29.2	40.8
7	0.2	1.0	2.7	5.8	10.7	17.8	27.1	38.6
8	0.2	0.9	2.5	5.5	10.2	17.2	26.4	37.9
Unperturbed ψ values	9.6	37.2	79.0	129.2	180.8	226.0	257.6	269.3

are for the unperturbed fields in a loss free resonator, and are independent of z. They were obtained by a relaxation calculation. The maximum perturbation of ψ, at $z = 0$, $r = 8$ will be of significance in this calculation only if

$$85.4\delta \geqslant .1$$

$$\delta \geqslant 1.2 \times 10^{-3}\text{cm.}$$

For this particular cavity geometry and mode of operation the skin depth δ at room temperatures is between 0.2×10^{-3} cm. and 0.5×10^{-3} cm. for all common metals, and the field perturbations are not significant.

Now, roughly speaking, $\Delta(\psi)$ increases with increase of $|\partial\psi/\partial r|$, $|\partial\psi/\partial z|$ at the boundaries. Both of these derivatives are proportional to the three-halves power of the frequency. The above analysis, though far from rigorous, indicates that the perturbation of ψ due to wall losses will become significant above 20,000 mc. per sec.

NOTATION

$A(\delta)$ — the effective geometric surface area.
$A(Q)$ — the effective surface area deduced from Q measurements.
H_θ — circular magnetic field in a cylindrical resonator.
Q — quality factor $= \dfrac{2\pi \times \text{energy stored}}{\text{energy loss per cycle}}$.
Q_0 — unloaded Q.
Q_L — loaded Q.
k $= 2\pi/\lambda$.
δ — skin depth $= \sqrt{\dfrac{2}{\mu\sigma\omega}}$.
λ — wave length.
μ — permeability.
σ — conductivity.
ψ $= rH_\theta$.
ω — circular frequency.

REFERENCES

1. CHU, L. J. J. Applied Phys. 9:583. 1938.
2. ESSEN, L. and GORDON-SMITH, A. C. Proc. Roy. Soc. (London), A, 194: 348. 1948.
3. FESHBACH, H. and CLOGSTON, A. M. Phys. Rev. 59: 189. 1941.
4. HAHN, W. C. J. Applied Phys. 12: 62. 1941.
5. HANSEN, W. W. J. Applied Phys. 10: 38. 1939.
6. KOEHLER, J. S. Office of Naval Research, U.S.A. Tech. Rept. No. 1, N.R. 015-001. 1948.
7. MONTGOMERY, C. G. Technique of microwave measurement. M.I.T. Radiation Laboratory Series, Vol. 11. McGraw-Hill Book Co., Inc., New York. 1947. p. 325.
8. MONTGOMERY, C. G., DICKE, R. H., and PURCELL, E. M. Principles of microwave circuits. M.I.T. Radiation Laboratory Series, Vol. 8. McGraw-Hill Book Co., Inc., New York. 1947. p. 218.
9. MORGAN, S. P., Jr. J. Applied Phys. 20: 352. 1949.
10. MOTZ, H. J. Inst. Elec. Engrs. (London), Pt. III, 93: 335. 1946.
11. PAGHIS, I. The design of resonant cavities. Ph.D. thesis, University of Toronto. 1949. p. 58.
12. PIPPARD, A. B. Proc. Roy. Soc. (London), A, 191: 370. 1947.
13. REUTER, G. E. H. and SONDHEIMER, E. H. Proc. Roy. Soc. (London), A, 195: 336. 1948.
14. SOUTHWELL, R. V. Relaxation methods in engineering science. Clarendon Press, Oxford. 1940.

FORBIDDEN TRANSITIONS IN DIATOMIC MOLECULES

II. THE $^3\Sigma_u^+ \leftarrow {}^3\Sigma_g^-$ ABSORPTION BANDS OF THE OXYGEN MOLECULE[1]

By G. Herzberg

ABSTRACT

The forbidden $^3\Sigma_u^+ - {}^3\Sigma_g^-$ absorption bands of O_2 in the near ultraviolet have been obtained under high resolution with absorbing paths up to 800 m. A detailed fine structure analysis has been carried out. It confirms the identification of the band system as a $^3\Sigma_u^+ - {}^3\Sigma_g^-$ transition. Precise values of the rotational constants B_v and D_v as well as of the vibrational quanta $\Delta G_{v+\frac{1}{2}}$ in the upper state have been derived. Each of the "lines" of the Q branches observed under low dispersion is resolved into six components whose spacing yields the triplet splitting in the upper state. This splitting is more than twice as large as in the $^3\Sigma_g^-$ ground state and is of opposite sign. The splitting constants λ and γ have been determined and their variation with the vibrational quantum number observed. In addition to the Q-form branches weak O- and S-form branches have been found in agreement with the prediction of Present which is based on the assumption that spin–orbit coupling is the main cause for the occurrence of this forbidden transition. However, the relative intensities of the different branches deviate strongly from Present's prediction. The dissociation limit obtained from the convergence limit of the bands (without extrapolation) is at 41219 ± 40 cm.$^{-1}$ This value is higher by about 220 cm.$^{-1}$ than the value of the dissociation energy of O_2 derived from the Schumann–Runge bands. It is possible that the limit of the Schumann–Runge bands, which is based on a short extrapolation, and therefore the value of the dissociation energy of O_2 has to be slightly revised. The electron configurations and dissociation products of the various electronic states of O_2 are briefly discussed.

A. INTRODUCTION

In 1931 I observed (15) a very weak absorption band system in oxygen in the region 2700-2400Å. This band system showed a rather peculiar structure in that only a single Q branch was apparent in each band under the low dispersion used. Successive bands showed a rapid convergence towards 2425Å, a wave length that corresponds closely to the dissociation energy of the oxygen molecule. In view of the limitations imposed by the Wigner–Witmer correlation rules for states arising from two normal O atoms in the ^3P state and the observed band structure I concluded that these absorption bands are due to a $^3\Sigma_u^+ - {}^3\Sigma_g^-$ transition.

Later on this band system was also observed by Herman (12) and Chalonge and Vassy (6). They observed several additional bands towards longer wave lengths as well as the continuum joining on towards shorter wave lengths. In 1941 Dufay (8) suggested that this band system in emission may account for some of the more prominent features of the ultraviolet part of the spectrum of the night sky. This identification is now fairly generally accepted (see Swings (23, 24), Barbier (4), and Meinel (20)), but in view of the low dispersion of night sky spectra in the ultraviolet it cannot yet be considered as entirely conclusive.

In oxygen at high pressure Wulf (25) has observed a progression of absorption bands which almost coincide with the bands here under discussion. These bands have been investigated in more detail by Finkelnburg and Steiner (10) who found that each band consists of three diffuse peaks. The wave lengths of the

[1] *Manuscript received November 20, 1951.*
Contribution from the Division of Physics, National Research Council, Ottawa, Canada. Issued as N.R.C. No. 2725.

central peaks of these bands agree closely with the wave lengths of the zero lines of the $^3\Sigma_u^+ - {}^3\Sigma_g^-$ bands. However, Herman and Herman (13) first showed that under medium pressure with a sufficient path length both band systems occur simultaneously, thus showing conclusively that the two systems are not identical, that is, Wulf's bands are not simply the $^3\Sigma_u^+ - {}^3\Sigma_g^-$ bands modified by pressure. The quadratic dependence of the intensity of Wulf's bands on pressure and their entirely diffuse nature (Finkelnburg and Steiner (10) and below) suggest very strongly that they are due to a loosely bound $(O_2)_2$ molecule for whose presence in oxygen at high pressure and in liquid oxygen there is also other independent evidence (Lewis (19), Wulf (25), Finkelnburg (9)).

The bands here under discussion consist of sharp lines, they occur at low pressure, and their intensity varies linearly with the pressure. Therefore they are certainly due to the free O_2 molecule. The very low intensity of the bands suggests that they represent a forbidden transition. Several types of forbidden transitions have been discussed in the introduction of the first paper of this series (17). The interpretation of the O_2 bands as a $^3\Sigma_u^+ - {}^3\Sigma_g^-$ transition, which is confirmed by the present investigation, implies a forbidden transition of the first type, that is, a forbidden transition violating an approximate selection rule, in the present case the rule that Σ^+ states do not combine with Σ^- states. This rule is derived under the assumption of zero interaction between rotation and electronic motion (zero rotational distortion) and, in the case of multiplet Σ states, under the assumption of negligible spin–orbit interaction. Since these interactions are actually not entirely negligible, weak $\Sigma^+ - \Sigma^-$ transitions may occur.

Present (21) has discussed in detail the fine structure to be expected for a $^3\Sigma_u^+ - {}^3\Sigma_g^-$ transition, both on the basis of spin–orbit interaction and of rotational distortion. Each "line" of the Q branch is predicted to consist of six or seven components corresponding to the different J values for a given K. In addition, for spin–orbit interaction, branches with $\Delta K = \pm 2$ (S- and O-form branches) are expected.

In the present work the $^3\Sigma_u^+ - {}^3\Sigma_g^-$ bands have been observed under high dispersion and the fine structure has been well resolved. Most of the predicted branches have been observed at least for the strongest bands, and precise values of the rotational constants and band origins of the various bands have been determined.

A new band system, much fainter than the $^3\Sigma_u^+ - {}^3\Sigma_g^-$ system, has been found on the same plates. It consists of a progression of bands similar in spacing to the $^3\Sigma_u^+ - {}^3\Sigma_g^-$ bands and converging to the same limit. These new bands, which very probably represent a $^1\Sigma_u^- - {}^3\Sigma_g^-$ transition, will be discussed in a separate paper of this series.

B. EXPERIMENTAL

The $^3\Sigma_u^+ - {}^3\Sigma_g^-$ bands were discovered by using an absorbing path of 25 m. in oxygen at atmospheric pressure. Under these conditions (and medium dispersion) the bands appear quite faintly. It was obvious that much longer absorbing paths were required in order to obtain the bands with an intensity sufficient for a

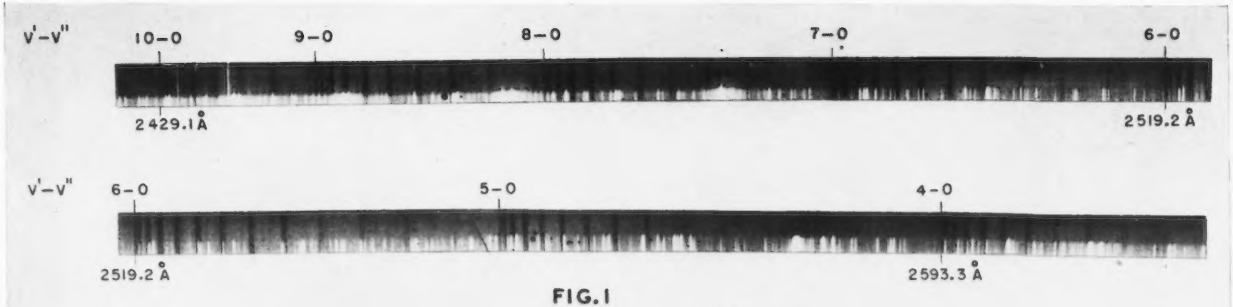

FIG. 1

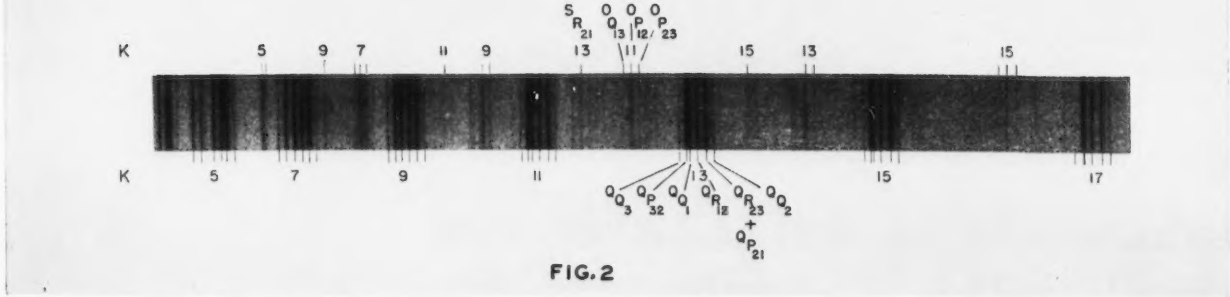

FIG. 2

FIG. 1. Absorption spectrum of O_2 in the region 2420-2600 Å with an absorbing path of 175 m. at atmospheric pressure. The Fe arc comparison lines appear at the bottom of each strip.

FIG. 2. Fine structure of part of the 9–0 band of O_2.

This section was enlarged from the same spectrogram which is shown in Fig. 1. The *Q*-form branches are marked below; the *O*- and *S*-form branches above the spectrogram. The designations are given only for one K value. The pattern repeats itself for the other K values shown.

detailed analysis. Using the 22 m. absorption tube and the multiple reflection technique described earlier (16, 17), it has been possible to obtain the $^3\Sigma_u^+ - {}^3\Sigma_g^-$ bands with path lengths up to 800 m. For this purpose aluminized rather than silvered mirrors were used since the reflectivity of silver is very low near 2500Å. The very long path lengths obtained in the infrared (see particularly Paper I (17) of this series) cannot be obtained readily in the ultraviolet since the reflectivity even of aluminum is only about 85% (compared to 95% or higher for that of silver in the red and near infrared). For the weakest bands the pressure of oxygen was increased to 2 or 3 atm. At still higher pressures the broadening of the lines becomes too large and, in addition, the intensity of the continuous background decreases on account of scattering.

The spectra were taken in the fourth order of the Yerkes 21 ft. grating. Lower orders were eliminated by means of a cylindrical prism used in the way described by Curry and Herzberg (7). Fig. 1 gives an example of the spectra obtained; Fig. 2 gives part of the band 40920 $cm.^{-1}$ with greater magnification in order to show the fine structure more clearly. The exposure times were of the order of 24 hr. The measurements were made against iron lines of third order. Judging from the agreement of independent measurements of one and the same plate the wave numbers obtained for unblended lines are accurate to ± 0.04 $cm.^{-1}$ This accuracy refers to the relative position on a given exposure. In different exposures shifts up to 0.12 $cm.^{-1}$ have been found, thus limiting the absolute accuracy of the band origins. For the very weak bands at the long wave length end the accuracy is appreciably less, viz. ± 0.1 $cm.^{-1}$ for relative measurements.

At pressures above 3 atm. in addition to the discrete bands the diffuse Wulf bands appear in conformity with the observations of Herman mentioned in the Introduction. The diffuse bands are overlapped by numerous very faint sharp absorption lines forming ill-defined bands which represent presumably the transition in free O_2 that corresponds to the diffuse bands of the $(O_2)_2$ complex.

C. ROTATIONAL ANALYSIS

(1) *Assignment of Branches*

The analysis of the fine structure of the $^3\Sigma_u^+ - {}^3\Sigma_g^-$ bands is not as readily made as that of more normal band systems, since combination differences $\Delta_2 F$ cannot be formed except for the few bands for which O and S branches have been observed. Fortunately the lower state is known with high accuracy (Babcock and L. Herzberg (3)). Using the data for this state an unambiguous analysis of the $^3\Sigma_u^+ - {}^3\Sigma_g^-$ bands has been found.

In the strongest bands each "line" of the Q branch is clearly resolved into six components as is shown in Fig. 2. Fig. 3 shows as an example the course of the six branches in the 40585 $cm.^{-1}$ band by giving the deviations from a hypothetical branch $\nu = 40585.0 - 0.78K(K+1)$. It is readily seen that the six branches form three pairs with a wave number separation of about 2 $cm.^{-1}$ for each pair. This is the separation of the component F_2 from F_1 and F_3 in the ground state of the oxygen molecule.

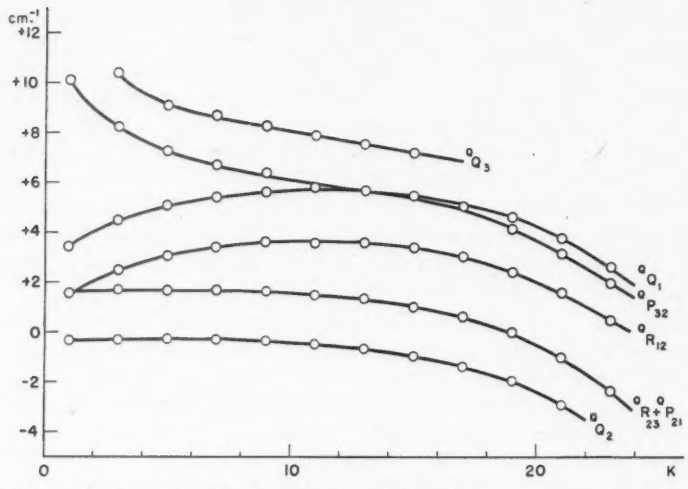

FIG. 3. Course of the six Q-form branches of the 8–0 band.
The deviations of the observed lines from the formula $\nu = 40585.0 - 0.78K(K+1)$ are plotted against K.

In Fig. 4 an energy level diagram for a $^3\Sigma_u^+ - {}^3\Sigma_g^-$ transition is shown in which all the possible branches with their designations are indicated assuming the selection rules $\Delta K = 0, \pm 1$ and $\Delta J = 0, \pm 1$. The diagram is drawn approximately to scale and in such a way that the horizontal separations of the transition lines correspond to their separations in the spectrum. The groups of S, Q, and O lines as they would appear in the spectrum are shown at the bottom, the pairs of lines with separation 2 cm.$^{-1}$ being indicated by broken-line arcs. There are seven possible Q lines for each K value, but two of these ($^QR_{23}$ and $^QP_{21}$) fall very closely together since F_1 and F_3 in the lower state are close together. Thus six components are expected in agreement with observation (see Fig. 2).

In Fig. 4 it has been assumed that the order of the component levels in the $^3\Sigma_u^+$ state is different from that in the $^3\Sigma_g^-$ ground state in that the F_2 levels are below rather than above F_1 and F_3. The alternative assignment in which the order of the levels is the same as in the ground state has also been considered. However, unlike the first assignment it leads to a variation of the triplet splitting in the upper state completely at variance with the well established formulae of Schlapp (22). In addition the S and O branches observed in some of the bands definitely rule out this alternative assignment.

Once the assignment of the various Q branches in one band had been made no difficulty was encountered in making the assignments for all the other bands, even those in which, on account of faintness of the band, only two or three of the six branches were observed. On the basis of the assignment of the Q branches and the known rotational levels of the ground state, the positions of the lines of the S- and O-form branches (see Fig. 4) can be predicted accurately. A number

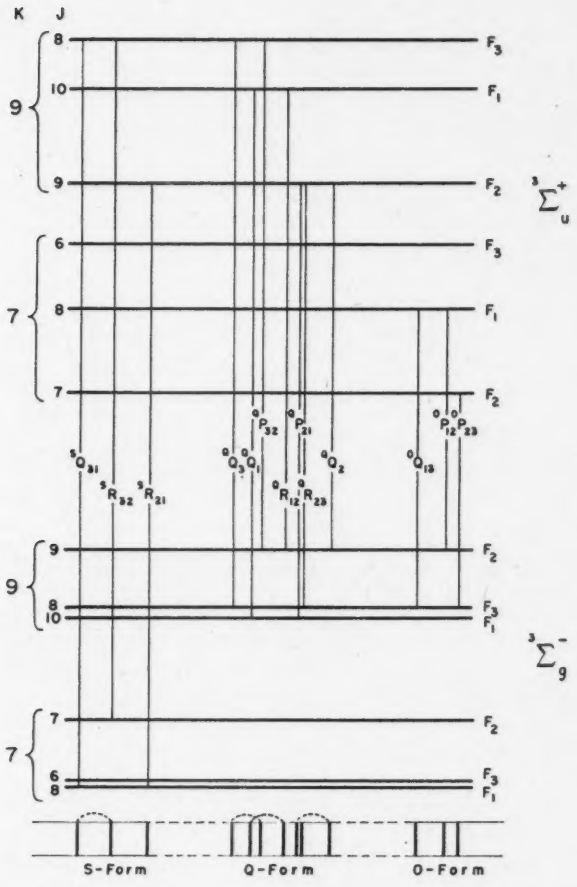

FIG. 4. Energy level diagram for a $^3\Sigma_u^+ - {}^3\Sigma_g^-$ transition.
The levels are drawn approximately to fit the observed O_2 bands. The vertical lines representing the transitions are drawn in such a way that their projections below give a representation of the spectrum. Only one line of each branch is indicated.

of these lines have thus been found. Except for the bands of highest v' these lines are always weak. Several of the *O*- and *S*-form branches are indicated in the spectrogram Fig. 2.

In Table I the wave numbers of the lines of all observed bands are given.

TABLE I

WAVE NUMBERS OF THE OBSERVED LINES

10–0 band, $\nu_0 = 41153.3$ cm.$^{-1}$ [a]

K''	$^{Q}Q_1$	$^{Q}Q_2$	$^{Q}Q_3$	$^{Q}P_{32}$	$^{Q}R_{12}$	$^{Q}R_{23} + {}^{Q}P_{21}$	$^{O}P_{12}$	$^{O}P_{23}$	$^{S}R_{32}$	$^{S}Q_{31}$
1	41155.53	41152.07	—	41167.65	41153.84*	{ 41156.09 153.84*	—	—	41170.80	41172.66
3	147.26	142.56	41158.71	156.63	145.30	144.60	41139.27	41139.90	164.34	166.17
5	131.18	125.77	140.44	138.44	*b*	127.72	119.43	118.34	150.49	152.62
7	106.92	100.77	115.13	113.19	104.86	102.78	091.85	090.23	128.47?	*
9	074.28	067.84	082.19	080.19	072.22	069.86	055.99	054.14		
11	036.18	029.16†	041.70	039.79	034.10	031.45	011.90	009.59		064.71?
13	40988.08	40981.12†?	40992.98	40991.00	40986.05	40982.92	40962.21	40959.82		
15	930.30		936.66†	934.46	928.41	924.05	902.76†			

9–0 band, $\nu_0 = 40920.45$ cm.$^{-1}$ [c]

K''	$^{Q}Q_1$	$^{Q}Q_2$	$^{Q}Q_3$	$^{Q}P_{32}$	$^{Q}R_{12}$	$^{Q}R_{23} + {}^{Q}P_{21}$	$^{O}P_{12}$	$^{O}P_{23}$	$^{S}R_{21}$	$^{O}Q_{13}$
1	40922.45*	40918.75	—	40930.30	40920.39*	{ 40922.45* 920.39*	—	—	40926.28	—
3	915.03	910.31	40922.45*	920.39*	913.09	912.33	40906.05*	40906.05*	*	40907.96†
5	900.54	895.12	906.05	903.91	898.53	897.09	887.25	886.44	*	888.91†
7	878.96	873.12	883.25	881.28	876.95	875.08	861.18	859.71	*	862.84†
9	850.45	844.21	854.03	852.05	848.38	846.22	828.10	826.12	871.36†	
11	814.94	808.55	818.03	816.14	812.93	810.54	788.10	785.88	839.76†	790.52†
13	772.52	765.93	775.24	773.36	770.44	767.92	741.06	738.59	801.60†	
15	723.08	716.29	725.63	723.68	720.97	718.33	687.18	684.46†	756.69†	688.85†
17	666.51	659.63	668.84	666.95	664.37	661.67	626.36†	623.40?		
19	602.97*	595.81	604.49†	602.97*	600.72	597.88	558.69†			
21	531.91*	524.88	533.69	531.91*	529.68	526.56				
23	453.50			453.50?	451.23					

[a] *Three otherwise unassigned lines, 41121.21, 41013.90, 41139.90 cm.$^{-1}$ may be assigned to $^{O}Q_{13}(5)$, $^{O}Q_{13}(11)$, and $^{S}R_{21}(5)$ but this assignment is doubtful since no other lines of these branches have been found.*

[b] *This line is hidden by an emission line in the continuous background.*

[c] *Two otherwise unassigned lines 40931.73 and 40847.24 may be assigned to $^{S}Q_{21}(3)$ and $^{S}Q_{21}(11)$. Other lines of the $^{S}Q_{21}$ branch are overlapped by strong lines of the main branches.*

**An asterisk indicates blended lines assigned to two or more branches.*

?*A question mark indicates a doubtful assignment.*

†*A dagger indicates extremely faint lines whose wave numbers have a much greater uncertainty than the others.*

TABLE I (*Continued*)

8–0 band, $\nu_0 = 40584.67$ cm.$^{-1}$ [d]

K''	Q_{Q_1}	Q_{Q_2}	Q_{Q_3}	$Q_{P_{32}}$	$Q_{R_{12}}$	$Q_{R_{23}} + Q_{P_{21}}$	$O_{P_{12}}$	$O_{P_{23}}$	$S_{R_{21}}$	
1	40586.89*	40583.11	—	40593.58	40584.98*	40586.89* 584.98*	—	—	40591.38	
3	580.10	575.36	40585.98	583.90	578.14	577.32	40570.70*	40570.70*	589.36	
5	566.65	561.30	570.70*	568.87	564.63	563.26	552.22	551.42	*	
7	546.70	541.00	550.00	548.03	544.73	542.97	527.24	525.90		
9	520.35	514.42	523.06	521.17	518.39	516.39	495.88	494.04		
11	487.80*	481.52	489.91	487.80*	485.60	483.47	458.03	455.99	*	
13	448.67*	442.34	450.54	448.67*	446.60	444.35	413.85	411.49		
15	403.19*	396.79	404.95	403.19*	401.15	398.78	363.37	361.07	441.72	
17	351.30*	344.85		351.30*	349.28	346.89	306.36	303.71		
19	293.16	286.58		292.65	290.92	288.53	243.18	240.46		
21	228.32	221.65		227.72	226.17	233.61				
23	156.98			156.34	154.84	152.02*				

7–0 band, $\nu_0 = 40166.80$ cm.$^{-1}$ [e]

K''	Q_{Q_1}	Q_{Q_2}	Q_{Q_3}	$Q_{P_{32}}$	$Q_{R_{12}}$	$Q_{R_{23}} + Q_{P_{21}}$	$O_{P_{12}}$	$O_{P_{23}}$	$S_{R_{32}}$	$S_{Q_{21}}$
1	40169.16*	40165.30	—	40175.33	40167.22*	40169.16* 167.22*	—	—		40182.49?
3	162.82	158.08	40168.21	166.21	160.90	160.01	40152.87*	40152.87*		179.64?
5	150.24	144.87	154.03	152.02	148.26	146.86	135.01	*		
7	131.54	125.80	134.40	132.50	129.55	127.82	110.90	*	40155.69?	
9	107.02*	100.93	109.23	107.02*	104.85	102.89	080.67	40078.94	136.71?	138.72?
11	076.31*	070.12	078.20	076.31*	074.23	072.15	044.48	042.61		
13	039.54*	033.45	041.26	039.54*	037.60	035.42	002.58	000.30		
15	39997.25	39990.80	39998.46	39996.66	39995.09	39992.80	39954.36	39952.12†	042.61*?	
17	948.77	942.26	949.70†	948.04	946.60	944.24	900.38	898.00†		
19	894.30	887.72		893.44	892.10	889.74	840.40†			
21	833.83	827.23		832.89	831.62	829.23	774.54†			
23	767.23	*b*		766.24	765.10	762.65				
25	694.72	688.19†			692.64	689.88				
27	615.98					611.58†				

[d] *Two otherwise unassigned lines, 40498.06 and 40308.02 cm^{-1}, may be assigned to $^{O}Q_{12}(9)$ and $^{O}Q_{12}(17)$ but this assignment is very doubtful since no other lines of this branch have been found. The $^{S}R_{21}$ branch may be present but many of its lines are overlapped by lines of the main branches.*

[e] *The presence of the $^{S}R_{21}$ branch cannot be established since its strongest predicted lines coincide with lines of the main branches. One unassigned line, 39996.02 cm^{-1}, may be $^{S}R_{21}(17)$.*

TABLE I (*Continued*)

6–0 band, $\nu_0 = 39681.29$ cm.$^{-1}$ *f*

K''	Q_{Q_1}	Q_{Q_2}	Q_{Q_3}	$Q_{P_{22}}$	$Q_{R_{12}}$	$Q_{R_{23}} + Q_{P_{21}}$	$^{O}P_{12}$	$^{O}P_{23}$	$^{S}R_{21}$	
1	39683.70*	39679.92	—	39689.88	39681.82*	39683.70* 681.82*	—	—		
3	677.85	672.96		680.95	675.87	674.99	*	*	39688.19*	
5	665.89	660.50	39669.58	667.48	663.89	662.49	39650.01	*	*	
7	648.20	642.50	650.87	648.91	646.19	644.45	626.70*	*	669.58*	
9	624.90*	618.89	626.70	624.90*	622.80	620.85	597.43*	*		
11	595.75*	589.73	597.43	595.75*	593.78	591.71	562.50*	*	628.96†	
13	561.22	555.01	562.51	560.69	559.17	556.98	522.05*	39519.76†	600.21	
15	521.04	514.65	522.05	520.25	518.93	516.65		*	565.41†	
17	475.11	468.64		473.91	473.01	470.72		*		
19	423.64	417.19†		422.70	421.51	419.18		*		
21	366.54			365.41	364.44	361.96				
23	303.76			302.78	301.55	299.03				
25	235.24			234.06	232.89	230.58				

5–0 band, $\nu_0 = 39138.54$ cm.$^{-1}$ *g*

K''	Q_{Q_1}	Q_{Q_2}	Q_{Q_3}	$Q_{P_{22}}$	$Q_{R_{12}}$	$Q_{R_{23}} + Q_{P_{21}}$	$^{O}P_{12}$			
1	39140.99*	39137.21	—	39146.91	39139.15*	39140.99* 139.15*	—			
3	135.50	130.79†	*	138.53	133.52	132.62	39124.84?			
5	124.13	118.67	127.61	125.57	122.13	120.72	*			
7	107.31	101.49	109.87	107.85	105.27	103.53	*			
9	085.01*	078.96	086.99	085.01*	082.99	080.97				
11	057.24*	051.18	058.97†	057.24*	055.30	053.21	*			
13	024.32	018.09	025.80†	023.84	022.35	020.05				
15	38986.01	38979.67	38987.11†	38985.26	38983.93	38981.61	939.05*?			
17	942.33	935.73	943.34†	941.34	940.21	937.87	*			
19	893.28	886.85		892.26	891.12	888.78				
21	838.85			837.72	836.73	834.30				
23	779.18	772.55†		777.98†	777.24	774.40				

f An otherwise unassigned line 39530.94 cm.$^{-1}$ may be assigned to $^{S}Q_{21}(17)$; but no other lines of this branch have been found.

g The identification of the $^{O}P_{12}$ branch is doubtful; the other O- and S-form branches are probably absent in spite of the considerable intensity of the main branches.

TABLE I (*Continued*)

4–0 band, $\nu_0 = 38546.26$ cm.$^{-1}$[9]

K''	Q_{Q_1}	Q_{Q_2}	Q_{Q_3}	$Q_{P_{32}}$	$Q_{R_{12}}$	$Q_{R_{23}} + Q_{P_{21}}$	$O_{P_{12}}$			
1	38548.83*	38544.97	—		38546.77*	{ 38548.83* 546.77*	—			
3	543.54		*	38546.77*	541.61	540.69	*			
5	532.71	527.27	38536.17	534.14	530.70	529.24	38515.63			
7	516.61	510.65†	519.09	517.07	514.53	512.72	*			
9	495.23*	489.17	497.20	495.23*	493.26	491.14	465.66			
11	468.58*	462.69	470.07†	468.58*	466.71	464.51	*			
13	437.04	430.85		436.47	434.94	432.72				
15	400.39	393.93		399.56	398.25	395.95				
17	358.51	352.13	359.63†	357.51	356.44	354.01				
19	311.62			310.56	309.40	307.05				
21	259.48	252.89†		258.23	257.31	254.81				
23	202.33				200.05	197.88				

3–0 band, $\nu_0 = 37910.23$ cm.$^{-1}$[9]

K''	Q_{Q_1}	Q_{Q_2}	Q_{Q_3}	$Q_{P_{32}}$	$Q_{R_{12}}$	$Q_{R_{23}} + Q_{P_{21}}$	$O_{P_{12}}$			
1	37912.92*	37908.85	—	37919.47†	37910.89*	{ 37912.92* 910.89*	—			
3	907.81	903.09	*	910.89*	905.89	904.95	37896.57†			
5	897.41	891.97		898.79	895.43	893.91	*			
7	881.95	876.05	37884.53	882.38	879.97	878.06				
9	861.38*		863.32†	861.38*	859.33	857.27				
11	835.68*			835.68*	833.87	831.70	*			
13	805.47	799.04		804.80	803.43	801.07	761.96†?			
15	770.18	764.02†		769.33	768.09	765.67				
17	729.80	723.46†		728.91	727.91	725.43				
19	684.72	678.01†		683.61†	682.62	680.10†				
21	634.75			632.51*†	632.51*†	630.25†				
23	578.55†?			577.57*†	577.57*†	575.00†				

TABLE I (*Concluded*)

2–0 band, $\nu_0 = 37234.84$ cm.$^{-1}$

K''	Q_{Q_1}	Q_{Q_2}	Q_{Q_3}	$Q_{P_{32}}$	$Q_{R_{12}}$	$Q_{R_{23}} + Q_{P_{21}}$
1	37237.61*	37234.01	—		37235.67*	37237.61* 235.67*
3	232.79	227.75		37285.67*	230.86	229.80
5	222.77	217.43†	37226.00	224.16	220.82	219.20
7	208.00*	201.78†	210.16†	208.00*	205.81	203.88
9	187.96*	182.06†	190.14†	187.96*	185.95	183.86
11	163.28*	157.10†	165.04†	163.28*	161.37	159.16
13	134.11	127.70†		133.55	132.02	129.70
15	100.07	093.54†		099.16	097.94	095.58
17	061.32			060.23	059.13	056.69
19	017.74			016.69†	015.61	013.13
21	36969.67†	36962.68†?			36967.47†	36964.95†
					914.84†	911.64†

1–0 band, $\nu_0 = 36523.85$ cm.$^{-1}$

K''	Q_{Q_1}	Q_{Q_2}	Q_{Q_3}	$Q_{P_{32}}$	$Q_{R_{12}}$	$Q_{R_{23}} + Q_{P_{21}}$
1	36526.41		—		36524.76*	36526.41* 524.76*
3	522.06			36524.76*	520.28	519.13
5	512.34		36515.63†?	513.87†	510.38	508.80
7	498.12*		500.68†?	498.12*	495.94	493.87
9	478.78*			478.78*	476.75	474.65
11	454.88*			454.88*	452.81	450.71
13	426.57				424.52	422.32
15	393.61				391.68	389.25
17	356.27				354.32	351.75
19	314.54†					

0–0 band, $\nu_0 = 35780.06$ cm.$^{-1}$

K''	Q_{Q_1}	Q_{Q_2}	Q_{Q_3}	$Q_{P_{32}}$	$Q_{R_{12}}$	$Q_{R_{23}} + Q_{P_{21}}$
1						
3						
5						35765.60
7	35755.65†	35749.61†			35753.17	751.25
9	736.71*	730.35†		35736.71*	734.86	732.64
11	713.76*	707.32†		713.76*	711.81	709.39
13	686.96†	679.75†			684.76†	682.13
15		647.99†			652.92†	650.09
17						

(*2*) *Determination of Rotational Constants*

Because of the low intensity of the *S*- and *O*-form branches in most bands the rotational constants of the upper state cannot be accurately determined from combination differences. Instead the strong *Q* branches were used for a determination of the differences $B_v' - B_0''$ and $D_v' - D_0''$ and from them and the very precisely known B_0'' and D_0'' values of the ground state (Babcock and L. Herzberg (3)) B_v' and D_v' were obtained.

According to Schlapp (22) the component F_2 (with $K = J$) of a $^3\Sigma$ state follows the simple formula

$$F_2(K) = B_vK(K+1) - D_vK^2(K+1)^2 \tag{1}$$

as for a singlet state. Therefore we have for the branch Q_2 of the v–0 band

$$(2) \qquad Q_2(K) = \nu_0 + (B_v' - B_0'')K(K+1) - (D_v' - D_0'')K^2(K+1)^2.$$

Plotting in the usual way, $Q_2(K)$ against $K(K+1)$, a line is obtained whose initial slope gives $B_v' - B_0''$ and whose intercept with the ordinate axis gives ν_0, the band origin. The value of $D_v' - D_0''$ is determined by the deviation from a straight line.* The branch Q_2 is weak (see Fig. 2) and has not been observed in the fainter bands. In its place the strong unresolved pair of branches, ${}^QR_{23}$ and ${}^QP_{21}$, may be used, if the mean of $F_2'' - F_3''$ and $F_2'' - F_1''$, which is precisely known from Babcock and L. Herzberg (3), is subtracted from it (see Fig. 4). Where the Q_2 branch was not too faint the average of Q_2 and $\frac{1}{2}[{}^QR_{23} + {}^QP_{21} - (F_2'' - F_3'' + F_2'' - F_1'')]$ was taken, while in the fainter bands only the latter was used. It may be noted that the use of the unresolved ${}^QR_{23}$ and ${}^QP_{21}$ branches would introduce a very slight systematic error in the unlikely event that these two branches have very different intensities. However, in the range $K = 3$ to 11, this error in the position of the equivalent Q_2 branch would amount to at most $\pm$ 0.15 cm.$^{-1}$

In Table II the rotational constants B_v and D_v of the ${}^3\Sigma_u^+$ state determined in this way are collected. Naturally the accuracy for the fainter bands of low v' is less than for the stronger bands of high v'. For the last band (10–0) a strong perturbation occurs above $K = 11$ and makes an accurate determination of the rotational constants impossible.

TABLE II

ROTATIONAL CONSTANTS OF O_2 IN THE $A^3\Sigma_u^+$ STATE

v	B_v	ΔB_v	D_v
0	0.8881		(4.4)
		− 0.0194	
1	0.8687		(4.6)
		− 0.0196	
2	0.8491_4		4.9
		-0.0218_8	
3	0.8272_6		5.3
		-0.0238_1	
4	0.8034_5		6.1
		-0.0269_6	
5	0.77649		8.3
		− 0.03175	
6	0.74474		10.3
		− 0.03832	
7	0.70642		12.8
		− 0.04828	
8	0.65814		18.1
		− 0.06459	
9	0.59355		31.1
		-0.0965_5	
10	0.4970[a]		165
	cm.$^{-1}$	cm.$^{-1}$	$\times 10^{-6}$ cm.$^{-1}$

[a]From low K values only.

*For more details of this graphical method see Herzberg (18).

In Figs. 5 and 6 the B_v and D_v values of the $^3\Sigma_u^+$ state are plotted against v. Instead of the usual linear variation B_v decreases and D_v increases in an accelerated fashion as the convergence limit is approached. It is not profitable to express B_v and D_v as power series in v since these would converge very poorly for high v. However, using only the first few B_v and D_v values, one obtains

$$B_v' = 0.8954_9 - 0.0161_0(v + \tfrac{1}{2}) - 0.0009_7(v + \tfrac{1}{2})^2 + \ldots \quad (3)$$

$$D_v' = [4.4_8 - 0.1_0(v + \tfrac{1}{2}) + 0.10(v + \tfrac{1}{2})^2 + \ldots] \times 10^{-6} \quad (4)$$

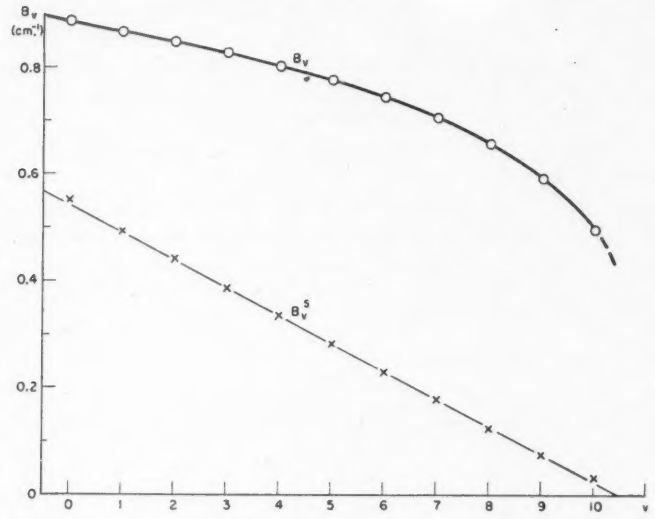

FIG. 5. B_v curve for the $^3\Sigma_u^+$ state of O_2.
In addition to B_v (circles, heavy curve) the values B_v^5 are plotted (crosses, light line).

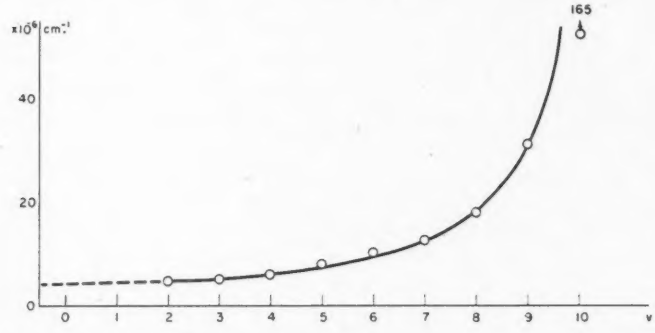

FIG. 6. D_v curve for the $^3\Sigma_u^+$ state of O_2.
The point for $v = 10$ falls beyond the limits of the diagram.

that is,

$$B_e' = 0.8954_9, \qquad \alpha_e' = 0.0161_0 \text{ cm.}^{-1}$$

$$D_e' = 4.4_8 \times 10^{-6}, \qquad \beta_e' = -0.1_0 \times 10^{-6} \text{ cm.}^{-1}$$

These values are not very accurate both on account of the uncertainty of the higher terms and of the lower accuracy of the B_v and D_v values of small v (see above). In addition the uncertainty of vibrational numbering (see below) must be kept in mind. The B_e value leads to

$$r_e' = 1.5341\text{Å}$$

using the conversion factors quoted by Herzberg (18).

Empirically one finds that $(B_v')^5$ is a very nearly linear function of v' as is shown by the crosses ($\times$) in Fig. 5. The straight line intersects the abscissa axis at $v' = 10.4$ in agreement with the nonobservation of levels above $v' = 10$. The reason for a nearly linear B_v^5 curve is not clear.

(3) Triplet Splitting

According to Schlapp the three triplet components of a $^3\Sigma$ state, neglecting centrifugal stretching terms, are given by

$$F_1(K) = B_vK(K+1) + (2K+3)B_v - \lambda - \sqrt{(2K+3)^2B_v^2 + \lambda^2 - 2\lambda B_v} + \gamma(K+1) \tag{5}$$

$$F_2(K) = B_vK(K+1) \tag{6}$$

$$F_3(K) = B_vK(K+1) - (2K-1)B_v - \lambda + \sqrt{(2K-1)^2B_v^2 + \lambda^2 - 2\lambda B_v} - \gamma K \tag{7}$$

where F_1, F_2, F_3 refer to the levels with $J = K+1$, K, and $K-1$, respectively, and where λ and γ are constants: λ is a measure of the spin–spin interaction of the unpaired electrons while γ is a measure of the interaction of the resultant electron spin with the magnetic moment produced by the rotation of the molecule. It is readily seen that on the basis of Schlapp's formulae the following sum rule should hold for the splittings

$$[F_1(K) - F_2(K)] + [F_3(K+2) - F_2(K+2)] = -(2\lambda + \gamma). \tag{8}$$

For the ground state $^3\Sigma_g^-$ of O_2 this constancy of the sum of the splittings $F_1(K) - F_2(K)$ and $F_3(K+2) - F_2(K+2)$ is very well fulfilled (within less than 0.01 cm.$^{-1}$) although with the very high accuracy possible in the microwave region a very slight deviation occurs (Burkhalter, Anderson, Smith, and Gordy (5)).

As mentioned above the triplet splitting in the upper $^3\Sigma_u^+$ state of the bands under consideration is opposite to that in the lower state, that is, the value of λ is negative. The splittings $F_1 - F_2$ and $F_3 - F_2$ are readily obtained as the differences $^QR_{12} - {}^QQ_2$ and $^QP_{32} - {}^QQ_2$ respectively. Since Q_2 is a weak branch

(see above) again in place of Q_2 the mean of ${}^QR_{23} - (F_2'' - F_3'')$ and ${}^QP_{21} - (F_2'' - F_1'')$ may be used (${}^QR_{23}$ and ${}^QP_{21}$ are not resolved, see above). Also, in place of ${}^QR_{12}$ the difference ${}^QQ_1 - (F_2'' - F_1'')$ and in place of ${}^QP_{32}$ the difference ${}^QQ_3 - (F_2'' - F_3'')$ may be used. Using in each case the best available combination or an average of such combinations the $F_1' - F_2'$ and $F_3' - F_2'$ values in Table III were obtained for the various vibrational levels. The sums $[F_1'(K) - F_2'(K)] + [F_3'(K+2) - F_2'(K+2)]$ are also given. It is seen that as required by Schlapp's formulae the sums are independent of K within the accuracy of the measurements except for the two highest vibrational levels, near the dissociation limit. According to equation 8 the sums give $-(2\lambda + \gamma)$. Mean values of $-(2\lambda + \gamma)$ for the various vibrational levels are given in the second column of Table IV. It is seen that $2\lambda + \gamma$ is independent of the vibrational quantum number for low* v, but increases appreciably with v for the last four vibrational levels. This increase indicates an increasing deviation from Hund's case (b) near the dissociation limit.

In order to determine the two splitting constants separately it is necessary to make use of the actual course of the splitting as a function of K. From the sum rule (equation 8) it follows that the two splittings $(F_3 - F_2)_{K+2}$ and $(F_1 - F_2)_K$ are symmetrical with respect to $-\lambda - \frac{1}{2}\gamma$. Rewriting equations 5 and 7 one finds

TABLE III

TRIPLET SPLITTINGS F_1–F_2 AND F_3–F_2, AND SUMS $(F_1–F_2)_K + (F_3–F_1)_{K+2}$ IN THE $A\,{}^3\Sigma_u^+$ STATE OF O_2

	$v = 0$			$v = 1$			$v = 2$			$v = 3$		
K	F_1-F_2	F_3-F_2	Sum	F_1-F_2	F_3-F_2	Sum	F_1-F_2	F_3-F_2	Sum	F_1-F_2	F_3-F_2	Sum
												9.48*
1				1.65*			1.70*			1.98*	9.48*	
						9.30*			9.60*			9.94*
3				3.08	7.65*		3.08	7.90*		2.95	7.96*	
						10.15†			10.04			9.83
5				3.56	7.07†		3.60	6.96		3.51	6.88	
						9.81*			9.72*			9.83
7	4.16			4.07	6.25*		3.93	6.12*		3.90	6.32	
			10.23*			10.20*			10.03*			10.01*
9	4.13	6.07*		4.10	6.13*		4.09	6.10*		4.06	6.11*	
			10.49*			10.26*			10.20*			10.03*
11	4.36	6.36*		4.09	6.16*		4.20	6.11*		4.16	5.97*	
									10.04			9.88
13	4.68			4.17			4.32	5.84		4.33	5.72	
									9.89			9.98
15	4.82			4.33			4.36	5.57		4.40	5.65	
									9.89			9.87
17				4.47			4.47	5.53		4.36	5.47	
									10.02†			9.86†
19							4.47	5.55†		4.49†	5.50†	
												8.74*
21							4.53†			4.33†	4.25*	
												8.89*
23							5.19†			4.56†	4.56*	

NOTE: *Values derived from blended lines or very faint lines are marked by * and † respectively.*

**Here it must be remembered that for the lowest v values the determinations are of smaller accuracy than for the other v values.*

TABLE III (*Concluded*)

	$v = 4$			$v = 5$			$v = 6$			$v = 7$			$v = 8$			$v = 9$			$v = 10$		
K	F_1-F_2	F_3-F_2	Sum	F_1-F_2	F_3-F_2	Sum	F_1-F_2	F_3-F_2	Sum	F_1-F_2	F_3-F_2	Sum	F_1-F_2	F_3-F_2	Sum	F_1-F_2	F_3-F_2	Sum	F_1-F_2	F_3-F_2	Sum
						9.73			9.99			10.03			10.49			11.55			15.59
1	1.96*			1.95*	9.73		1.94*	9.99		1.96*	10.03		1.91*	10.49		1.74*	11.55		1.60	15.59	
			10.06*			9.88			9.92			10.15			10.49			11.81*			15.66
3	2.93	8.10*		2.93	7.93		2.91	7.98		2.87	8.19		2.83	8.58		2.78	10.07*		2.73	14.06	
			9.83			9.80			9.90			10.03			10.43			11.63			15.43
5	3.47	6.90		3.44	6.87		3.41	6.99		3.39	7.16		3.37	7.60		3.44	8.85		3.45	12.70	
			9.82			9.78			9.85			10.08			10.42			11.62			15.84
7	3.85	6.35		3.77	6.34		3.72	6.44		3.73	6.69		3.73	7.05		3.85	8.18		4.11	12.39	
			9.94*			9.84			9.75*			10.12			10.50			11.69			16.47
9	4.12	6.09*		4.02	6.07		3.93	6.03*		3.95	6.39		3.95	6.77		4.18	7.84		4.38	12.36	
			10.18*			9.87†			9.96*			10.08			10.45			11.76			14.71
11	4.19	6.06*		4.10	5.85†		4.06	6.03*		4.08	6.13		4.11	6.50		4.36	7.58		4.65	10.33	
			9.93			9.87			9.75			10.00			10.40			11.78			14.75
13	4.22	5.74		4.22	5.77		4.16	5.69		4.16	5.92		4.25	6.29		4.51	7.42		5.09	10.10	
			9.82			9.84			9.75			10.01			10.53			11.89			13.49
15	4.31	5.60		4.28	5.62		4.28	5.59		4.31	5.85		4.36	6.28		4.66	7.38		6.25	8.40	
			9.80			9.81			9.49			10.10			10.78*			11.96			
17	4.40	5.49		4.40	5.53		4.30	5.21		4.38	5.79		4.40	6.42*		4.72	7.30				
			9.90			9.84			9.81			10.08			10.50			11.80*			
19	4.38	5.50		4.31	5.44		4.32	5.51		4.39	5.70		4.43	6.10		4.85	7.08*				
			9.79			9.72			9.76			10.04			10.52			12.17			
21	4.50	5.41		4.39	5.41		4.43	5.44		4.41	5.65		4.54	6.09		5.14	7.32				
						9.96†			10.17			9.99			10.85*						
23	4.21			4.71	5.57†		4.52	5.74		4.41	5.58		4.79*	6.31*							
									9.98												
25							4.37	5.46		4.49											
27										4.40†											

NOTE: *Values derived from blended lines or very faint lines are marked by * and † respectively.*

TABLE IV

SPLITTING CONSTANTS IN THE $^3\Sigma_u^+$ STATE

v	$-(2\lambda+\gamma)$	γ	λ
0	(10.3_6^*)	—	(-5.1_8^*)
1	9.9_4^*	—	-4.9_7^*
2	9.96	0.0000	− 4.98
3	9.87_8	-0.000_1	-4.93_9
4	9.84_1	-0.000_4	-4.92_1
5	9.82_2	-0.000_6	-4.91_1
6	9.85_2	-0.001_9	-4.92_5
7	10.05_1	-0.003_6	-5.02_4
8	10.47_3	-0.008_1	-5.23_2
9	11.73_5	-0.015_6	-5.86_0
10	15.63	—	(-7.81_5)

Values in parentheses are very uncertain.

$$\left.\begin{aligned}&-(\lambda+\tfrac{1}{2}\gamma)-[F_1(K)-F_2(K)]\\ &[F_3(K+2)-F_2(K+2)]+(\lambda+\tfrac{1}{2}\gamma)\end{aligned}\right\}+(2K+3)B$$
$$-\sqrt{(2K+3)^2B^2+\lambda^2-2\lambda B}=-\gamma(K+\tfrac{3}{2}). \tag{9}$$

Using for $-(\lambda+\frac{1}{2}\gamma)$ half the average sum as determined previously and averaging $-(\lambda+\frac{1}{2}\gamma)-[F_1(K)-F_2(K)]$ and $[F_3(K+2)-F_2(K+2)]+(\lambda+\frac{1}{2}\gamma)$ for each K value, the left-hand side of Equation 9 may be plotted against $K+3/2$. Here, as an approximate value for λ under the square root, the value $\lambda+\frac{1}{2}\gamma$ is used. The slope of the resulting line gives an approximate value of γ and therefore λ which may be improved by repeating the procedure by reintroducing the new λ value in the square root. The results of this procedure are collected in the third column of Table IV. For the first five vibrational levels γ is indistinguishable from 0 but it decreases rapidly for the higher vibrational levels. For $v=10$ the plot of the left-hand side of Equation 9 does not lead to a straight line and γ cannot be determined. This is apparently related to the fact that in this case a strong perturbation occurs for $K>7$ and that for higher K the sums $(F_1-F_2)_K+(F_3-F_2)_{K+2}$ are no longer even approximately constant.

As an illustration Fig. 7*a* shows the course of the three triplet components of the $v'=8$ level. The observed splittings are represented by circles, the calculated values using the λ and γ values of Table IV by the full-line curves, and the calculated values obtained by assuming $\gamma=0$ by the broken-line curves. It is seen that the effect of γ is small, but definitely present. For comparison, in Fig. 7*b* the corresponding curves for the ground state of O_2 ($v=0$) are shown as obtained from the data of Babcock and L. Herzberg (3).

As a check on the analysis the splittings $F_2''-F_1''$ and $F_2''-F_3''$ in the lower state have been determined from the combinations $^QQ_1-{}^RR_{12}$ and $^QQ_3-{}^QP_{32}$ respectively. Obviously the accuracy of these determinations is appreciably less than that of Babcock and L. Herzberg (3), but taking the average from all bands quite a fair agreement is obtained. This is shown in Table V in which the

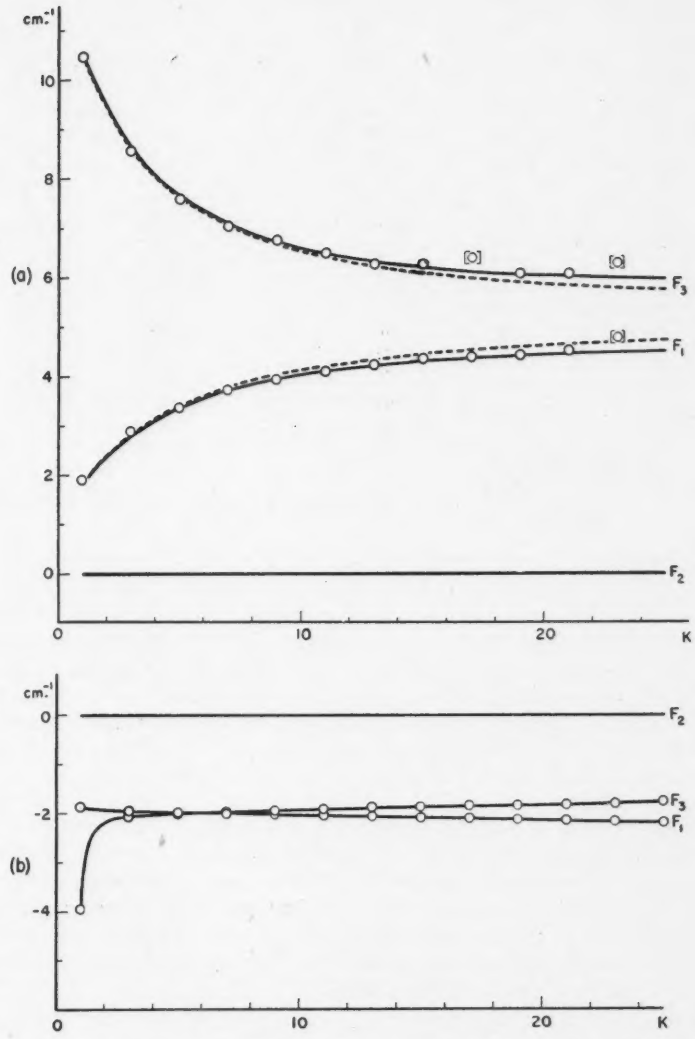

FIG. 7. Triplet splitting (*a*) in the $A^3\Sigma_u^+$ state and (*b*) in the $X^3\Sigma_g^-$ state of the O_2 molecule as a function of K.

In (*a*) the full-line curves correspond to Schlapp's Formula including γ while the broken-line curves correspond to the same formula, but neglecting γ.

splittings obtained from the $^3\Sigma_u^+ - {}^3\Sigma_g^-$ bands are compared with those obtained from the $^1\Sigma_g^+ - {}^3\Sigma_g^-$ bands and with the still more accurate ones obtained from

TABLE V

TRIPLET SPLITTING IN THE GROUND STATE ($X^3\Sigma_g^-$, $v = 0$) of O_2

	From the ultraviolet bands[1]		From the red ("atmospheric") bands[2]		From the microwave spectrum[3]	
K	F_2-F_1	F_2-F_3	F_2-F_1	F_2-F_3	F_2-F_1	F_2-F_3
1	1.93*	4.02	1.873_2	—	1.876905	3.961141
3	1.94_7	2.05_3	1.952_0	2.084_8	1.949663	2.084428
5	1.99_4	2.05_3	1.987_2	2.012_3	1.9885	2.011715
7	2.01_8	1.96_9	2.014_8	1.976_4	2.0160	1.973586
9	2.03_0	1.95_7	2.041_9	1.947_8	2.0389	1.945587
11	2.04_5	1.90	2.064_3	1.921_0	2.061546	1.921836
13	2.05_1	1.89	2.081_8	1.901_3	2.081944	1.900377
15	2.08_9	1.85	2.104_2	1.880_7	2.1006	1.880165
17	2.09_7	1.89	2.124_4	1.859_5	2.120525	1.860859
19	2.16_9		2.128_0	1.844_2	2.139185	1.842067
21	2.16_3	1.78	2.165_6	1.823_9	2.157575	1.823779
23	2.16_2		2.180_3	1.816_5	2.1756	1.805682
25	2.21_5		—	1.784_7	2.1940	1.78774

[1]*From the data of this paper.*
[2]*From Babcock and L. Herzberg (3).*
[3]*From Burkhalter, Anderson, Smith, and Gordy (5) and Anderson, Johnson, and Gordy (1) assuming* $c = 2.99776 \times 10^{10}$ *cm./sec.*

the microwave spectrum. The splitting $F_2'' - F_3''$ for $K = 1$, which on the basis of Schlapp's formulae is expected to be about twice the splitting for $K \neq 1$, cannot be obtained from the atmospheric oxygen bands ($^1\Sigma_g^+ - {}^3\Sigma_g^-$) and has only recently been observed as a microwave line at λ 2.50 mm. (Anderson, Johnson, and Gordy (1)). This splitting can in principle also be obtained from the $^3\Sigma_u^+ - {}^3\Sigma_g^-$ bands, but in each of the intense bands the appropriate lines which occur near the crowded band origin are blends with other lines and the determination of $F_2''(1) - F_3''(1)$ has very little weight.

(4) Intensities

Present (21) has given intensity factors for the various branches of a $^3\Sigma_u^+ - {}^3\Sigma_g^-$ transition both on the assumption of spin–orbit interaction and on the assumption of rotational distortion as the cause for the occurrence of this forbidden transition. In Table VI the theoretical intensities in the two cases are given for $K = 3$ and $K = 13$ taking account of the Boltzmann factor (with $kT = 210$ cm.$^{-1}$). The last two columns give the estimated intensities obtained from the observed spectra for the 9–0 band.

On the basis of rotational distortion the intensity factors of the ^QQ branches should vary as K^3 and therefore the intensity would reach a maximum only at $K = 15$. In addition the ^QQ branches should be far more intense than all the other branches (for $K = 13$ e.g. $^QQ_1$ should be 195 times as intense as $^QP_{32}$). Actually the ^QQ branches are of an intensity quite comparable to that of the ^QP and ^QR branches and the maximum of intensity in all branches occurs at about

TABLE VI

THEORETICAL AND OBSERVED RELATIVE INTENSITIES OF THE VARIOUS BRANCHES OF THE $^3\Sigma_u^+ - {}^3\Sigma_g^-$ BANDS FOR $K = 3$ AND $K = 13$

Branch	Theoretical				Observed	
	Spin–orbit interaction		Rotational distortion		9–0 band	
	$K = 3$	$K = 13$	$K = 3$	$K = 13$	$K = 3$	$K = 13$
$^QQ_1$	4.15	4.22	9.46	153	4	5
$^QQ_2$	0	0	6.55	142	1	1.5
$^QQ_3$	2.24	3.64	4.98	132	(2*)	1
$^QP_{32}$	1.12	1.06	0.622	0.786	(2*)	4
$^QR_{12}$	0.622	0.915	0.630	0.786	3	4
$^QP_{21}$	0.622	0.915	0.630	0.786	5	6
$^QR_{23}$	1.12	1.062	0.622	0.786		
$^OP_{12}$	0.747	0.980	0	0	2*	2
$^OP_{23}$	0.280	0.834	0	0	(1*)	0.5
$^OQ_{13}$	0.093	0.0058	0	0	0.2	0.3
$^SQ_{31}$	0.052	0.0050	0	0	0.5*	*
$^SR_{21}$	1.24	1.11	0	0	*	0.5
$^SR_{32}$	0.778	0.980	0	0	*	—

**Values from blended lines are marked by an asterisk.*

$K = 9$, close to the value expected for spin–orbit interaction ($K = 7$). This and the presence of some of the O- and S-form branches would appear to rule out rotational distortion as the main cause of the violation of the selection rules.

On the other hand the agreement of the observed intensities with those predicted on the basis of spin–orbit interaction is far from satisfactory. While the intensity ratio of the branches $^QP_{32}$, $^QR_{12}$, $^QP_{21}$, $^QR_{23}$ is approximately as predicted, the branches $^QQ_1$ and $^QQ_3$ which should be about four times stronger are respectively only slightly stronger and very much weaker than the ^QP and ^QR branches. The $^QQ_2$ branch which should be absent according to spin–orbit coupling is definitely present, even though with small intensity (about the same as $^QQ_3$). In addition, the ^OP and ^SR branches, which should be about as intense as the ^QP and ^QR branches, are observed to be much weaker with the exception of the $^OP_{12}$ branch which at least in the 9–0 and 10–0 bands becomes comparable to ^QP or ^QR. For lower v' values the intensity of the $^OP_{12}$ branch is much less than that of ^QP or ^QR. The intensity of the other ^OP and ^SR branches is low for all v' values and they have not been observed for the weaker bands ($v' < 6$). The two branches $^OQ_{13}$ and $^SQ_{31}$, which on the basis of Present's formulae should be extremely weak except for the lowest K values, have been observed for some of the bands of high v' with an intensity comparable to $^OP_{23}$ and $^SR_{21}$.

The reason for all these discrepancies must apparently be sought in deviations of the coupling from that assumed by Present in his calculations. It may be expected that for high v' values near the dissociation limit Hund's case (c) is approached and that therefore different intensity formulae hold. The increase of the splitting constant λ for the last vibrational levels is indicative of such a change of coupling conditions.

The $^3\Sigma_u^+$ state in case (*c*) goes over into a 1_u and a 0_u^- state, the latter corresponding to the F_1 component. It is probably significant that $^QP_{12}$, the strongest of the *O*- and *S*-form branches, is the only one involving the F_1 component.

A more detailed explanation of these intensity anomalies will only be possible when a theoretical treatment of intensities for intermediate coupling cases has been given.

D. VIBRATIONAL ANALYSIS, DISSOCIATION

When the present band system was first discovered the longest wave length band was observed to be at 2637Å. For lack of other evidence this band was designated as 0–0 band. Herman (12) has already pointed out that three additional absorption bands occur at longer wave lengths. With the much longer paths used here three additional bands have been definitely identified and measured (see Table I). Again for lack of other evidence the first observed band, at 2794Å, has been designated as 0–0 band. It must be realized however that still fainter bands at longer wave lengths may have escaped observation and that therefore the vibrational numbering may have to be raised again.* On the other hand such an additional increase would be excluded if the identification of this band system in the spectrum of the night sky (8, 23) is definitely confirmed and if no bands from lower vibrational levels are found in emission.

In Table VII the band origins ν_0 of the various bands are listed together with the first and second differences, $\Delta G_{v+\frac{1}{2}}$ and $\Delta^2 G_{v+1}$. The accelerated decrease of $\Delta^2 G_{v+1}$ shows that a representation of $G'(v)$ by the usual power series in v would only be possible by including a large number of terms. The first four levels may be represented by

$$T_0'(v') = 35780.1_2 + 758.8_9 v' - 14.63_5 v'^2 - 0.55_0 v'^3 + \ldots$$

or

$$G'(v') = 773.1_1(v' + \tfrac{1}{2}) - 13.81(v' + \tfrac{1}{2})^2 - 0.55_0(v' + \tfrac{1}{2})^3 + \ldots .$$

It must be realized that the coefficients in these equations, i.e., ω_e, $\omega_e x_e$, $\omega_e y_e$ would have to be slightly modified if higher powers were included and would have to be appreciably changed if the vibrational numbering had to be revised (see above).

Similar to the case of B_v a better representation of the $\Delta G_{v+\frac{1}{2}}$ values can be obtained by expressing $(\Delta G_{v+\frac{1}{2}})^n$ as a function of v. In Fig. 8, $\Delta G_{v+\frac{1}{2}}$ as well as $(\Delta G_{v+\frac{1}{2}})^{2.5}$ are plotted against v. It is seen that $\Delta G^{2.5}$ varies very nearly linearly with v except for the last two v values. A more nearly linear variation for the last few v values can be obtained by plotting ΔG^2 rather than $\Delta G^{2.5}$. There may be some significance in the fact that the power to which ΔG has to be raised to give a linear plot (Fig. 8) is just half of the power to which B_v has to be raised (Fig. 5).

The variation of ΔG and $\Delta G^{2.5}$ with v shown in Fig. 8 makes it extremely probable that the level $v = 10$ is the last one. Indeed, even with the longest

*One can however not conclude (as did Herman) from the observation of further diffuse O_4 bands at longer wave lengths that there will be corresponding bands of the $^3\Sigma_u^+ - {}^3\Sigma_g^-$ system since the O_4 bands correspond to a different transition in O_2.

TABLE VII

BAND ORIGINS OF THE $^3\Sigma_u^+ - {}^3\Sigma_g^-$ BANDS AND VIBRATIONAL QUANTA IN THE UPPER STATE

v'	ν_0	$\Delta G_{v+\frac{1}{2}}$	$\Delta^2 G_{v+1}$
0	35780.0_6		
		743.7_9	
1	36523.8_5		$- 32.8_0$
		710.9_9	
2	37234.84		$- 35.6_0$
		675.39	
3	37910.23		$- 39.36$
		636.03	
4	38546.26		$- 43.75$
		592.28	
5	39138.54		$- 49.53$
		542.75	
6	39681.29		$- 57.24$
		485.51	
7	40166.80		$- 67.64$
		417.87	
8	40584.67		$- 82.09$
		335.78	
9	40920.45		$- 102.2_9$
		233.4_9	
10	41153.9_4		

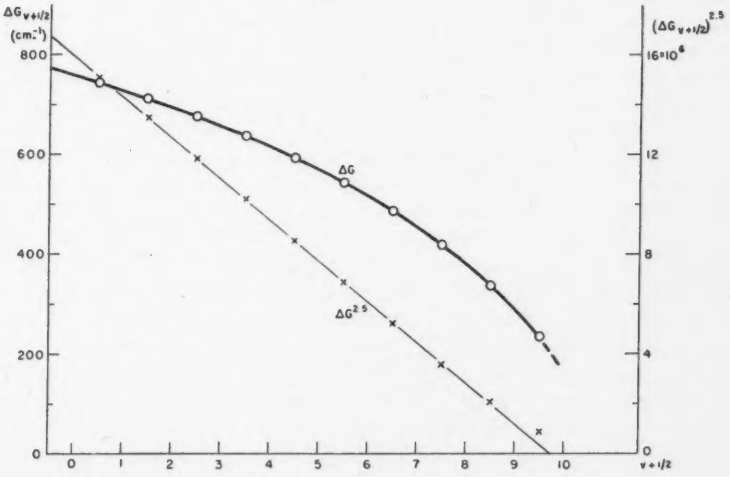

FIG. 8. $\Delta G_{v+\frac{1}{2}}$ curve for the $^3\Sigma_u^+$ state of O_2.
In addition to $\Delta G_{v+\frac{1}{2}}$ (circles, heavy curve) the values of $(\Delta G_{v+\frac{1}{2}})^{2.5}$ are plotted (crosses, light line, ordinate scale at right).

possible path lengths no further bands that might be ascribed to higher v values have been found.

As is expected from the Frank–Condon principle and as is confirmed by the observations of Herman (12) and Chalonge and Vassy (6) the maximum of intensity of the $^3\Sigma_u^+ - {}^3\Sigma_g^-$ transition lies in the continuum joining on to the bands. On the other hand the 10–0 band appears distinctly less intense than the 9–0 band (see Fig. 1). This anomaly is probably only apparent and due to the fact that the continuous spectrum overlaps slightly the discrete spectrum because rotating molecules with higher K'' values will give continuous absorption at longer wave lengths than correspond to the limit of the continuum for $K'' = 0$. Because of this continuous absorption it was found to be impossible to record the spectrum in the region of the 10–0 band for the longest path lengths used in this work.

The 10–0 band has been observed to $K = 15$. At the position where the lines with $K = 17$ would be expected appears a somewhat indistinct very diffuse feature. It seems very likely that this corresponds to the onset of predissociation by rotation. The predissociation limit (i.e. approximately the energy of the $K' = 16, v' = 10$ level which is 41284 cm.$^{-1}$ above the $K'' = 0, v'' = 0$ level) represents an upper limit to the corresponding dissociation limit. A lower limit is the energy of the $K' = 0, v' = 10$ level (41153 cm.$^{-1}$). It is clear that the dissociation limit must be appreciably above the lower limit since otherwise the centrifugal terms could not raise the effective potential curves sufficiently to cause the rotational levels to be stable up to $K = 15$. The average between the upper and lower limit, 41219 cm.$^{-1}$, should be a close approximation to the true dissociation limit, probably within $\pm$ 40 cm.$^{-1}$

The dissociation energy of the O_2 molecule is usually determined from the convergence limit in the Schumann–Runge bands which lies at 56877 cm.$^{-1}$ (Gaydon (11)) or 56859 cm.$^{-1}$ (Herzberg (18)) depending on the extrapolation made for the last three vibrational levels. Since the upper state of the Schumann–Runge bands must dissociate into one normal ($^3P_2$) and one excited ($^1D_2$) oxygen atom (Herzberg (14)) one obtains 41009 or 40991 cm.$^{-1}$ for the energy required to dissociate O_2 into two normal ($^3P_2$) atoms. This value is appreciably smaller than the dissociation limit derived above for the $^3\Sigma_u^+$ state; it is definitely smaller than even the lower limit of this dissociation limit. The simplest explanation of this difference is that the $^3\Sigma_u^+$ state dissociates into $^3P_2 + {}^3P_0$ (or $^3P_2 + {}^3P_1$) which is higher by 226.5 cm.$^{-1}$ (or 158.5 cm.$^{-1}$) than the limit $^3P_2 + {}^3P_2$. This would be analogous to the well-known fact that the upper states of the visible Cl_2, Br_2, I_2 bands dissociate into $^2P_{1\frac{1}{2}} + {}^2P_{\frac{1}{2}}$ rather than $^2P_{1\frac{1}{2}} + {}^2P_{1\frac{1}{2}}$. However, unlike the case of the halogen molecules, in the present case such a correlation is not required by the Wigner–Witmer correlation rules. For large internuclear distances all electronic states are close to Hund's case (c). In this case the four known electronic states of O_2, $^3\Sigma_g^-$, $^1\Delta_g$, $^1\Sigma_g^+$, $^3\Sigma_u^+$, yield 1_g, 0_g^+; 2_g; 0_g^+; and 1_u, 0_u^- states respectively. Two O atoms in the $^3P_2$ state give in Hund's case (c) according to the correlation rules 0_g^+, 0_g^+, 0_g^+, 0_u^-, 0_u^-, 1_g, 1_g, 1_u, 1_u, 2_g, 2_g, 2_u, 3_g, 3_u, 4_g. Thus all four electronic states mentioned can in principle result from $^3P_2 + {}^3P_2$. This holds even if one includes the upper states of the two other band systems that

TABLE VIII

DESLANDRES TABLE OF THE $^3\Sigma_u^+ - {}^3\Sigma_g^-$ SYSTEM OF O_2*

v' \ v''	0	1	2	3	4	5	6	7	8	9	10	11	12	13	14	15
0	35780.1	34223.7	32691.0	31181.8	29695.7	28232.7	26792.6	25375.1	23980.4	22608.3	21258.7	19931.7	18627.4	17345.9	16087.2	14851.5
1	36523.9	34967.5	33434.8	31925.6	30439.5	28976.5	27536.4	26118.9	24724.2	23352.1	22002.5	20675.5	19371.2	18089.7	16831.0	15595.3
2	37234.8	35678.4	34145.7	32636.5	31150.4	29687.4	28247.3	26829.9	25435.1	24063.0	22713.4	21386.5	20082.2	18800.6	17541.9	16306.2
3	37910.2	36353.8	34821.1	33311.9	31825.8	30362.8	28922.7	27505.3	26110.5	24738.4	23388.8	22061.9	20757.6	19476.0	18217.3	16981.6
4	38546.3	36989.9	35457.2	33948.0	32461.9	30998.9	29558.8	28141.4	26746.6	25374.5	24024.9	22698.0	21393.7	20112.1	18853.4	17617.7
5	39138.5	37582.1	36049.4	34540.2	33054.1	31591.1	30151.0	28733.6	27338.8	25966.7	24617.1	23290.2	21985.9	20704.3	19445.6	18209.9
6	39681.3	38124.9	36592.2	35083.0	33596.9	32133.9	30693.8	29276.4	27881.6	26509.5	25159.9	23833.0	22528.7	21247.1	19988.4	18752.7
7	40166.8	38610.4	37077.7	35568.5	34082.4	32619.4	31179.3	29761.9	28367.1	26995.0	25645.4	24318.5	23014.2	21732.6	20473.9	19238.2
8	40584.7	39028.3	37495.6	35986.4	34500.3	33037.3	31597.2	30179.8	28785.0	27412.9	26063.3	24736.4	23432.1	22150.5	20891.8	19656.1
9	40920.5	39364.1	37831.4	36322.2	34836.1	33373.1	31933.0	30515.6	29120.8	27748.7	26399.1	25072.2	23767.9	22486.3	21227.6	19991.9
10	41153.9	39597.5	38064.8	36555.6	35069.5	33606.5	32166.4	30749.0	29354.2	27982.1	26632.5	25305.6	24001.3	22719.7	21461.0	20225.3

*All but the values in the first column are computed values (see text).

occur in the region of the $^3\Sigma_u^+ - {}^3\Sigma_g^-$ bands and have not yet been analyzed. These two states are in all probability $^3\Delta_u$ and $^1\Sigma_u^-$, that is, in case (*c*) $3_u, 2_u, 1_u$, and 0_u^-.

In order to retain the correlation $^3\Sigma_u^+ \rightarrow {}^3P_2 + {}^3P_0$ one is therefore forced to conclude that a crossing over takes place of this state with another state having the same Ω values and dissociating into $^3P_2 + {}^3P_2$, in violation of the non-crossing rule. The only alternative appears to be the assumption that the small extrapolation for the upper state of the Schumann-Runge bands is erroneous. If the convergence limit of the Schumann-Runge bands were really at 57087 cm.$^{-1}$ instead of at 56859 cm.$^{-1}$ no difficulty would arise. This would imply a change of the dissociation energy of oxygen from 5.080 to 5.109 ev. In order to reach a decision between these two alternatives it will be necessary to ascertain which is really the last vibrational level of the upper $^3\Sigma_u^-$ state of the Schumann-Runge bands as was done here for the $^3\Sigma_u^+$ state. Such an investigation is being prepared in this laboratory.

As was mentioned in the Introduction, the $^3\Sigma_u^+ - {}^3\Sigma_g^-$ bands have been identified in the emission spectrum of the night sky. For the purpose of checking this identification and of identifying additional bands it may be useful to present a Deslandres Table of the band system based on the revised wave numbers of the absorption bands. This is done in Table VIII. The wave numbers given, except those with $v'' = 0$, are calculated values and refer to band origins. The band heads will agree closely with these band origins. For the lower state the vibrational formula of Curry and Herzberg (7) has been used which has been shown to be valid up to $v'' = 21$.

CONCLUSION

While no quantitative intensity measurements have been made it is very clear from the long paths needed for the observation of the $^3\Sigma_u^+ - {}^3\Sigma_g^-$ bands that their intensity is extremely low. The individual bands are very much weaker than the atmospheric oxygen bands which represent a $^1\Sigma_g^+ - {}^3\Sigma_g^-$ magnetic dipole transition. Even the total intensity of the whole $^3\Sigma_u^+ - {}^3\Sigma_g^-$ band system including the continuum is estimated to be less than that of the red atmospheric bands. In view of this low intensity it would appear that the tentative identification of some $^3\Sigma_u^+ - {}^3\Sigma_g^-$ bands with high v'' in the solar spectrum by Babcock (2) is not tenable.

Until now the band system here discussed is the only observed example of a $\Sigma^+ - \Sigma^-$ transition not involving a change of multiplicity. The extremely small transition probability observed for these bands confirms the expectation that the selection rule "Σ^+ states do not combine with Σ^- states" is a very strong rule even though it is not a rigorous one.

As is well known the electron configuration of the ground state of O_2 is

$$(K)(K)(\sigma_g 2s)^2(\sigma_u 2s)^2(\sigma_g 2p)^2(\pi_u 2p)^4(\pi_g 2p)^2$$

which, in addition to the $^3\Sigma_g^-$ state, gives rise to $^1\Sigma_g^+$ and $^1\Delta_g$, the upper states of the red and infrared atmospheric oxygen bands respectively. The first excited electron configuration is

$$(K)(K)(\sigma_g 2s)^2(\sigma_u 2s)^2(\sigma_g 2p)^2(\pi_u 2p)^3(\pi_g 2p)^3$$

which gives rise to the states

$$^1\Sigma_u^+,\ ^1\Sigma_u^-,\ ^1\Delta_u,\ ^3\Sigma_u^+,\ ^3\Sigma_u^-,\ ^3\Delta_u.$$

Of these states, $^3\Sigma_u^-$ and $^3\Sigma_u^+$ are clearly the upper states of the Schumann–Runge system and the band system here under discussion. It appears very probable that $^1\Sigma_u^-$ is the upper state of the new bands briefly mentioned above and that $^3\Delta_u$ is the upper state of the analogue of the ultraviolet O_4 bands. That leaves $^1\Sigma_u^+$ and $^1\Delta_u$ of the above configuration unaccounted for. These two states cannot arise from normal (^3P) atoms (see below), and lie therefore presumably at the level of the $^3\Sigma_u^-$ state or higher. The weak forbidden transitions from the ground state to the states $^1\Sigma_u^+$ and $^1\Delta_u$ would consequently be overlapped by far stronger transitions and would be exceedingly difficult if not impossible to observe. Thus all the states of the lowest excited electron configuration of O_2 are accounted for.

It is interesting to consider the 18 electronic states arising from two normal oxygen atoms:

$$\underline{^1\Sigma_g^+}\ {}^1\Sigma_g^+\ \underline{^1\Sigma_u^-}\ {}^1\Pi_g\ {}^1\Pi_u\ \underline{^1\Delta_g}$$

$$\underline{^3\Sigma_u^+}\ {}^3\Sigma_u^+\ \underline{^3\Sigma_g^-}\ {}^3\Pi_g\ {}^3\Pi_u\ \underline{^3\Delta_u}$$

$$^5\Sigma_g^+\ {}^5\Sigma_g^+\ {}^5\Sigma_u^-\ {}^5\Pi_g\ {}^5\Pi_u\ {}^5\Delta_g.$$

Of these the six underlined states have been observed and belong to the two electron configurations given above. The remaining 12 states have necessarily more highly excited electron configurations and are therefore in all probability unstable. Thus it is very probable that all stable states arising from normal O atoms have been observed.

For very few if any diatomic molecules other than H_2 and He_2 is the information about their electronic structure as complete as for the O_2 molecule. All but one of the transitions on which this information is based are forbidden transitions. This state of affairs emphasizes the need for further work on forbidden transitions of other molecules. In the case of O_2 further work on the higher electronic states that give rise to strong allowed transitions in the far ultraviolet appears desirable.

ACKNOWLEDGMENTS

The experimental part of this investigation was carried out at the Yerkes Observatory. Grateful thanks are due to the authorities of Yerkes Observatory for making this work possible. I am much indebted to Dr. A. E. Douglas for several helpful discussions and suggestions.

REFERENCES

1. ANDERSON, R. S., JOHNSON, C. M., and GORDY, W. Phys. Rev. 83:1060. 1951.
2. BABCOCK, H. D. Astrophys. J. 102:154. 1945.
3. BABCOCK, H. D. and HERZBERG, L. Astrophys. J. 108:167. 1948.
4. BARBIER, D. Ann. d'Astrophys. 10:47. 1947.
5. BURKHALTER, J. H., ANDERSON, R. S., SMITH, W. V., and GORDY, W. Phys. Rev. 79:651. 1950.
6. CHALONGE, D. and VASSY, E. Compt. rend. 198:1318. 1934. J. de Phys. (7) 5:309. 1934.
7. CURRY, J. and HERZBERG, G. Ann. Physik, 19:800. 1934.
8. DUFAY, J. Compt. rend. 213:284. 1941.
9. FINKELNBURG, W. Z. Physik, 90:1. 1934.
10. FINKELNBURG, W. and STEINER, W. Z. Physik, 79:69. 1932.
11. GAYDON, A. G. Dissociation energies. Chapman & Hall, Ltd., London. 1947.
12. HERMAN, L. Compt. rend. 196: 1877. 1933; Ann. Phys. Ser. 11, 11:548. 1939.
13. HERMAN, L. and HERMAN, R. Compt. rend. 201:714. 1935.
14. HERZBERG, G. Z. physik. Chem., B, 4:223. 1929.
15. HERZBERG, G. Naturwissenschaften, 20:577. 1932.
16. HERZBERG, G. *In* The atmospheres of the earth and planets *edited by* G. P. KUIPER. University of Chicago Press. 1949. p. 346.
17. HERZBERG, G. Can. J. Research, A, 28:144. 1950.
18. HERZBERG, G. Molecular spectra and molecular structure. I. Spectra of diatomic molecules. D. Van Nostrand, Inc., New York. 1950.
19. LEWIS, G. N. J. Am. Chem. Soc. 46:2027. 1924.
20. MEINEL, A. B. Repts. Progress Phys. Phys. Soc. (London), 14:121. 1951.
21. PRESENT, R. D. Phys. Rev. 48:140. 1935.
22. SCHLAPP, R. Phys. Rev. 51:342. 1937.
23. SWINGS, P. Astrophys. J. 97:72. 1943.
24. SWINGS, P. *In* The atmospheres of the earth and planets *edited by* G. P. KUIPER. University of Chicago Press. 1949. p. 159.
25. WULF, O. R. Proc. Natl. Acad. Sci. U.S. 14:609. 1928.

SYMMETRICALLY PLACED INDUCTIVE POSTS IN RECTANGULAR WAVE GUIDE[1]

By H. Gruenberg

ABSTRACT

A theoretical expression is derived for the susceptance of two symmetrically placed inductive posts in rectangular wave guide. Universal curves are drawn up that are valid for all rectangular guides in their normal operating range, for different post diameters and offsets. Reasonable agreement has been obtained with experiments at 10.7, 4.74, and 3.20 cm. wave lengths.

Schelkunoff (1) has worked out an expression for the susceptance of a single transverse wire in a wave guide. His work is extended in the following to apply to two symmetrically placed inductive posts. Double posts have been used for some time at the National Research Council for matching purposes. They are simpler and cheaper to install in rectangular wave guide than the usual symmetrical inductive iris. It was also felt that two symmetrically placed posts may have some advantages over a single post. Intuitively, the extent of the higher-order fields might be expected to be smaller in the symmetrical case for the same given susceptance. This is borne out by the fact that no second-order mode is excited in this case. It is thus possible to put the matching structure closer to the load impedance without affecting its susceptance. This is, of course, important for broad-band matching.

The geometry of the problem is shown in Fig. 1. Two metallic circular-cylindrical posts of diameter d are placed symmetrically about the center line of the guide parallel to the narrow dimension of the guide. The inside guide dimensions are a and b respectively, and the centers of the posts are displaced a distance c from the side walls. The susceptance is to be found for the dominant mode (TE_{10}) with the electric vector parallel to the posts.

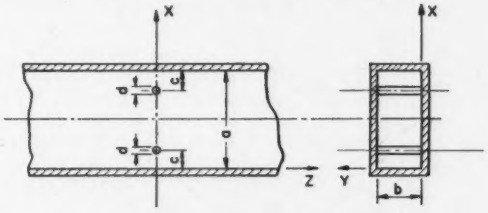

FIG. 1. Geometry of double posts.

It will be assumed that the current in the posts is uniform and that, for the purpose of calculating the fields excited in the guide, the currents are concentrated along the axis of each post. The latter assumption is reasonable as long as the post diameter is small compared with the width of the guide and as long as

[1] *Manuscript received December 6, 1951.*
Contribution from the Radio and Electrical Engineering Division, National Research Council of Canada, Ottawa, Canada. Issued as N.R.C. No. 2728.

the posts do not approach each other or the walls of the guide too closely. From the symmetry of the problem it is also clear that the currents excited in the two posts will be equal in magnitude and phase.

Expanding the wave guide field in a set of orthogonal modes and proceeding exactly as in Schelkunoff's paper, one obtains an expression for the shunt reactance of the double posts which is similar to that for a single post, except that all the even terms are missing:

$$(1)\quad X\frac{\lambda_g}{a} = -\frac{\pi d}{2a} + \csc^2\left(\frac{\pi c}{a}\right)\sum_{\text{odd } m=3}^{\infty}\frac{\sin^2(m\pi c/a)}{m[1-(2a/m\lambda)^2]^{\frac{1}{2}}}\,e^{-(m\pi d/2a)[1-(2a/m\lambda)^2]^{\frac{1}{2}}}$$

where X = normalized shunt reactance,

λ = free-space wave length,

λ_g = guide wave length for the dominant mode,

a = wide dimension of the guide,

c = offset of the posts from the inside guide walls, and

d = diameter of the posts $\ll a$.

Schelkunoff does not give the first term which comes from the first mode ($n = 1$), presumably because it is very small. It will be retained here because it is not negligible in some cases.

The result given in Equation (1) is not of much practical value because of the slow convergence of the series.

Following Schelkunoff we note that for large values of m the terms in the series approach

$$(1/m)\sin^2(m\pi c/a)\,e^{-(m\pi d/2a)}.$$

Hence by adding and subtracting a series of such terms,

$$(2)\qquad X\lambda_g/a = -(\pi d/2a) + \csc^2(\pi c/a)[S+T],$$

where

$$(3)\qquad S = \sum_{\text{odd } m=3}^{\infty}\frac{1}{m}\sin^2\left(\frac{m\pi c}{a}\right)e^{-(m\pi d/2a)}$$

is a series that can be summed, and T is the rapidly converging series

$$(4)\qquad T = \sum_{\text{odd } m=3}^{\infty}\frac{\sin^2(m\pi c/a)}{m}\left\{\frac{e^{-(m\pi d/2a)[1-(2a/m\lambda)^2]^{\frac{1}{2}}}}{[1-(2a/m\lambda)^2]^{\frac{1}{2}}} - e^{-(m\pi d/2a)}\right\}.$$

In the Appendix it is shown that, assuming $d \ll a$ and $d/2 < c < a/2 - d/2$ (i.e., posts not touching the wall nor each other),

$$(5)\qquad S = -(1-\pi d/2a)\sin^2(\pi c/a) - \tfrac{1}{4}[\ln(\pi d/4a) + \ln\cot(\pi c/a)].$$

In normal applications T has a value of from 5 to 20% of that of S. Hence further approximations are justified without seriously affecting the result. This leads to (see Appendix):

$$(6) \qquad T = \left(\frac{\lambda_0}{\lambda}\right)^2 \sum_{\text{odd } m=3}^{\infty} \frac{1}{m^2}\left(\frac{\pi d}{2a} + \frac{1}{m}\right)\left(1 + \frac{1.5}{m^2}\right) \sin^2\left(\frac{m\pi c}{a}\right) e^{-(m\pi d/2a)},$$

where $\lambda_0 = 1.4\,a$, a wave length near which rectangular wave guides are normally operated.

With the above approximations, the normalized susceptance of the posts can be obtained from the relation

$$(7) \qquad \left(B\frac{a}{\lambda_g}\right)^{-1} = -X\frac{\lambda_g}{a} = F\left(\frac{c}{a}, \frac{d}{a}\right) - \left(\frac{\lambda_0}{\lambda}\right)^2 G\left(\frac{c}{a}, \frac{d}{a}\right),$$

where

$$(8) \qquad F\left(\frac{c}{a}, \frac{d}{a}\right) = 1 + \frac{1}{4}\csc^2\left(\frac{\pi c}{a}\right)\left(\ln\frac{\pi d}{4a} + \ln\cot\frac{\pi c}{a}\right),$$

and

$$(9) \qquad G\left(\frac{c}{a}, \frac{d}{a}\right) = \csc^2\left(\frac{\pi c}{a}\right) \sum_{\text{odd } m=3}^{\infty} \frac{1}{m^2}\left(\frac{\pi d}{2a} + \frac{1}{m}\right)\left(1 + \frac{1.5}{m^2}\right) \sin^2\left(\frac{m\pi c}{a}\right) e^{-(m\pi d/2a)}.$$

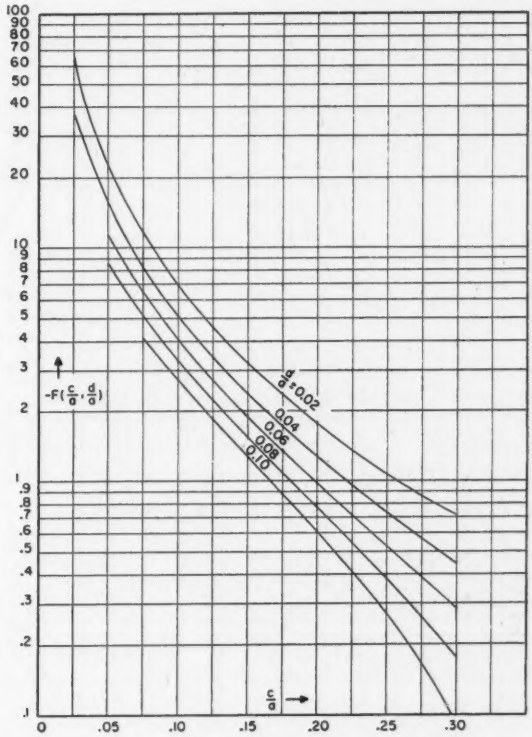

FIG. 2. Plot of $F(\frac{c}{a}, \frac{d}{a})$.

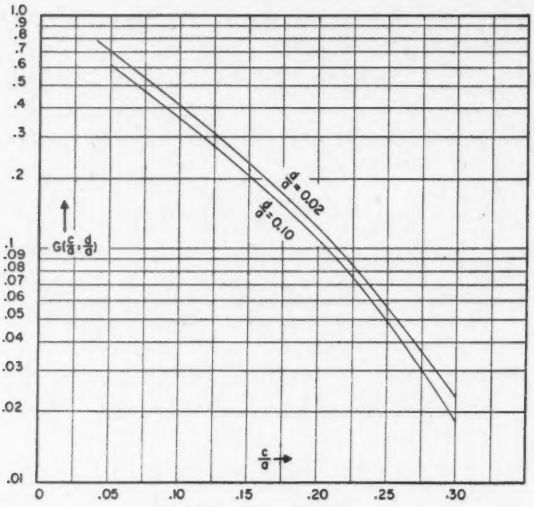

FIG. 3. Plot of $G(\frac{c}{a}, \frac{d}{a})$.

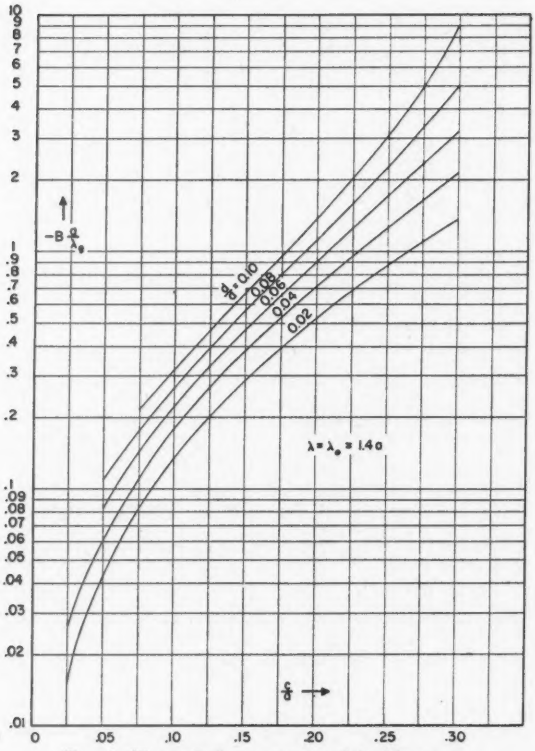

FIG. 4. Theoretical susceptance of double posts.

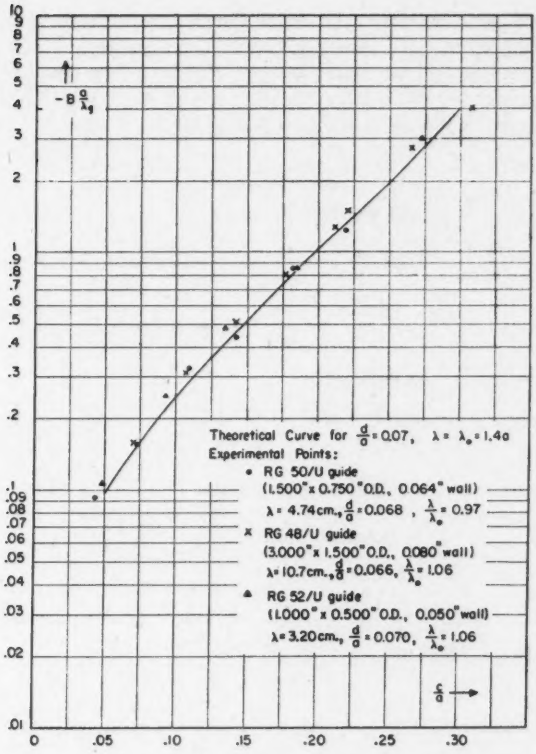

FIG. 5. Post susceptances by experiment.

In most cases λ is close enough to λ_0 so that, for a given post diameter and offset, the susceptance varies linearly with the guide wave length. Even if λ differs from λ_0 by 10%, the corresponding change in B is only between 1 and 4%.

Curves of the functions F and G are plotted in Figs. 2 and 3. Fig. 4 gives universal curves for the post susceptances as a function of post offset and post diameter for a wave length $\lambda_0 = 1.4\ a$.

Fig. 5 shows a comparison between some experimental results and theory. The accuracy of the experiments was probably not better than $\pm$ 5%. Nevertheless, there seems to be reasonably good agreement between the experimental results for different wave guides and frequencies.

It appears, then, that the above simple theory yields values for the susceptance of double posts which are generally too low—perhaps by about 10%. Better results can probably be obtained by variational methods using cosine and sine terms in addition to the constant assumed for the current distribution on the

posts. However, for most practical purposes where the posts are used for correcting mismatches in wave guides, the above theory is sufficiently accurate. If the voltage standing-wave ratio corresponding to the mismatch is less than 6.0, a 10% error in the matching susceptance will still allow a final standing-wave ratio of 1.2 or less. If the original voltage standing-wave ratio is less than 2.6, the final voltage standing-wave ratio will be better than 1.1.

APPENDIX

Schelkunoff (1) quotes the formula

$$\sum_{m=1}^{\infty} \frac{1}{m} e^{-mp} \cos mq = -\frac{1}{2} \ln(1 - 2e^{-p}\cos q + e^{-2p})$$

$$= \frac{1}{2}[p - \ln 2(\cosh p - \cos q)].$$

Replacing q by $\pi - q$, one obtains

$$\sum_{m \text{ even}} \frac{1}{m} e^{-mp} \cos mq - \sum_{m \text{ odd}} \frac{1}{m} e^{-mp} \cos mq = \frac{1}{2}[p - \ln 2(\cosh p + \cos q)].$$

By subtraction the series of odd terms becomes

$$\sum_{\text{odd } m=1}^{\infty} \frac{1}{m} e^{-mp} \cos mq = \frac{1}{4} \ln\left(\frac{\cosh p + \cos q}{\cosh p - \cos q}\right).$$

Hence,

$$\sum_{\text{odd } m=1}^{\infty} \frac{1}{m} e^{-mp} = -\frac{1}{2} \ln \tanh \frac{p}{2},$$

and,

$$\sum_{\text{odd } m=3}^{\infty} \frac{1}{m} e^{-mp} \sin^2 mq = -e^{-p}\sin^2 q + \sum_{\text{odd } m=1}^{\infty} \frac{1}{m} e^{-mp} \sin^2 mq$$

$$= -e^{-p}\sin^2 q + \frac{1}{2} \sum_{\text{odd } m=1}^{\infty} \frac{1}{m} e^{-mp}(1 - \cos 2mq)$$

$$= -e^{-p}\sin^2 q - \frac{1}{4}\left[\ln \tanh \frac{p}{2} + \frac{1}{2} \ln \frac{\cosh p + \cos 2q}{\cosh p - \cos 2q}\right].$$

This is the series of Equation (3) if $p = (\pi d/2a)$ and $q = (\pi c/a)$. For $d \ll a$, one can write $1 - p$ for e^{-p}, and $(p/2)$ for $\tanh(p/2)$. Furthermore, $d/2 < c < a/2 - d/2$ because of the geometry of the system. This allows one to write

$$\frac{1}{2} \ln \frac{\cosh p + \cos 2q}{\cosh p - \cos 2q} \approx \ln \cot q$$

with little error. Hence Equation (3) can be written in the form of Equation (5).

Equation (4) can be written in the form

$$T = \sum_{\text{odd } m=3}^{\infty} \frac{1}{m} \left\{ \frac{e^{-mp[1-(a/m)^2]^{\frac{1}{2}}}}{[1 - (a/m)^2]^{\frac{1}{4}}} - e^{-mp} \right\} \sin^2(mq),$$

with p and q as previously defined, and $\alpha = 2a/\lambda$. For standard wave guides operated in the normal frequency range $\alpha^2 \approx 2$ and hence $(\alpha/m)^2 < 2/9$ for all terms in T. Expanding the above expression in terms of $(\alpha/m)^2$, and omitting higher-order terms, leads to

$$T = \sum_{\text{odd } m=3}^{\infty} \frac{1}{2}\left(\frac{\alpha}{m}\right)^2\left(p + \frac{1}{m}\right)\left[1 + \frac{3}{4}\left(\frac{\alpha}{m}\right)^2\right] \sin^2 mq\, e^{-mp}.$$

The term $(3/4)(\alpha/m)^2$ is negligible compared with unity except in the first or the first two terms in the series. Furthermore, T is considerably smaller than S in normal applications. Negligible error is introduced, therefore, by replacing α by some mean value α_0 in this term. Rectangular wave guides are normally operated at a wave length near $\lambda_0 = 1.4\,a$; hence choosing $\alpha_0^2 = (2a/\lambda_0)^2 \approx 2$, one obtains

$$T = \left(\frac{\lambda_0}{\lambda}\right)^2 \sum_{\text{odd } m=3}^{\infty} \frac{1}{m^2}\left(\frac{\pi d}{2a} + \frac{1}{m}\right)\left(1 + \frac{1.5}{m^2}\right) \sin^2\left(\frac{m\pi c}{a}\right) e^{-(m\pi d/2a)}.$$

REFERENCE

1. SCHELKUNOFF, S. A. Quart. Applied Math. 1: 78. 1943.

THE DYNAMICAL THEORY OF MAGNETIC MONOPOLES[1]

By S. Shanmugadhasan[2]

ABSTRACT

The theory of electric charges and magnetic monopoles has been set up by Dirac by expressing the electromagnetic field tensor in terms of one four-potential and of the variables describing the strings attached to each magnetic monopole. In this reformulation of Dirac's theory the field tensor is expressed in terms of two four-potentials, one corresponding to charges and the other to monopoles, and the action principle for the equations of motion is set up in terms of the two four-potentials and of the tensors dual to them. Thus there is formal symmetry as far as is possible in the treatment of the charges and the monopoles. Also the mathematics is direct and neat. Though the physical content is the same as that of Dirac, a natural generalization of the Fermi form of electrodynamics subject to the restriction that the same particle cannot have both charge and monopole is obtained here.

1. INTRODUCTION

A generalization of the usual electrodynamics has been obtained by Dirac (1,2) by assuming the existence of magnetic monopoles in addition to electric charges. A consequence of this theory is that all the electric charges must be integral multiples of a certain unit of charge and that all the magnetic monopoles must be integral multiples of a certain unit of monopole. The large value of the quantum of monopole required by the theory may explain why monopoles have not been found in nature. Though the theory provides a possible explanation of the quantization of electricity as observed in nature, it is not completely satisfactory in that it does not give the magnitude of the electric charge.

Dirac (2) has set up a dynamical theory of the motion of electric charges and magnetic monopoles interacting with an electromagnetic field by expressing the field tensor in terms of one four-vector potential and of the variables used to describe the strings attached to each monopole. This method of splitting up the field seems rather artificial, and shows a lack of symmetry in handling charges and monopoles. Further, the mathematics is complicated by having to deal with the two-dimensional sheets swept out by the strings in terms of Gaussian coordinates. In the present paper, the device of the strings is eliminated. The field tensor is expressed in terms of two four-potentials, one corresponding to the charges and the other to the monopoles. The action principle for the equations of motion is then set up in terms of these two four-potentials and of the tensors dual to them. With this method, formal symmetry between charges and monopoles is achieved as far as is possible, and the mathematics becomes direct.

The limiting process used to deal with the infinities in the equations of motion, and the method of canonical formulation are taken over from Dirac (2). Since the details of these techniques are omitted here, the present paper

[1] *Manuscript received January 3, 1952.*
Contribution from the Division of Physics, National Research Council, Ottawa, Canada. Issued as N.R.C. No. 2737.
[2] *National Research Council of Canada Postdoctorate Fellow.*

must be read in conjunction with that of Dirac. An examination of the equations of motion shows that the limiting process does not allow the same particle to have both charge and monopole. Subject to the restriction just mentioned. the present treatment provides a natural generalization of the Fermi (4) form of electrodynamics in which the subsidiary equations governing the potentials play an essential role. The physical content, however, is the same as that of Dirac (2).

2. THE CLASSICAL EQUATIONS OF MOTION

The familiar relativistic notation in Lorentz space is used below. Note, however, changes of notation from Dirac (2). Four-vector notation is used whenever convenient. The scalar product $a_\mu b^\mu$ of two four-vectors a_μ, b_μ is denoted by $(\mathbf{a}, \mathbf{b})$. s is the proper-time, and a dot denotes differentiation with respect to s. The typical particle point, whether that of an electric charge e or a magnetic monopole g, is z_μ, and its velocity is v_μ. The world-point is x_μ, and the operator of differentiation $\partial/\partial x^\mu$ is denoted by ∂_μ. The tensor dual to the electromagnetic field tensor $F_{\mu\nu}$ is defined by $F^*_{\mu\nu} = \frac{1}{2}\epsilon_{\mu\nu\rho\sigma}F^{\rho\sigma}$. $\epsilon_{\mu\nu\rho\sigma}$ is a tensor antisymmetric in all its indices and such that $\epsilon_{0123} = 1$. Other dual tensors are also formed with the help of $\epsilon_{\mu\nu\rho\sigma}$. The following relations satisfied by $\epsilon_{\mu\nu\rho\sigma}$ are used below

$$-\epsilon_{\mu\nu\rho\sigma}\epsilon^{\mu\alpha\beta\gamma} = \delta^\alpha_\nu\delta^\beta_\rho\delta^\gamma_\sigma + \delta^\alpha_\rho\delta^\beta_\sigma\delta^\gamma_\nu + \delta^\alpha_\sigma\delta^\beta_\nu\delta^\gamma_\rho - \delta^\beta_\nu\delta^\alpha_\rho\delta^\gamma_\sigma - \delta^\beta_\rho\delta^\alpha_\sigma\delta^\gamma_\nu - \delta^\beta_\sigma\delta^\alpha_\nu\delta^\gamma_\rho,$$

$$-\epsilon_{\mu\nu\rho\sigma}\epsilon^{\mu\nu\alpha\beta} = 2(\delta^\alpha_\rho\delta^\beta_\sigma - \delta^\alpha_\sigma\delta^\beta_\rho),$$

$$-\epsilon_{\mu\nu\rho\sigma}\epsilon^{\mu\nu\rho\alpha} = 6\delta^\alpha_\sigma,$$

where the δ's are Kronecker symbols. $\delta(\mathbf{x})$ is written for the Dirac δ function $\delta(x_0)\delta(x_1)\delta(x_2)\delta(x_3)$. $\mathbf{dx}$ stands for $dx_0dx_1dx_2dx_3$.

The classical scheme of equations of motion consists of

$$\partial^\nu \tilde{F}_{\mu\nu} = -4\pi\Sigma_e e\int v_\mu\delta(\mathbf{x}-\mathbf{z})ds, \tag{2.1}$$

$$\partial^\nu F^*_{\mu\nu} = -4\pi\Sigma_g g\int v_\mu\delta(\mathbf{x}-\mathbf{z})ds \tag{2.2}$$

for the field,

$$m\dot{v}_\mu = ev^\nu F_{\mu\nu}(\mathbf{z}) \tag{2.3}$$

for a charge, and

$$m\dot{v}_\mu = gv^\nu \tilde{F}^*_{\mu\nu}(\mathbf{z}) \tag{2.4}$$

for a monopole, where Σ_e denotes the sum over all the charges. The usual infinities in the equations of motion are avoided by a limiting process, which introduces the field quantity $\tilde{U}(\mathbf{x})$ associated with $U(\mathbf{x})$ according to

$$\tilde{U}(\mathbf{x}) = \int U(\mathbf{x}')\gamma(\mathbf{x}-\mathbf{x}')\mathbf{dx}', \quad U(\mathbf{x}) = \int \tilde{U}(\mathbf{x}')\Gamma(\mathbf{x}-\mathbf{x}')\mathbf{dx}'.$$

The function $\gamma(\mathbf{x})$, which approximates to $\delta(\mathbf{x})$ and tends to it in the limit, is left arbitrary except to state those properties necessary to put the equations of motion into canonical form. Equation (2.2) is equivalent to

$$\partial_\rho F_{\mu\nu} + \partial_\mu F_{\nu\rho} + \partial_\nu F_{\rho\mu} = 4\pi\epsilon_{\mu\nu\rho\sigma} \Sigma_g g \int v^\sigma \delta(\mathbf{x} - \mathbf{z}) ds. \tag{2.5}$$

In the ordinary electrodynamics with electric charges only, the field tensor $F_{\mu\nu}$ satisfies the equation $\partial^\nu F^*_{\mu\nu} = 0$. Hence it is a simple six-vector, and can be expressed in terms of one four-potential in the usual manner. This is not true in the present case, and the field tensor is a general six-vector. Then split up $F_{\mu\nu}$ with respect to the symbolic four-vector ∂_μ according to

$$F_{\mu\nu} = G^*_{\mu\nu} + E_{\mu\nu} = G^*_{\mu\nu} + \partial_\mu A_\nu - \partial_\nu A_\mu, \tag{2.6}$$

where

$$\partial^\nu G^*_{\mu\nu} = 0, \tag{2.7}$$

$$\partial^\mu A_\mu = 0. \tag{2.8}$$

From (2.7), let

$$G_{\mu\nu} = -(\partial_\mu B_\nu - \partial_\nu B_\mu), \tag{2.9}$$

where

$$\partial^\mu B_\mu = 0. \tag{2.10}$$

Thus, from (2.6) and (2.9), one has

$$F_{\mu\nu} = \partial_\mu A_\nu - \partial_\nu A_\mu - \epsilon_{\mu\nu\rho\sigma}\partial^\rho B^\sigma = \partial_\mu A_\nu - \partial_\nu A_\mu + \partial^\rho B_{\mu\nu\rho}, \tag{2.11}$$

$$F^*_{\mu\nu} = \partial_\mu B_\nu - \partial_\nu B_\mu + E^*_{\mu\nu}, \tag{2.12}$$

where $B_{\mu\nu\rho} = -\epsilon_{\mu\nu\rho\sigma}B^\sigma$, and $\partial^\nu E^*_{\mu\nu} = 0$ or its equivalent

$$\partial_\rho E_{\mu\nu} + \partial_\mu E_{\nu\rho} + \partial_\nu E_{\rho\mu} = 0. \tag{2.13}$$

The above method of splitting up $F_{\mu\nu}$ can then be introduced into the equations (2.1) to (2.5). The equations corresponding to (2.8) and (2.10)

$$\partial^\mu \tilde{A}_\mu = 0, \ \partial^\mu B_\mu = 0 \tag{2.14}$$

are introduced as subsidiary conditions. These subsidiary conditions are essential with the Fermi (4) form of electrodynamics considered here. But electrodynamics can be built up without using these subsidiary conditions, as Dirac (3) has done recently.

$\tilde{A}_\mu$ and B_μ satisfy the equations

$$\Box \tilde{A}_\mu(\mathbf{x}) = 4\pi \Sigma_e e \int v_\mu \delta(\mathbf{x} - \mathbf{z}) ds, \quad \Box \equiv \partial^\mu \partial_\mu, \tag{2.15}$$

$$\Box B_\mu(\mathbf{x}) = 4\pi \Sigma_g g \int v_\mu \delta(\mathbf{x} - \mathbf{z}) ds. \tag{2.16}$$

With the help of the Lorentz invariant function $J(\mathbf{x})$, defined by

$$J(\mathbf{x}) = 2\delta(\mathbf{x}^2), \quad x_0 > 0,$$

$$= 0 \quad , \quad x_0 < 0,$$

so that $\Box J(\mathbf{x}) = 4\pi\delta(\mathbf{x})$, the contributions of a charge e and a monopole g to the retarded potentials are

$$(2.17)\qquad \tilde{A}_\mu^{\text{ret.}}(\mathbf{x}) = e\int_{-\infty}^{\infty} v_\mu J(\mathbf{x}-\mathbf{z})ds, \qquad B_\mu^{\text{ret.}}(\mathbf{x}) = g\int_{-\infty}^{\infty} v_\mu J(\mathbf{x}-\mathbf{z})ds,$$

respectively. Hence it is clear that for the equations of motion (2.3) and (2.4) not to involve infinities, the same particle cannot have both charge and monopole, and the world-lines of the charges should not cross the world-lines of the monopoles.

3. THE ACTION PRINCIPLE

The action integral I which gives correctly the equations of motion is the sum of four terms $I_1 + I_2 + I_3 + I_4$, where

$$(3.1)\qquad I_1 = \Sigma_{e+g} m\int ds,$$

$$(3.2)\qquad I_2 = \Sigma_e e\int (\mathbf{v}, \mathbf{A}(\mathbf{z}))ds,$$

$$(3.3)\qquad I_3 = \Sigma_g g\int (\mathbf{v}, \tilde{\mathbf{B}}(\mathbf{z}))ds = \tfrac{1}{6}\Sigma_g \epsilon_{\mu\nu\rho\sigma} g\int v^\sigma \tilde{B}^{\mu\nu\rho} ds,$$

$$I_4 = (16\pi)^{-1}\int\int F_{\mu\nu}(\mathbf{x})F^{\mu\nu}(\mathbf{x}')\gamma(\mathbf{x}-\mathbf{x}')\mathbf{dx}\,\mathbf{dx}'$$

$$= (16\pi)^{-1}\int\int \{E_{\mu\nu}(\mathbf{x})E^{\mu\nu}(\mathbf{x}')\gamma(\mathbf{x}-\mathbf{x}')$$

$$(3.4)\qquad + \tilde{G}^*_{\mu\nu}(\mathbf{x})\tilde{G}^{*\mu\nu}(\mathbf{x}')\Gamma(\mathbf{x}-\mathbf{x}') + 2E_{\mu\nu}(\mathbf{x})G^{*\mu\nu}(\mathbf{x}')\gamma(\mathbf{x}-\mathbf{x}')\}\mathbf{dx}\,\mathbf{dx}'.$$

The property $\gamma(\mathbf{x}) = \gamma(-\mathbf{x})$ is necessary to deduce the equations of motion from this variational principle.

The quantities to be varied in the above action function are the particle variables z^μ and the field variables $A^\mu(\mathbf{x})$, $\tilde{B}^{\mu\nu\rho}(\mathbf{x})$. Such variations in (3.1), (3.2), and (3.3) give

$$(3.5)\qquad \delta I_1 = -\Sigma_{e+g} m\int \dot{v}_\mu \delta z^\mu ds,$$

$$(3.6)\qquad \delta I_2 = \Sigma_e e\int v^\nu\{(\partial_\mu A_\nu - \partial_\nu A_\mu)_{\mathbf{x}=\mathbf{z}}\delta z^\mu + (\delta A_\nu)_{\mathbf{x}=\mathbf{z}}\}ds,$$

$$(3.7)\qquad \delta I_3 = \Sigma_g g\int \{v^\nu(\partial_\mu \tilde{B}_\nu - \partial_\nu \tilde{B}_\mu)_{\mathbf{x}=\mathbf{z}}\delta z^\mu + \tfrac{1}{6}\epsilon_{\mu\nu\rho\sigma}v^\sigma(\delta\tilde{B}^{\mu\nu\rho})_{\mathbf{x}=\mathbf{z}}\}ds.$$

The variation of the first term of I_4 in (3.4) gives

$$(8\pi)^{-1}\int\int E_{\mu\nu}(\mathbf{x}')\delta E^{\mu\nu}(\mathbf{x})\gamma(\mathbf{x}-\mathbf{x}')\mathbf{dx}\,\mathbf{dx}' = (8\pi)^{-1}\int \tilde{E}_{\mu\nu}(\mathbf{x})\delta E^{\mu\nu}(\mathbf{x})\mathbf{dx}$$

$$(3.8)\qquad = -(4\pi)^{-1}\int \tilde{E}_{\mu\nu}\partial^\nu \delta A^\mu \mathbf{dx} = (4\pi)^{-1}\int (\partial^\nu \tilde{E}_{\mu\nu})\delta A^\mu \mathbf{dx}.$$

The variation of the second term gives

$$(8\pi)^{-1}\int\int \tilde{G}^*_{\mu\nu}(\mathbf{x}')\delta\tilde{G}^{*\mu\nu}(\mathbf{x})\Gamma(\mathbf{x}-\mathbf{x}')\mathbf{dx}\mathbf{dx}' = (8\pi)^{-1}\int G^*_{\mu\nu}(\mathbf{x})\delta\tilde{G}^{*\mu\nu}(\mathbf{x})\mathbf{dx}$$

$$= -(8\pi)^{-1}\int G_{\mu\nu}(\mathbf{x})\delta\tilde{G}^{\mu\nu}(\mathbf{x})\mathbf{dx} = (8\pi)^{-1}\int G^*_{\mu\nu}\partial_\rho\delta\tilde{B}^{\mu\nu\rho}\mathbf{dx}$$

$$= -(24\pi)^{-1}\int(\partial_\rho G^*_{\mu\nu} + \partial_\mu G^*_{\nu\rho} + \partial_\nu G^*_{\rho\mu})\delta\tilde{B}^{\mu\nu\rho}\mathbf{dx}. \tag{3.9}$$

The third term of I_4 in (3.4) gives, in addition to the contribution due to the variations $\delta A^\mu(\mathbf{x})$ and $\delta\tilde{B}^{\mu\nu\rho}(\mathbf{x})$, a contribution due to the variation of the world-lines of the particles. The first contribution is conveniently obtained by writing the integrand as $E_{\mu\nu}\tilde{G}^{*\mu\nu}$ and gives

$$(8\pi)^{-1}\int(\tilde{G}^*_{\mu\nu}\delta E^{\mu\nu} + E_{\mu\nu}\partial_\rho\delta\tilde{B}^{\mu\nu\rho})\mathbf{dx}$$

$$= (4\pi)^{-1}\int\{(\partial^\nu G^*_{\mu\nu})\delta A^\mu - \tfrac{1}{6}(\partial_\rho E_{\mu\nu} + \partial_\mu E_{\nu\rho} + \partial_\nu E_{\rho\mu})\delta\tilde{B}^{\mu\nu\rho}\}\mathbf{dx}. \tag{3.10}$$

The second contribution due to the variation δz^μ is obtained by writing the integrand as $\tilde{E}_{\mu\nu}G^{*\mu\nu}$. Because of the dependence of $\tilde{E}_{\mu\nu}$ and $G^*_{\mu\nu}$ on $\mathbf{x}$ and $\mathbf{z}$ according to (2.1), (2.2) (as can also be seen from (2.17)), the operation $\partial/\partial z^\mu$ on these quantities is just equal to the operation $-\partial_\mu$ on the same quantities. From (2.13) and (2.5), one gets

$$G^{*\nu\rho}\partial_\mu\tilde{E}_{\nu\rho} = -2G^{*\nu\rho}\partial_\rho\tilde{E}_{\mu\nu},$$

$$\tilde{E}^{\nu\rho}\partial_\mu G^*_{\nu\rho} = -2\tilde{E}^{\nu\rho}\partial_\rho G^*_{\mu\nu} + 4\pi\tilde{E}^{\nu\rho}\epsilon_{\mu\nu\rho\sigma}\Sigma_g g\int v^\sigma\delta(\mathbf{x}-\mathbf{z})ds$$

$$= -2\tilde{E}^{\nu\rho}\partial_\rho G^*_{\mu\nu} - 8\pi\tilde{E}^*_{\mu\nu}\Sigma_g g\int v^\nu\delta(\mathbf{x}-\mathbf{z})ds.$$

Thus, with the help of these results, the second contribution is

$$-(8\pi)^{-1}\int(\delta z^\mu G^{*\nu\rho}\partial_\mu\tilde{E}_{\nu\rho} + \delta z^\mu\tilde{E}^{\nu\rho}\partial_\mu G^*_{\nu\rho})\mathbf{dx}$$

$$= (4\pi)^{-1}\int(\delta z^\mu G^{*\nu\rho}\partial_\rho\tilde{E}_{\mu\nu} + \delta z^\mu\tilde{E}^{\nu\rho}\partial_\rho G^*_{\mu\nu})\mathbf{dx}$$

$$+\int\int\Sigma_g\tilde{E}^*_{\mu\nu}v^\nu\delta(\mathbf{x}-\mathbf{z})\delta z^\mu ds\,\mathbf{dx}$$

$$= \Sigma_e\int eG^*_{\mu\nu}v^\nu\delta z^\mu ds + \Sigma_g\int g\tilde{E}^*_{\mu\nu}v^\nu\delta z^\mu ds. \tag{3.11}$$

The total variation of I is obtained by adding the expressions (3.5) to (3.11). The field equations (2.1), (2.5) are obtained correctly by equating the coefficients of δA^μ and $\delta\tilde{B}^{\mu\nu\rho}$ to zero. The particle equations (2.3), (2.4) are obtained by equating the coefficient of the corresponding δz^μ to zero. The field

equations are obtained first independently of (3.11), so that their subsequent use in evaluating (3.11) is justified.

In order that the momenta conjugate to A_0 and to the dual to $\tilde{B}_0$ may not vanish, it is necessary to add to the above action integral, as Fermi (4) has done, a further term

$$I_5 = (8\pi)^{-1}\int\{(\partial_\mu\tilde{A}_\nu)(\partial^\nu A^\mu) - (\partial_\mu B_\nu)(\partial^\nu\tilde{B}^\mu)\}\,\mathbf{dx}.$$

Since

$$\delta I_5 = -(4\pi)^{-1}\int\{(\partial^\nu\partial_\mu\tilde{A}_\nu)\delta A^\mu - (\partial^\nu\partial_\mu B_\nu)\delta\tilde{B}^\mu\}\,\mathbf{dx},$$

this contribution does not affect the equations of motion in view of the subsidiary equations (2.14).

4. THE CANONICAL FORMULATION AND QUANTIZATION

The canonical formulation follows closely the methods of Dirac (2). The action integrals I_1, I_2, I_3 are stopped at a space-like three-dimensional surface S_P, where the particles are supposed to go out of existence, while I_4, I_5 are stopped at a much later surface S_F, where the field is supposed to go out of existence. Then, from (2.15) and (2.16), in the region between S_P and S_F, $\Box\tilde{\mathbf{A}}(\mathbf{x}) = 0$, $\Box\mathbf{B}(\mathbf{x}) = 0$. By suitable choice of the function $\gamma(\mathbf{x})$, the equations $\Box\mathbf{A}(\mathbf{x}) = 0$, $\Box\tilde{\mathbf{B}}(\mathbf{x}) = 0$ are arranged to hold even at the points where the particles go out of existence. Under these conditions, the Fourier expansions for the potentials are

$$\begin{cases} A_\mu(\mathbf{x}) = \Sigma_{k_0}\int A_{\mathbf{k}\mu}e^{i(\mathbf{k},\mathbf{x})}\partial k, \quad \tilde{A}_\mu(\mathbf{x}) = \Sigma_{k_0}\int\tilde{A}_{\mathbf{k}\mu}e^{i(\mathbf{k},\mathbf{x})}\partial k, \\ B_\mu(\mathbf{x}) = \Sigma_{k_0}\int B_{\mathbf{k}\mu}e^{i(\mathbf{k},\mathbf{x})}\partial k, \quad \tilde{B}_\mu(\mathbf{x}) = \Sigma_{k_0}\int\tilde{B}_{\mathbf{k}\mu}e^{i(\mathbf{k},\mathbf{x})}\partial k, \end{cases} \tag{4.1}$$

where $k_0 = \pm(k_1^2 + k_2^2 + k_3^2)^{\frac{1}{2}}$, $\partial k = k_0^{-1}dk_1dk_2dk_3$, and Σ_{k_0} denotes the sum over both values of k_0 for given k_1, k_2, k_3. Also, $\tilde{A}_{\mathbf{k}\mu} = \gamma_{\mathbf{k}}A_{\mathbf{k}\mu}$, $\tilde{B}_{\mathbf{k}\mu} = \gamma_{\mathbf{k}}B_{\mathbf{k}\mu}$, where $\gamma_{\mathbf{k}}$ is obtained by the Fourier resolution of $\gamma(\mathbf{x})$. In the region between S_P and S_F, the subsidiary equations (2.14) become

$$\partial^\nu\tilde{A}_\nu + \Sigma_e eJ(\mathbf{x} - \mathbf{z}) = 0, \quad \partial^\nu B_\nu + \Sigma_g gJ(\mathbf{x} - \mathbf{z}) = 0. \tag{4.2}$$

The action integral bounded as above is now varied allowing S_P to vary but not S_F. The boundary terms from δI_1, δI_2, and δI_3 together are

$$\Sigma_{e+g}mv_\mu\Delta z^\mu + \Sigma_e eA_\mu(\mathbf{z})\Delta z^\mu + \Sigma_g g\tilde{B}_\mu(\mathbf{z})\Delta z^\mu, \tag{4.3}$$

where Δz^μ is the total variation of z^μ at the point where the particle goes out of existence. In forming δI_4 the third term in (3.4) describing the interaction of the field of the charges with the field of the monopoles becomes

$$\int_{-\infty}^{\infty}\int E_{\mu\nu}(\mathbf{x})G^{*\mu\nu}(\mathbf{x}')\gamma(\mathbf{x} - \mathbf{x}')\mathbf{dx}\,\mathbf{dx}', \tag{4.4}$$

provided that S_F is sufficiently far from S_P, so that $\gamma(\mathbf{x} - \mathbf{x}') = 0$ for $\mathbf{x}$ earlier than S_P and $\mathbf{x}'$ later than S_F. The boundary contribution from δI_5 and the remaining two terms of δI_4 is

$$(4.5) \qquad (8\pi)^{-1}\int\{(\partial_\nu\tilde{A}_\mu)\delta A^\mu + (\partial_\nu A_\mu)\delta\tilde{A}^\mu - (\partial_\nu B_\mu)\delta\tilde{B}^\mu - (\partial_\nu\tilde{B}_\mu)\delta B^\mu\}dS^\nu,$$

where dS^ν is an element of the three-dimensional surface S_F over which the integral is taken. The expression (4.5) evaluated in terms of the Fourier expansions (4.1) gives, after discarding terms which are perfect differentials,

$$(4.6) \qquad -4\pi^2\mathrm{i}\int\gamma_{\mathbf{k}}(\bar{A}_{\mathbf{k}\mu}\delta A_{\mathbf{k}}{}^\mu - \bar{B}_{\mathbf{k}\mu}\delta B_{\mathbf{k}}{}^\mu)\partial k$$

$$= -4\pi^2\mathrm{i}\int\gamma_{\mathbf{k}}(\bar{A}_{\mathbf{k}\mu}\delta A_{\mathbf{k}}{}^\mu + \bar{B}_{\mathbf{k}\mu\nu\rho}\delta B_{\mathbf{k}}{}^{\mu\nu\rho})\partial k,$$

where a bar over any quantity denotes its conjugate complex.

The canonical coordinates and momenta can be written down from the boundary formula. Hence, the fundamental Poisson Brackets (P.B.'s hereafter) are

$$(4.7) \qquad \begin{cases} [p_\mu, z_\nu] = g_{\mu\nu}, \\ [\bar{A}_{\mathbf{k}\mu}, A_{\mathbf{k}'\nu}] = -[\bar{B}_{\mathbf{k}\mu}, B_{\mathbf{k}'\nu}] \\ \qquad\qquad = \mathrm{i}(4\pi^2\gamma_{\mathbf{k}})^{-1}g_{\mu\nu}k_0\delta(k_1 - k_1')\delta(k_2 - k_2')\delta(k_3 - k_3'), \end{cases}$$

with all the other P.B.'s vanishing. The Hamilton-Jacobi equations are

$$(4.8) \qquad (\mathbf{p} - e\mathbf{A}(\mathbf{z}))^2 - m^2 = 0$$

for each electric charge, and

$$(4.9) \qquad (\mathbf{p} - g\tilde{\mathbf{B}}(\mathbf{z}))^2 - m^2 = 0$$

for each magnetic monopole, where the potentials $\mathbf{A}(\mathbf{z})$, $\tilde{\mathbf{B}}(\mathbf{z})$ are given by (4.1). The subsidiary equations (4.2) provide the Hamilton-Jacobi equations for the field, which are, in terms of Fourier components with $k_0 > 0$,

$$(4.10) \qquad \begin{cases} \gamma_{\mathbf{k}}\,(\mathbf{k}, \mathbf{A}_{\mathbf{k}}) - (4\pi^2)^{-1}\Sigma_e\, e e^{-\mathrm{i}(\mathbf{k},\mathbf{z})} = 0, \\ \gamma_{\mathbf{k}}\,(\mathbf{k}, \bar{\mathbf{A}}_{\mathbf{k}}) - (4\pi^2)^{-1}\Sigma_e\, e e^{\mathrm{i}(\mathbf{k},\mathbf{z})} = 0, \\ (\mathbf{k}, \mathbf{B}_{\mathbf{k}}) - (4\pi^2)^{-1}\Sigma_g\, g e^{-\mathrm{i}(\mathbf{k},\mathbf{z})} = 0, \\ (\mathbf{k}, \bar{\mathbf{B}}_{\mathbf{k}}) - (4\pi^2)^{-1}\Sigma_g\, g e^{\mathrm{i}(\mathbf{k},\mathbf{z})} = 0. \end{cases}$$

All the Hamilton-Jacobi equations (4.8) to (4.10) are seen to be self-consistent by verifying that the P.B.'s of their left-hand sides all vanish.

The varied point $\mathbf{z}$ on the new S_P can be reached by more than one path. The action integral is single-valued only if the second path can be continuously deformed into the first in such a way that during this deformation process the

path has the same initial and final $\mathbf{z}$ values and satisfies the equations of motion. The second path of a charged particle which loops round a monopole cannot be continuously deformed into a direct path because the deformed path must not pass through the monopole. A similar situation holds for the path of a monopole looping round a charge. Therefore the action integral considered above is many-valued.

The uncertainty in the action integral is calculated as follows. During the variation of the path of a particle round a second particle the world-line of the varied particle sweeps out a closed two-dimensional surface σ lying in S_P and enclosing the second particle. The change in the action integral due to this looping process arises from the term (4.4), which, from (3.11), leads to expressions of the form

$$(4.11)\quad \Sigma_e \int_\sigma eG^*_{\mu\nu} dz^\nu \delta z^\mu + \Sigma_g \int_\sigma g\tilde{E}^*_{\mu\nu} dz^\nu \delta z^\mu = \Sigma_e e \int_\sigma \tfrac{1}{2} G^*_{\mu\nu} d\sigma^{\mu\nu} + \Sigma_g g \int_\sigma \tfrac{1}{2} \tilde{E}^*_{\mu\nu} d\sigma^{\mu\nu},$$

where $d\sigma^{\mu\nu}$ is an element of the two-dimensional surface σ. (In forming the variation δz^μ of $z^\mu(s)$, the latter is considered as embedded in a sufficiently smooth family of functions $z^\mu(s,\tau)$, where τ is the parameter of the family and where $z^\mu(s,0) = z^\mu(s)$. Then $dz^\mu = ds\partial z^\mu(s,0)/\partial s$, and $\delta z^\mu = d\tau \partial z^\mu(s,0)/\partial \tau$. This explains how $d\sigma^{\mu\nu} = \delta z^\mu dz^\nu - \delta z^\nu dz^\mu$ gives the element of σ.) If σ encloses a monopole g once, then the first integral on the right-hand side of (4.11) is $4\pi g$. Similarly, if σ encloses a charge e once, the second integral on the right-hand side of (4.11) is $4\pi e$. The surface σ may enclose a particle more than once, and may enclose several particles at the same time. When all these factors are taken into account, the total uncertainty in I is

$$(4.12)\qquad 4\pi \Sigma_{ge} m_{ge} ge,$$

where m_{ge} is an arbitrary integral coefficient and the sum is taken over all the charges e and monopoles g.

The transition to the quantum theory from the above canonical formulation is carried out by the usual rules. The P.B.'s provide the commutation relations for the operators corresponding to the dynamical variables. Since the Hamilton-Jacobi equations provide the Schrödinger equations of the quantum theory, the wave equations for the charges are similar to those for the monopoles in the present theory. The uncertainty (4.12) in the action integral leads to the quantization of charges and monopoles as in the work of Dirac (2).

I am indebted to Miss Lorraine Ourom for help with the manuscript. My thanks are due to Dr. G. Herzberg for kind encouragement and research facilities, and to the National Research Council of Canada for financial support.

Note added in proof. Some of the work recently announced by Melvin (5) seems similar in scope to the above.

REFERENCES

1. Dirac, P. A. M. Proc. Roy. Soc. (London), A, 133: 60. 1931.
2. Dirac, P. A. M. Phys. Rev. (Ser. 2), 74: 817. 1948.
3. Dirac, P. A. M. Can. J. Math. 3: 1. 1951.
4. Fermi, E. Revs. Modern Phys. 4: 87. 1932.
5. Melvin, M. A. Bull. Am. Phys. Soc. 27, No. 2: Abstract C4. March, 1952.

SPINORS IN THE DYNAMICAL THEORY OF SPINNING PARTICLES[1]

By S. Shanmugadhasan[2]

ABSTRACT

The correspondence between self-dual six-vectors and symmetric spinors of the second rank is used to put into spinor form the rotational equations of motion of a particle analogous to a pure gyroscope or to a symmetrical top. These equations are then split up into an equivalent system of equations in terms of spinors of the first rank. The Lagrangian of each system is set up, and the canonically conjugate variables obtained from it in terms of covariant spinors. But the canonical variables, being not all independent, lead to weak equations in the sense of Dirac. Therefore, Dirac's generalized Hamiltonian dynamics is used in the canonical formulation in terms of Poisson Brackets. The detailed discussion of the symmetrical top case shows that, though the fundamental Poisson Brackets for the total spin angular momentum and the "spin" are the usual ones, those Poisson Brackets involving the derivative of the "spin" are not unique.

INTRODUCTION

The quantization of the classical theory of spinning particles has been considered in two previous papers (2,3). For this purpose the Poisson Brackets (P.B.'s hereafter) of the rotational variables have been obtained in paper (3) by setting up the variational principle for the rotational equations of motion. The two cases of particular interest are those in which the rotational behavior of the particle is analogous to a pure gyroscope or to a symmetrical top. It is found that quasi-coordinates are necessary to formulate the action function in covariant vector or tensor form. The canonically conjugate variables deduced from this action principle are not in vector or tensor form, and therefore the basic P.B.'s do not exhibit their Lorentz invariant nature.

It is known that there is a one–one correspondence between self-dual six-vectors or the complex three-vectors arising from them and the two-component spinors of van der Waerden. Therefore the rotational equations of motion can be written in terms of spinors. The Lagrangian for these equations can be set up in terms of spinors without using quasi-coordinates. Then the canonically conjugate variables are spinors which show explicitly their Lorentz invariance. The momenta deduced from this Lagrangian are not independent functions of the velocities. Therefore the dynamical theory involves strong and weak equations in the sense of Dirac (1). The further discussion then follows the generalized Hamiltonian dynamics considered by Dirac (1) to deal with such systems.

The canonical formulation in the case of the symmetrical top displays all the interesting features of Dirac's theory. The P.B.'s for the total spin angular momentum and the "spin", which are the usual ones, always remain the same and independent of the representation used. But the P.B.'s involving the derivative of the "spin" are not unique since they depend on the choice of the

[1] *Manuscript received November 30, 1951.*
Contribution from the Division of Physics, National Research Council, Ottawa, Canada. Issued as N.R.C. No. 2736.
[2] *Holder of a National Research Council of Canada Postdoctorate Fellowship.*

Hamiltonian and the representation. When the two invariant squares of the "spin" tensor are strongly constant, and the two invariant scalar products of the "spin" tensor and its derivative vanish strongly, the P.B.'s obtained here agree with those previously obtained in paper (3) under the same conditions.

SPINOR FORM OF THE ROTATIONAL EQUATIONS OF MOTION

The tensor notation (with Greek indices) and the complex three-vector notation used below are exactly as in paper (3), unless otherwise stated. Latin indices taking values 1, 2 are used as spinor indices. A summary of the two-component spinor formalism is found in Taub (4), but the bridge spinors used by Taub to connect tensors with spinors are different from those used below. The following conventions may be noted explicitly. The antisymmetric spinors ϵ^{ij} and ϵ_{ij}, defined by

$$\epsilon^{12} \equiv -\epsilon^{21} \equiv \epsilon_{12} \equiv -\epsilon_{21} \equiv 1, \quad \epsilon^{11} \equiv \epsilon^{22} \equiv \epsilon_{11} \equiv \epsilon_{22} \equiv 0,$$

are used for raising and lowering an undotted spinor index according to the formulae

$$a^i \equiv \epsilon^{ij} a_j, \quad a_i \equiv \epsilon_{ji} a^j.$$

If $$\mathbf{s} \equiv (s_1, s_2, s_3) \equiv (S_{23} + iS_{01}, S_{31} + iS_{02}, S_{12} + iS_{03})$$

is the three-vector from the self-dual tensor obtained from $S_{\mu\nu}$, then the symmetric spinor s_{ij} corresponding to this three-vector (or self-dual tensor) has the components

$$(1) \qquad \begin{cases} s_{11} \equiv -(s_1 + is_2), & s_{22} \equiv s_1 - is_2, & s_{12} \equiv s_{21} \equiv s_3, \\ s^1_{\cdot 1} \equiv s_3, & s^1_{\cdot 2} \equiv s_1 - is_2, & s^2_{\cdot 1} \equiv s_1 + is_2, & s^2_{\cdot 2} \equiv -s_3, \\ s^{11} \equiv s_1 - is_2, & s^{12} \equiv s^{21} \equiv -s_3, & s^{22} \equiv -(s_1 + is_2). \end{cases}$$

The spinor corresponding to a tensor is denoted by the corresponding lower case letter with Latin indices. Scalar products and invariant squares of symmetric spinors such as $s_{ij}f^{ij}$ and $s_{ij}s^{ij}$ are written as (sf) and s^2 respectively.

In discussing the Hamiltonian dynamics of the systems under consideration the present paper follows the methods and terminology of Dirac (1). Two types of equations occur in the theory, and they are distinguished by writing the weak equations with the usual equality sign $=$ and by writing the strong equations with the sign $\equiv$.

Consider the rotational equation for a pure gyroscope

$$(2) \qquad \dot{\mathbf{s}} = 2C[\mathbf{s} \times \mathbf{f}].$$

With the help of (1), equation (2) takes the spinor form

$$(3) \qquad \dot{s}_{ij} = -iC(s_{ik}f^{k}_{\cdot j} + s_{jk}f^{k}_{\cdot i}).$$

Since s_{ij} is symmetric, it can be split up in the form

$$(4) \qquad s_{ij} \equiv a_i b_j + a_j b_i,$$

where a_i, b_i are spinors of the first rank. Since

$$s^2 \equiv -2\mathbf{s}^2 \equiv -2(a_i b^i)^2 = \text{constant},$$

the splitting up (4) is subject to the condition

$$a_i b^i = (\mathbf{s}^2)^{\frac{1}{2}} = \text{constant}. \tag{5}$$

For this to be consistent, $d(a_i b^i)/ds = 0$. From $\dot{s}_{ij}a^j + s_{ij}\dot{a}^j \equiv d(b_j a^j a_i)/ds$, and equation (3), one gets

$$a_j b^j e_i + s_{ij}e^j = a_i d(b_j a^j)/ds, \tag{6}$$

where $e_i \equiv \dot{a}_i - iCa^j f_{ji}$. Equation (6) is equivalent to

$$2b_i(e_1 a_2 - e_2 a_1) = a_i d(a_j b^j)/ds.$$

Since a_i, b_i are nonvanishing, $d(a_i b^i)/ds = 0$ if and only if $e_i = ua_i$, where u is an arbitrary scalar parameter. Hence

$$\dot{a}_i - iCa^j f_{ji} - ua_i = 0, \tag{7}$$

with u an arbitrary scalar. The corresponding equation for b_i is

$$\dot{b}_i - iCb^j f_{ji} + ub_i = 0. \tag{8}$$

Thus equations (7) and (8) together are equivalent to equation (3).

Consider now the rotational equation of motion of a symmetrical top

$$\dot{\mathbf{n}} \equiv \dot{\mathbf{s}} + 2K[\mathbf{s} \times \dot{\mathbf{s}}] = 2C[\mathbf{s} \times \mathbf{f}]. \tag{9}$$

In terms of spinors, equation (9) becomes

$$\dot{s}_{ij} - iK(s_{ik}\dot{s}^k{}_j + s_{jk}\dot{s}^k{}_i) = -iC(s_{ik}f^k{}_j + s_{jk}f^k{}_i). \tag{10}$$

As before, equation (10) leads to the equation

$$(a_j b^j)f_i + s_{ij}f^j = a_i d(b_j a^j)/ds,$$

or to the equivalent form

$$2b_i(f_1 a_2 - f_2 a_1) = a_i d(a_j b^j)/ds,$$

where $f_i \equiv \dot{a}_i + iKa^j\dot{s}_{ji} - iCa^j f_{ji}$. Thus equation (10) is equivalent to the equations

$$\dot{a}_i + iKa^j\dot{s}_{ji} - iCa^j f_{ji} - ua_i = 0, \tag{11}$$

$$\dot{b}_i + iKb^j\dot{s}_{ji} - iCb^j f_{ji} + ub_i = 0, \tag{12}$$

where u is an arbitrary scalar parameter.

HAMILTONIAN DYNAMICS OF THE PURE GYROSCOPE

Consider the Lagrangian

$$L \equiv -2i\dot{a}_i b^i - C(sf) + 2iu(a_i b^i - (\mathbf{s}^2)^{\frac{1}{2}}). \tag{13}$$

Equations (7) and (5) are obtained by taking a_i and u respectively as Lagrangian coordinates. The momenta corresponding to the coordinates a_i, defined by $c^i = \partial L/\partial\dot{a}_i$, are $c^i = -2ib^i$. Since the momentum conjugate to u is zero,

equation (5) is treated as a supplementary equation and u is not counted as a coordinate. Hence the P.B. relations for a_i, b_i are

$$[a_i, b_j] = \tfrac{1}{2}i\epsilon_{ij}, \quad [a_i, a_j] = 0, \quad [b_i, b_j] = 0, \tag{14}$$

so that

$$[s_{ij}, s_{kl}] = \tfrac{1}{2}i(\epsilon_{ik}s_{jl} + \epsilon_{jk}s_{il} + \epsilon_{il}s_{jk} + \epsilon_{jl}s_{ik}). \tag{15}$$

It may be noted that the equations of motion and the canonical variables can be obtained by using standard methods from a variational principle based on the Lagrangian (13).

The Hamiltonian of the system is given by

$$H \equiv c^i\dot{a}_i - L = C(sf) - 2iu(a_ib^i - (\mathbf{s}^2)^{\frac{1}{2}}).$$

Since the only weak equation involving coordinates and momenta is the one corresponding to (5), the Hamiltonian of the system is

$$H \equiv C(sf) - 2iu(a_ib^i - (\mathbf{s}^2)^{\frac{1}{2}}). \tag{16}$$

With this H, the equations of motion (3), (7), and (8) can be obtained from $\dot{g} = [g, H]$ by taking g to be equal to s_{ij}, a_i, and b_i respectively. Also, $a_ib^i - (\mathbf{s}^2)^{\frac{1}{2}}$ has zero P.B. with H, as should be the case for the consistency of the weak equation (5).

The P.B.'s (15) are the spinor equivalent of the P.B.'s for the total spin angular momentum tensor $S_{\mu\nu}$ used in papers (2,3) for the pure gyroscope. Relations of the type (14) and (15) have been postulated by Wessel (5) in another context.

HAMILTONIAN DYNAMICS OF THE SYMMETRICAL TOP

The Lagrangian

$$L \equiv -i(\dot{a}_ib^i + \dot{b}_ia^i) - \tfrac{1}{2}K\dot{s}^2 - C(sf) + 2iu(a_ib^i - (\mathbf{s}^2)^{\frac{1}{2}}) \tag{17}$$

gives the equations of motion (11), (12), and (5) on taking a_i, b_i, and u respectively as coordinates. For instance, since

$$\partial\dot{s}_{ij}/\partial\dot{a}_k \equiv \delta^k_ib_j + \delta^k_jb_i, \quad \partial\dot{s}_{ij}/\partial a_k \equiv \delta^k_i\dot{b}_j + \delta^k_j\dot{b}_i,$$

where the δ's are Kronecker symbols, the Lagrange equation $\dot{c}^i - \partial L/\partial a_i = 0$ with $c^i = \partial L/\partial\dot{a}_i$ gives

$$\frac{d}{ds}(-ib^i - 2K\dot{s}^{ij}b_j) - (i\dot{b}^i - 2K\dot{s}^{ij}\dot{b}_j - 2Cf^{ij}b_j + 2iub^i) = 0,$$

which is equation (11). The momenta c^i, d^i conjugate to a_i, b_i respectively are

$$c_i = -ib_i + 2K\dot{s}_{ij}b^j, \quad d_i = -ia_i + 2K\dot{s}_{ij}a^j. \tag{18}$$

Since the momentum conjugate to u is zero, it is best not to count u as a coordinate and to treat the equation $\partial L/\partial u = 0$, which gives (5), as a supplementary equation.

It follows from (18) that

$$2K(s\dot{s}) \equiv -2Kd(a_i b^i)^2/ds = c_i a^i + d_i b^i, \tag{19}$$

$$c_i a^i - d_i b^i - 2ia_i b^i = 0. \tag{20}$$

In the terminology of Dirac (1), equation (20) is a weak ϕ equation, the supplementary equation (5) is treated as a weak χ equation, for which to be consistent (19) gives the further weak χ equation

$$c_i a^i + d_i b^i = 0. \tag{21}$$

The spinor n_{ij} corresponding to the total spin angular momentum is

$$n_{ij} \equiv s_{ij} - iK(s_{ik}\dot{s}^k_{\cdot j} + s_{jk}\dot{s}^k_{\cdot i}). \tag{22}$$

Hence

$$\dot{s}_{ij} \equiv \frac{i}{2Ks^2}(n_{ik}s^k_{\cdot j} + n_{jk}s^k_{\cdot i}) + \frac{(s\dot{s})}{s^2}s_{ij}. \tag{23}$$

From (18)

$$n_{ij} = \tfrac{1}{2}i(c_i a_j + c_j a_i + d_i b_j + d_j b_i), \tag{24}$$

$$\dot{s}_{ij} = (c_i a_j + c_j a_i - d_i b_j - d_j b_i)/4Ka_i b^i. \tag{25}$$

Since

$$\dot{s}_{ij}b^j \equiv 2a_i(\dot{b}_j b^j) + b_i d(a_j b^j)/ds,$$

and similar relations, n_{ij} and $\dot{s}_{ij}$ can be written in the form

$$n_{ij} = s_{ij} + i(c_k b^k a_i a_j - d_k a^k b_i b_j)/a_i b^i, \tag{26}$$

$$\dot{s}_{ij} = \frac{1}{2K(a_i b^i)^2}(c_k b^k a_i a_j + d_k a^k b_i b_j) - \frac{(c_k a^k + d_k b^k)}{4K(a_i b^i)^2}s_{ij}, \tag{27}$$

where (19) has been used in (27). From (25) and the definition (22) for n_{ij}, one gets an expression for n_{ij} which consists of $s_{ij}(c_k a^k - d_k b^k - 2i\, a_k b^k)/2a_i b^i$ plus half the sum of the right-hand sides of (24) and (26). $\dot{s}_{ij}$ obtained by using (24) and (23) consists of half the sum of the right-hand sides of (25) and (27). The expressions (26) and (27) for n_{ij} and $\dot{s}_{ij}$ are completely consistent with the definitions (22) and (23). The expressions for the dynamical variables in terms of coordinates and momenta are not unique because of the occurrence of weak ϕ and χ equations.

The Hamiltonian of the system is given by

$$H \equiv -\tfrac{1}{2}K\dot{s}^2 + C(sf) - 2iu(a_i b^i - (\mathbf{s}^2)^{\frac{1}{2}}) + v(c_i a^i - d_i b^i - 2ia_i b^i) \tag{28}$$

with suitable coefficient v to be determined below. If an extra term of the form $w(c_i a^i + d_i b^i)$ is added to the right-hand side of (28), the consistency of the weak equations (5) and (20) demands that w be zero. The basic P.B.'s of the system are

$$\begin{cases} [a_i, c_j] = \epsilon_{ij},\ [a_i, a_j] = 0,\ [c_i, c_j] = 0, \\ [b_i, d_j] = \epsilon_{ij},\ [b_i, b_j] = 0,\ [d_i, d_j] = 0. \end{cases} \tag{29}$$

On the basis of (29), any one of the expressions (25) or (27) for $\dot{s}_{jk}$ gives

$$[a_i, \dot{s}_{jk}] = \frac{\epsilon_{ij}a_k + \epsilon_{ik}a_j}{4Ka_lb^l}, \quad [c_i, \dot{s}_{jk}] = \frac{\epsilon_{ij}c_k + \epsilon_{ik}c_j + 4K\dot{s}_{jk}b_i}{4Ka_lb^l}. \tag{30}$$

$c_ka^k - d_kb^k$ has zero P.B. with a_ib^i, $c_ia^i + d_ib^i$, s_{ij}, or $\dot{s}_{ij}$, while

$$[s_{ij}, c_ka^k + d_kb^k] = -2s_{ij}, \quad [\dot{s}_{ij}, c_ka^k + d_kb^k] = 2\dot{s}_{ij},$$

$$[a_ib^i, c_ka^k + d_kb^k] = -2a_ib^i.$$

With the help of these results, it is easy to check the consistency of the weak equations (5) and (20). Since

$$[c_ia^i + d_ib^i, H] = 2K\dot{s}^2 + 2C(sf) - 4\mathrm{i}(u + v)a_ib^i,$$

the weak equation (21) is consistent, provided that v in (28) is chosen to be

$$v = -u - \mathrm{i}\{K\dot{s}^2 + C(sf)\}/2a_ib^i. \tag{31}$$

From equation (4) one has

$$\dot{s}_{ij}a^j \equiv -2\dot{a}_i(a_jb^j) + 2a_i(\dot{a}_jb^j) - a_id(a_jb^j)/ds, \tag{32}$$

where $d(a_jb^j)/ds = 0$. Since from (11) and (31)

$$\dot{a}_jb^j = u(a_jb^j) + \tfrac{1}{2}\mathrm{i}(K\dot{s}^2 + C(sf)) = -v(a_jb^j),$$

it follows from (32) that

$$\dot{s}_{ij}a^j = -2(a_jb^j)(\dot{a}_i + va_i). \tag{33}$$

Similarly

$$\dot{s}_{ij}b^j = 2(a_jb^j)(\dot{b}_i - vb_i). \tag{34}$$

The application of the usual Hamiltonian equation of motion in P.B. notation gives, with the help of the analogue of (30) for b_i,

$$\dot{b}_i = [b_i, H] = vb_i + \dot{s}_{ij}b^j/2a_ib^i,$$

which is correct in view of (34). The similar equation for a_i agrees with (33). Moreover,

$$\begin{aligned} \dot{c}_i = [c_i, H] &= 2Cf_{ij}b^j + 2iub_i - 2iv(c_i - b_i) - (\dot{s}_{ij}c^j + 2K\dot{s}^2b_i)/2a_ib^i \\ &= 2Cf_{ij}b^j + 2iub_i + 2K\dot{s}_{ij}\dot{b}^j + \mathrm{i}\dot{b}_i, \end{aligned}$$

where the last equation is used in the reduction. This equation is just the correct equation of motion (11).

With the help of the basic P.B.'s (34), one obtains either with (24) or with (26)

$$\begin{cases} [s_{ij}, s_{kl}] = 0, \\ [n_{ij}, s_{kl}] = \tfrac{1}{2}\mathrm{i}(\epsilon_{ik}s_{jl} + \epsilon_{jk}s_{il} + \epsilon_{il}s_{jk} + \epsilon_{jl}s_{ik}), \\ [n_{ij}, n_{kl}] = \tfrac{1}{2}\mathrm{i}(\epsilon_{ik}n_{jl} + \epsilon_{jk}n_{il} + \epsilon_{il}n_{jk} + \epsilon_{jl}n_{ik}), \end{cases} \tag{35}$$

which are equivalent to the P.B.'s used for $S_{\mu\nu}$ and $N_{\mu\nu}$ in paper (3). The P.B.'s involving $\dot{s}_{kl}$ are

$$(36)\qquad \begin{cases} [s_{ij}, \dot{s}_{kl}] = -(\epsilon_{ik}\epsilon_{jl} + \epsilon_{jk}\epsilon_{il})/2K, \\ [\dot{s}_{ij}, \dot{s}_{kl}] = \mathrm{i}(\epsilon_{ik}s_{jl} + \epsilon_{jk}s_{il} + \epsilon_{il}s_{jk} + \epsilon_{jl}s_{ik})/4K^2s^2, \end{cases}$$

irrespective of the use of expressions (25) or (27). But (24) and (25), or (24) and (27) lead to

$$(37)\qquad [n_{ij}, \dot{s}_{kl}] = \tfrac{1}{2}\mathrm{i}(\epsilon_{ik}\dot{s}_{jl} + \epsilon_{jk}\dot{s}_{il} + \epsilon_{il}\dot{s}_{jk} + \epsilon_{jl}\dot{s}_{ik}),$$

while (36) and (22), or (26) and (27), or (26) and (25) lead to

$$(38)\qquad [n_{ij}, \dot{s}_{kl}] = \tfrac{1}{2}\mathrm{i}(\epsilon_{ik}\dot{s}_{jl} + \epsilon_{jk}\dot{s}_{il} + \epsilon_{il}\dot{s}_{jk} + \epsilon_{jl}\dot{s}_{ik}) - s_{ij}s_{kl}/Ks^2.$$

This is in keeping with the remarks below equation (27). The P.B.'s (36) and (38) are different from the corresponding P.B.'s for $\dot{S}_{\mu\nu}$ used in paper (3).

Consider the set of functions $\theta_1 \equiv a_ib^i - (\mathbf{s}^2)^{\frac{1}{2}}$, $\theta_2 \equiv c_ia^i + d_ib^i$. Then, since $[\theta_1, \theta_2] \equiv -2(a_ib^i)$, the determinant

$$\Delta \equiv \begin{vmatrix} 0 & [\theta_1, \theta_2] \\ [\theta_2, \theta_1] & 0 \end{vmatrix} \equiv 4(a_ib^i)^2.$$

If c_{12} and c_{21} denote respectively the cofactors of $[\theta_1, \theta_2]$ and $[\theta_2, \theta_1]$ divided by Δ, then $c_{12} \equiv -c_{21} \equiv -(2a_ib^i)^{-1}$. As in Dirac (1), define a new P.B. $[\xi, \eta]^*$ for any two quantities ξ and η by the formula

$$(39)\qquad [\xi, \eta]^* \equiv [\xi, \eta] - (2a_ib^i)^{-1}([\xi, \theta_1][\theta_2, \eta] - [\xi, \theta_2][\theta_1, \eta]).$$

These P.B.'s make $[\xi, \theta_1] \equiv 0$, $[\xi, \theta_2] \equiv 0$ for any ξ. If one uses the new starred P.B.'s, one can assume that θ_1 and θ_2 vanish strongly, and these strong equations can be used to simplify the Hamiltonian.

The new basic P.B.'s are, with the help of (29) and (39),

$$(40)\qquad \begin{cases} [a_i, c_j]^* = \epsilon_{ij} - a_ib_j/2a_lb^l,\ [a_i, a_j]^* = 0,\ [c_i, c_j]^* = \epsilon_{ij}c_kb^k/2a_lb^l, \\ [b_i, d_j]^* = \epsilon_{ij} + b_ia_j/2a_lb^l,\ [b_i, b_j]^* = 0,\ [d_i, d_j]^* = -\epsilon_{ij}d_ka^k/2a_lb^l, \\ [a_i, b_j]^* = 0,\ [a_i, d_j]^* = a_ia_j/2a_lb^l, \\ [b_i, c_j]^* = -b_ib_j/2a_lb^l,\ [c_i, d_j]^* = -(c_ia_j + d_jb_i)/2a_lb^l. \end{cases}$$

Since $[\theta_1, H] = 0$, $[\theta_2, H] = 0$, the equations of motion follow from $[g, H]^* = [g, H] = \dot{g}$ for g any function of the coordinates and momenta. This can be verified directly using (40). Since in the new scheme $\theta_1 \equiv 0$, $\theta_2 \equiv 0$, the simplified Hamiltonian to be used in conjunction with the P.B.'s (40) becomes

$$H \equiv -\tfrac{1}{2}K\dot{s}^2 + C(sf) + 2vc_ia^i$$

with v given by (31).

The starred P.B.'s for the variables n_{ij} and s_{ij} are again the same as (35). The P.B.'s involving $\dot{s}_{kl}$, irrespective of the expressions used for the variables, are

$$(41)\qquad \begin{cases} [s_{ij}, \dot{s}_{kl}]^* = \{ -(\epsilon_{ik}\epsilon_{jl} + \epsilon_{jk}\epsilon_{il}) + 2s_{ij}s_{kl}/s^2\}/2K, \\ [\dot{s}_{ij}, \dot{s}_{kl}]^* = \mathrm{i}(\epsilon_{ik}n_{jl} + \epsilon_{jk}n_{il} + \epsilon_{il}n_{jk} + \epsilon_{jl}n_{ik})/4K^2s^2, \\ [n_{ij}, \dot{s}_{kl}]^* = \tfrac{1}{2}\mathrm{i}(\epsilon_{ik}\dot{s}_{jl} + \epsilon_{jk}\dot{s}_{il} + \epsilon_{il}\dot{s}_{jk} + \epsilon_{jl}\dot{s}_{ik}). \end{cases}$$

The equations $\theta_1 \equiv 0$, $\theta_2 \equiv 0$ are equivalent to $\mathbf{s}^2 \equiv$ constant, $(\mathbf{s}, \dot{\mathbf{s}}) \equiv 0$. The action principle in paper (3) is subject to these strong equations because of the representation used for $\mathbf{s}$ and $\dot{\mathbf{s}}$. The agreement of the P.B.'s (41) with those of paper (3) is as expected.

In paper (3) the P.B.'s involving the components of $\dot{\mathbf{s}}$ have been deduced by postulating the fundamental P.B.'s

$$(42)\qquad [s_p, s_q] = 0, \quad [n_p, s_q] = \epsilon_{pqr}s_r, \quad [n_p, n_q] = \epsilon_{pqr}n_r,$$

(equivalent to (35) above), and then using the connection $\mathbf{n} \equiv \mathbf{s} + 2K[\mathbf{s}\times\dot{\mathbf{s}}]$ (equivalent of (22) above). In (42) p, q, r take values 1, 2, 3 and ϵ_{pqr} is the permutation symbol antisymmetric in all indices with $\epsilon_{123} \equiv 1$. Since $(\mathbf{s}, \dot{\mathbf{s}})$ need not be strongly zero

$$(43)\qquad \dot{\mathbf{s}} \equiv \frac{[\mathbf{n}\times\mathbf{s}]}{2K\mathbf{s}^2} + \frac{(\mathbf{s}, \dot{\mathbf{s}})\mathbf{s}}{\mathbf{s}^2}$$

(equivalent of (23)). From (42) and (43) the P.B.'s $[s_p, \dot{s}_q]$ and $[n_p, \dot{s}_q]$ are obtained by solving the equations

$$2K\mathbf{s}^2[s_p, \dot{s}_q] - 2Ks_qs_r[s_p, \dot{s}_r] = \mathbf{s}^2\delta_{pq} - s_ps_q,$$

$$\mathbf{s}^2[n_p, \dot{s}_q] - s_qs_r[n_p, \dot{s}_r] = \epsilon_{pqr}\dot{s}_r + \epsilon_{prt}s_q\dot{s}_rs_t.$$

Hence

$$(44)\qquad [s_p, \dot{s}_q] = (\delta_{pq} + \lambda s_ps_q/\mathbf{s}^2)/2K,$$

$$(45)\qquad [n_p, \dot{s}_q] = \epsilon_{pqr}\dot{s}_r + \mu s_ps_q/\mathbf{s}^2,$$

where λ and μ are arbitrary parameters. With the help of (45), $[\dot{s}_p, \dot{s}_q]$ is obtained by the solution of

$$4K^2\mathbf{s}^2[\dot{s}_p, \dot{s}_q] - 4K^2s_ps_r[\dot{s}_r, \dot{s}_q] = -\epsilon_{pqr}s_r - 2\lambda Ks_q(\dot{s}_p - s_p(\mathbf{s}, \dot{\mathbf{s}})/\mathbf{s}^2).$$

Hence

$$(46)\qquad [\dot{s}_p, \dot{s}_q] = -\{\epsilon_{pqr}s_r - 2\lambda K(s_p\dot{s}_q - s_q\dot{s}_p)\}/4K^2\mathbf{s}^2,$$

where λ is the same parameter as in (44). Note that (44) and (46) give

$$(47)\qquad [n_p, \dot{s}_q] = \epsilon_{pqr}\dot{s}_r + (\lambda + 1)s_ps_q/\mathbf{s}^2.$$

The P.B.'s (36) and (38) correspond to (44), (45), and (47) with $\lambda = 0$, while (37) corresponds to (45) with $\mu = 0$. The P.B.'s (41) correspond to the P.B.'s (44), (46), and (47) with $\lambda = -1$.

The Hamiltonian $H' \equiv K\dot{\mathbf{s}}^2 - 2C(\mathbf{s}, \mathbf{f})$ and the P.B.'s (44) to (47) give correctly the rotational equation of motion (9). Also $[\mathbf{s}^2, H'] = 0$. But

$$[(\mathbf{s}, \dot{\mathbf{s}}), H'] = (\lambda + 1)\{K\dot{\mathbf{s}}^2 + C(\mathbf{s}, \mathbf{f})\}/K.$$

Thus for $(\mathbf{s}, \dot{\mathbf{s}}) = 0$ to be consistent, $\lambda = -1$. This value of λ gives the P.B.'s (41) in agreement with the results of paper (3).

The P.B.'s (36) take the tensor form

$$[S_{\alpha\beta}, \dot{S}_{\mu\nu}] = (g_{\alpha\mu}\, g_{\beta\nu} - g_{\beta\mu}\, g_{\alpha\nu})/K,$$

$$[\dot{S}_{\alpha\beta}, \dot{S}_{\mu\nu}] = (g_{\alpha\mu}\tilde{S}_{\beta\nu} - g_{\beta\mu}\tilde{S}_{\alpha\nu} - g_{\alpha\nu}\tilde{S}_{\beta\mu} + g_{\beta\nu}\tilde{S}_{\alpha\mu})/K^2,$$

where

$$\tilde{S}_{\mu\nu} \equiv 2\{S^2 S_{\mu\nu} + (SS^*)S^*_{\mu\nu}\}/\{(S^2)^2 + (S\dot{S}^*)^2\}.$$

The tensor equivalents of the P.B.'s (41) are

$$[S_{\alpha\beta}, \dot{S}_{\mu\nu}] = (g_{\alpha\mu}\, g_{\beta\nu} - g_{\beta\mu}\, g_{\alpha\nu} - 2S_{\alpha\beta}\tilde{S}_{\mu\nu})/K,$$

$$[\dot{S}_{\alpha\beta}, \dot{S}_{\mu\nu}] = (g_{\alpha\mu}\tilde{N}_{\beta\nu} - g_{\beta\mu}\tilde{N}_{\alpha\nu} - g_{\alpha\nu}\tilde{N}_{\beta\mu} + g_{\beta\nu}\tilde{N}_{\alpha\mu})/K^2,$$

where $\tilde{S}_{\mu\nu}$ is as above and

$$\tilde{N}_{\mu\nu} \equiv 2\{S^2 N_{\mu\nu} + (SS^*)N^*_{\mu\nu}\}/\{(S^2)^2 + (SS^*)^2\}.$$

I am grateful to Miss Lorraine Ourom for substantial help with this paper. My thanks are due to Dr. G. Herzberg, Director of the Division of Physics, for kind encouragement and research facilities, and to the National Research Council of Canada for financial support.

REFERENCES

1. Dirac, P. A. M. Can. J. Math. 2: 129. 1950.
2. Shanmugadhasan, S. Proc. Cambridge Phil. Soc. 43: 106. 1947.
3. Shanmugadhasan, S. Can. J. Phys. 29: 593. 1951.
4. Taub, A. H. Ann. Math. (Ser. 2), 40: 937. 1939.
5. Wessel, W. Z. Naturforsch. 1: 622. 1946.

BALLONS DE MATIÈRE PLASTIQUE FABRIQUÉS PAR UN NOUVEAU PROCÉDÉ[1]

PAR PIERRE DEMERS ET JEAN-LOUIS DE GRANDPRÉ[2]

SOMMAIRE

Nous décrivons un nouveau procédé de soudure des matières thermoplastiques, spécialement adapté à la fabrication des ballons à partir des feuilles minces de Polythène. Ce procédé continu et multiple emploie un fil rougi électriquement, logé dans un appareil ou "navire" sans parties mobiles. Il a permis de faire 60 soudures à la fois, et de réaliser des ballons de 6 et de 18 mètres de diamètre. Les procédés de lancement de ces ballons ont été simplifiés. La forme optimum du ballon dans des conditions assurant l'utilisation intégrale du matériel possède un contour hexagonal s'inscrivant autour d'un cercle. Nous présentons une collection de formules relatives à ces ballons, et une étude sur les tensions et sur la résistance de l'enveloppe qui conduit à envisager la possibilité de réaliser des ballons ouverts de faible poids capables de plafonner à des pressions résiduelles inférieures à 0.001 atmosphère, à condition d'employer des feuilles épaisses de quelques microns d'une matière très solide comme le nylon.

1. INTRODUCTION

Les études sur la météorologie et sur les rayons cosmiques à haute altitude se sont faites depuis quelques années, surtout à l'aide de ballons de caoutchouc naturel ou artificiel fermés, qui se dilatent à mesure qu'ils montent, jusqu'au point où ils crèvent, tels que ceux de la Cie Dewey and Almy à Cambridge, Massachusetts. Cependant depuis 1948, la Cie General Mills à Minneapolis, Minnesota, avec l'aide du projet Helios, a mis au point des ballons ouverts de grande capacité qui, comme les sphériques populaires autrefois, montent en perdant du gaz et plafonnent sans crever, lorsque le poids de l'air déplacé égale le poids total enlevé. Ces ballons sont faits en Polythène, polymère de l'éthylène préparé à partir du gaz naturel par condensation à température et pression élevées, par la Cie Dupont aux États-Unis. Ces ballons ont permis dès leurs premières envolées, la découverte des particules primaires lourdes de la radiation cosmique, en laissant séjourner des plaques photographiques spéciales longtemps à une grande altitude, où la pression résiduelle est environ 0.01 atmosphère. Ces ballons ne sont pas disponibles en dehors des États-Unis et sont fort coûteux.

Le procédé employé à Minneapolis consiste à tailler des fuseaux dans des laizes de Polythène épaisses de 0.001 pouce et larges probablement de 3 ou 4 mètres, puis à les souder côte à côte. La soudure se fait en chauffant les deux bords à joindre, tenus ensemble superposés. Les détails manquent sur les méthodes exactes employées, sauf qu'on réalise un joint plat, probablement à l'aide d'un fer chaud (3, 5).

Heitler et King (4) à Bristol, ont décrit en 1950 la fabrication de tels ballons, par un procédé de soudure au fer chaud. Ils ont réalisé une sorte de petit chariot qui avance par un tapis sans fin formé d'une lame de cuivre mince, qui sert en somme comme la chenille d'une auto-chenille, sur les bords à joindre. Ce tapis

[1] *Manuscrit reçu le 9 novembre, 1951. Contribution de l'Institut de Physique, Université de Montréal, Montréal, Que.*

[2] *Collaborateur pour les parties 2, 4, et 5.*

est chauffé et soude les feuilles à mesure qu'il avance. Ils employent une feuille simple épaisse de 0.002 pouce, large de 40 pouces. Ils ont fait des ballons hauts de 50 et 100 pieds, et se proposent des ballons de 200 et peut-être de 400 pieds.

2. PREMIER PROCÉDÉ, SOUDURE À LA FLAMME

Nous avons fabriqué en 1950 deux ballons, à six et à huit fuseaux respectivement. Les fuseaux ont d'abord été taillés dans des feuilles de Polythène CIL, épaisses de 0.0015 pouce environ, selon un patron destiné à donner au sommet la forme d'une sphère, raccordée à un cône tel que la hauteur soit moitié plus grande que le diamètre. Cette forme reproduit celle des ballons 733 de General Mills. Les fuseaux nécessaires ont un contour sinusoidal au sommet et triangulaire à la base. Près du sommet, la largeur est donc proportionnelle à $\sin \pi$ (distance du sommet/d), la valeur de d étant voisine de la longueur du fuseau.

Les feuilles étaient en réalité doubles, on les produit en effet sous la forme de tubes, qu'on aplatit ensuite avant de les enrouler. De la sorte, il est facile de tailler à la fois les deux bords d'un fuseau. On les a d'ailleurs taillés tous ensemble, les tubes nécessaires étant superposés. Puis on les a soudés à la flamme, suivant en cela la suggestion de M. Mackenzie de la Compagnie CIL. Les deux bords à souder sont placés ensemble à plat entre deux règles de métal, en laissant déborder une marge de 4 à 5 mm. En promenant une flamme longue de 3 cm. environ, on chauffe les deux bords, qui fondent, reculent jusqu'à la règle et se soudent en un bourrelet. Le Polythène en effet se ramollit et fond aux environs de 120°C. Ce procédé est excellent mais laborieux. Il réclame une personne habile et une attention constante pour placer les bords sous les règles et pour promener la flamme. La flamme peut être remplacée par un fil chauffé électriquement. Les procédés de soudure du Polythène sont discutés par Ryan (6).

3. SECOND PROCÉDÉ, NAVIRE ET FIL CHAUD

Après divers tâtonnements, nous avons finalement mis au point un procédé de soudure continu et multiple, spécialement adapté à la fabrication des ballons, qu'il permet d'accélérer considérablement. Il est fondé sur un principe apparemment nouveau dans le domaine de la soudure des matières plastiques. Les feuilles sont tirées à travers un appareil sans parties mobiles, et les fuseaux en sortent taillés et soudés l'un à l'autre formant si on les déploie, un ballon entièrement fini sauf une soudure allant d'une extrémité à l'autre, et une petite région près de chaque extrémité.

L'élément qui taille et qui soude est un fil rougi électriquement, passant dans des trous percés dans deux plaques de cuivre légèrement espacées qui doivent rester froides au cours du fonctionnement. Deux feuilles qu'on tire ensemble entre les deux plaques à la rencontre du fil sont échancrées en arrivant vis à vis des trous, par la chaleur, qui les soude en un bourrelet de part et d'autre du fil. Le fil agit comme une flamme, les feuilles fondent et reculent jusqu'au bords des trous. Le bourrelet ne colle pas au métal refroidi, il glisse sur lui au contraire et on le tire normalement avec la feuille sans qu'il s'accroche, à mesure qu'il se forme.

L'appareil complet présente 50 tels éléments ou étages, compris entre 51

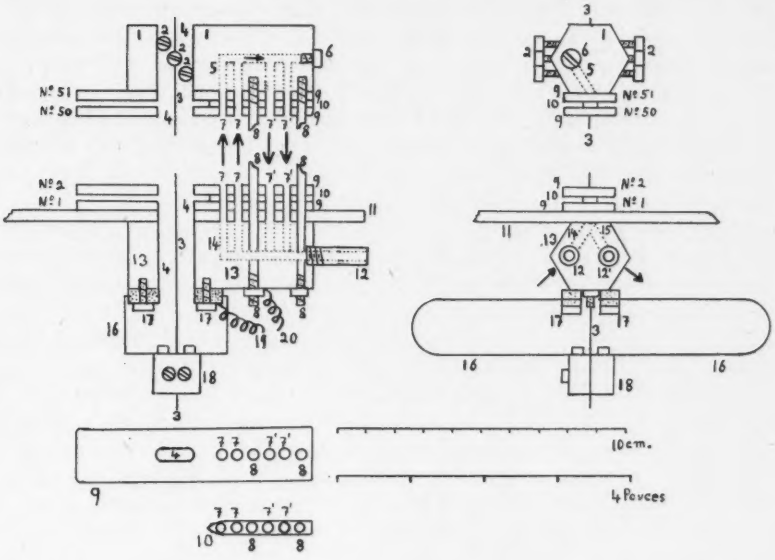

FIG. 1. Navire pour la soudure multiple et continue du Polythène et d'autres matières thermoplastiques, ayant servi à la confection de ballons de 10 et de 30 fuseaux.

1. Bloc supérieur en laiton hexagonal.
2. Vis tenant les fils chauffants.
3. Il peut y avoir d'un à trois fils chauffants.
4. Trous laissant passer les fils 3.
5. Trous percés dans le bloc 1 pour la circulation de l'eau de refroidissement, reliés à 7 et à 7′.
6. Vis fermant l'un des trous 5.
7, 7′. Canaux formés par l'alignement des trous dans les lames, les lamelles, et les blocs de laiton pour le refroidissement. La circulation de l'eau est marquée par des flèches.
8. Tiges en laiton filetées aux extrémités, et trous les recevant. Ces tiges serrent ensemble les blocs de laiton, les lamelles, et les lames. L'échanchéité est assurée en faisant circuler du glyptal rouge une fois l'appareil assemblé, puis en égouttant et en laissant sécher avant de faire passer l'eau.
9. Lames en cuivre rouge épaisses de 1/16 pouce ou 1.59 mm. Il y a 51 lames numérotées de bas en haut, seulement quatre lames sont répresentées sur 51, et deux lamelles sur 50.
10. Lamelles en cuivre rouge épaisse de 1/32 pouce ou 0.794 mm.
11. Petite table en aluminium également percée des trous 4, 7, 7′ et 8, 12, 12′. Tubes vissés pour l'entrée et la sortie de l'eau dans le bloc inférieur en laiton hexagonal 13.
14. Trous pour l'entrée de l'eau, reliés à 12 et à 7.
15. Trous pour la sortie de l'eau, reliés à 12′ et à 7′.
16. Ressort, en tôle galvanisée, gardant le fil chauffant tendu malgré ses dilatations.
17. Vis fixant le ressort 16 et isolement.
18. Blocs de laiton serrant l'extrémité inférieure du fil 3.
19, 20. Fils amenant le courant d'une part au ressort, d'autre part à la masse.

Figure sensiblement à l'échelle, sauf que l'épaisseur des lames et lamelles est exagérée.

plaques de cuivre, traversées par le même fil chaud. Chacun de ces étages peut recevoir une paire de feuilles à couper et à souder.* Les plaques de cuivre ou *lames*, épaisses de 1/16 de pouce, sont tenues espacées par de petites plaques étroites de cuivre ou *lamelles*, placées derrière le trou du fil chauffant, épaisses de 1/32 de pouce. Les lames et les lamelles sont percées de trous servant à les aligner et à faire circuler l'eau de refroidissement; elles sont saisies entre deux blocs de laiton hexagonaux, convenablement percés aussi. L'appareil, qui est fixé à une petite table d'aluminium, est figuré dans ses détails Fig. 1.

Ce procédé n'a servi jusqu'ici qu'avec le Polythène. Cependant d'autres matières thermoplastiques, comme le nylon et la lucite, pourraient probablement être soudées à son aide. Nous ne l'avons pas essayé avec des feuilles épaisses de plus de quelques millièmes de pouce.

Le matériel venant sous la forme d'un tube aplati a suggéré l'emploi de l'appareil de la façon suivante (Fig. 2). On tire à la fois autant de tubes qu'il y aura de fuseaux. Chaque tube passe de part et d'autre d'une lame de cuivre de l'appareil. Tous les tubes par chacune de leurs parois, touchent un autre tube, sauf ceux du haut et du bas, qui n'ont chacun qu'un voisin. Les tubes sortent soudés tous l'un à l'autre, de chaque côté de l'appareil, formant comme deux soufflets d'accordéon. A cause de sa ressemblance, au cours de cette opération, avec une barque fendant une nappe liquide, l'appareil a été appelé un *navire*.

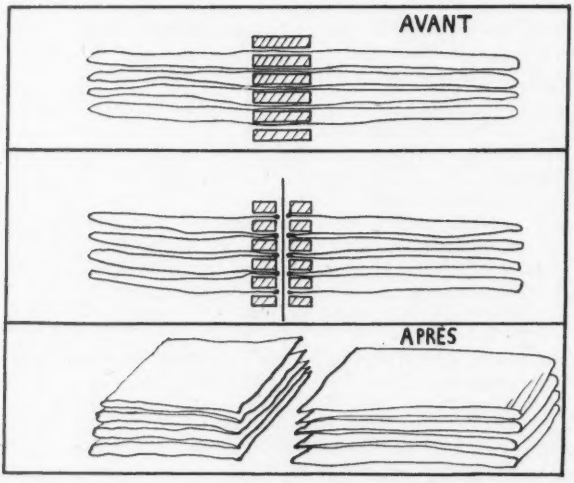

FIG. 2. Action du fil soudeur. *Avant.* Les tubes enfilés autour des lames touchent chacun par une paroi le tube voisin. Le fil chaud coupe ensuite les parois qu'il rencontre et y forme un bourrelet, s'il rencontre deux parois se touchant, il les soude en un seul bourrelet. *Après.* Au lieu de quatre tubes on a deux soufflets présentant trois soudures et deux bourrelets—en haut et en bas—non soudés.

* *On pourrait donc tirer à la fois 50 paires de feuilles qui en sortiraient taillées et soudées chacune selon deux bourrelets, faisant ainsi à la fois 100 soudures.*

Le Polythène entre donc sous la forme de n tubes distincts, il sort sous la forme de deux soufflets présentant chacun $n-1$ soudures. La longueur totale des soudures exécutées simultanément est $2(n-1)L$, L étant la longueur des tubes. Nous avons réussi à faire ainsi 29 soudures simultanées, $n = 30$, dans un temps voisin de quatre heures tous arrêts compris, sur une longueur de 64 pieds, ou une longueur totale de 3700 pieds.

La théorie de la soudure mettrait en oeuvre les principes de la conduction de la chaleur, et de la capillarité. Pour certaines conditions mal comprises, le bourrelet est dentelé, ce qui résulte de phénomènes analogues à la formation de gouttes dans un filet liquide. Avec le navire à 50 étages, servant à faire plusieurs soudures à la fois, la soudure était plus solide si on prenait un fil chauffant fin. Si on s'en servait pour faire une seule soudure à la fois, on obtenait de meilleurs résultats avec un boudin de fil résistant, plus large, introduit dans les mêmes trous. La vitesse à laquelle on fait avancer les feuilles dans le navire ne doit pas être excessive, sinon la soudure ne tient pas bien: les deux parois fondues par la chaleur sont refroidies trop tôt, et ne se collent pas en un bourrelet unique et solide. La vitesse permise est d'environ 60 cm. par min. Avec des précautions, on arrive à produire une soudure tout à fait solide et sans trous, surtout si on ne manipule qu'un petit nombre de feuilles simultanément. Cependant il faut dire qu'il n'a pas été possible d'éviter jusqu'ici absolument tous les trous et tous les accidents quand on a tiré plusieurs feuilles à la fois pour faire un ballon. La régularité du déplacement du matériel semble être une condition essentielle de succès.

4. CONFECTION D'UN BALLON

Voici la description de notre expérience de l'usage du navire, appliqué à réaliser des ballons de 10 et de 30 fuseaux ayant la forme optimum cylindroconique décrite plus loin, à partir de feuilles épaisses d'un peu moins de 0.001 pouce, en Polythène, livrées sous forme de tubes aplatis larges de 36 pouces.

Il faut d'abord mesurer n bandes de la longueur nécessaire L, augmentée d'une marge de 2 à 3%. Chaque bande est enroulée séparément sur une baguette de bois de 1/2 pouce de diamètre, longue de 40 pouces, en formant un *rouleau* aux bords bien réguliers. Les opérations de déroulement et de mesure requièrent des supports solides, un moteur à vitesse réglable, et un compte-tours relié à une roue caoutchoutée appuyant constamment sur le rouleau original. Les n rouleaux sont installés chacun dans une paire d'encoches se faisant face, dans un *berceau* à un ou plusieurs étages. On tire successivement les tubes et on les fait passer dans les intervalles d'une *barrière* formée de barres de laiton horizontales superposées à une petite distance l'une de l'autre.

Puis en commençant par la feuille du bas, on les enfile dans les espaces du navire, chaque feuille,—qui est un tube aplati—, entourant une ou même plusieurs lames. Le côté inférieur d'une feuille est enfilé dans l'espace où se trouve déjà le côté supérieur de la feuille précédente. Les feuilles ont ainsi été échancrées au contact du fil chaud, et chacune a été fixée à une planchette à sa sortie du navire, à l'aide de ruban Durex. Il y a finalement plusieurs planchettes super-

posées, on en ajoute à mesure qu'on tire de nouvelles feuilles, et elles sont tenues par un trou dans une tige verticale de métal.

On tire ensuite, en saisissant cette tige et les planchettes, toutes les feuilles à la fois. Le départ donne lieu parfois à des accrochages, le bourrelet ayant pu s'épaissir dans certains espaces, on s'aide alors de mouvements latéraux. Sur la feuille du dessus on a tracé d'avance le patron qu'il faut suivre avec le navire. La ligne tracée peut faire un angle, ou *angle d'attaque*, avec l'axe de la feuille. On oriente le navire en angle et en position, pendant qu'on continue de tirer l'ensemble des feuilles. Le navire peut tourner sur une base de bois, celle-ci peut coulisser latéralement sur la table.

La principale cause d'accident est qu'une feuille plastique, par un de ses côtés, s'embarrasse dans le bord d'une lame et n'avance plus. Dès lors, la tension augmente, la feuille peut se déchirer sur sa largeur, parfois elle saute dans un espace voisin: une soudure alors ne se fait pas, et une soudure triple peut alors apparaître. Il faut surveiller constamment les soudures à la sortie du navire, et si un défaut apparaît, souvent on peut y remédier avec une spatule plate et des ciseaux. Parfois il faut tout désenfiler et renfiler dans le navire.

La traction initiale se fait à la main. On peut ensuite s'aider d'une corde passant sur un *treuil* mu par un moteur à vitesse réglable, qui régularise le mouvement. Il faut de temps à autre changer le point d'accrochage de la corde sur le matériel. On saisit celui-ci sur toute sa largeur entre deux règles serrées fortement, car le Polythène glisse facilement, et il importe que toutes les feuilles avancent également. Les paires de soufflets obtenus sont entassées sur la table sous la corde. L'opération s'est faite sur deux tables de 4 m. $\times$ 1.2 m. A aucun moment on n'a besoin d'étaler les fuseaux sur toute leur longueur. Voir Fig. 3.

Un angle d'attaque élevé rend l'opération plus délicate, le navire pouvant s'accrocher plus facilement. L'expérience nous a appris que pour éviter les accrochages il faudrait tirer exactement dans la direction des soudures. Il ne serait

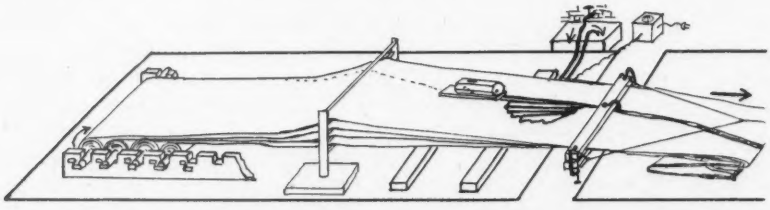

FIG. 3. Fabrication d'un ballon. A gauche le berceau avec des ressorts maintenant alignés les rouleaux. Il porte ici quatre rouleaux, se dévidant indépendamment, chaque tube traverse un intervalle de la barrière, est divisé et soudé au passage dans le navire selon la coupe de la Fig. 2. Le navire peut coulisser sur des glissières, et pivoter autour d'un axe vertical, pour permettre de suivre le patron tracé en pointillé. Le navire est alimenté par une circulation d'eau, et par un transformateur réglable, de préférence à secondaire entièrement isolé du primaire pour éviter les courts-circuits avec le sol. Les soufflets sont saisis entre deux règles de bois serrées par trois pinces réglables, et tirés par une corde solide, et par un moteur non figuré. N.B., les échelles ne sont pas respectées, en particulier, le berceau devrait être plus petit.

d'ailleurs pas plus difficile de suivre un contour courbe qu'un contour linéaire. Dans les parties où l'angle d'attaque est nul, le navire longe un côté ou l'autre de la feuille, et on perd nécessairement une petite *marge* de matière, puisque la lame de cuivre ne peut pas traverser le bord du tube. La perte, si les rouleaux sont réguliers et bien alignés dans leur berceau, est facilement réduite au minimum, soit à environ 1 cm. sur la largeur du tube aplati ou 1% en valeur relative sur le diamètre final du ballon.

Ainsi nous avons fait un ballon de $n = 30$ fuseaux, avec $L = 64$ pieds, en attaquant au milieu de la largeur à un bout, et en terminant au milieu aussi à l'autre bout. Nous avons préparé trois fois six ballons de $n = 10$ fuseaux, $L = 21$ pieds, en attaquant des bandes de $6 \times 21 = 126$ pieds, à un bord, et en finissant au même bord à l'autre extrémité. Voir Fig. 4.

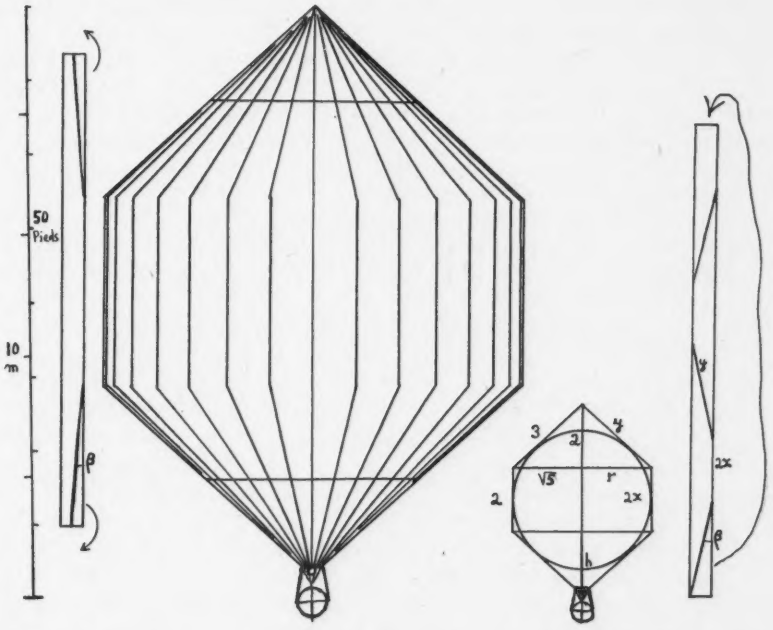

FIG. 4. Ballons de forme optimum cylindroconique, figures à l'échelle. Ballon de 30 fuseaux supposé plein, avec son appendice, avec les traces des 30 soudures sur le long et des 2 soudures périphériques. Patron, de longueur L, pour tirer un tel ballon; les deux portions triangulaires sont soudées au reste par des soudures périphériques, de longueur totale égale au périmètre à l'équateur.—Ballon de 10 fuseaux, avec son appendice, avec quelques éléments géométriques et leurs valeurs. Patron, de longueur $3L$, pour tirer trois tels ballons. La portion triangulaire est reliée, pour terminer l'un de ces ballons, à l'endroit indiqué, par une soudure périphérique de longueur égale au périmètre à l'équateur. Les deux autres ballons sont complets, une fois tirés, sauf une soudure de toute la longueur. Les flèches indiquent comment on raccorde au reste les morceaux triangulaires. β est l'angle d'attaque et vaut arc tg $2.3416/n$.

Pour finir les ballons à partir des soufflets obtenus en tirant les feuilles à travers le navire, il reste des soudures à faire isolément. Il y en a une sur toute la longueur, que le navire est incapable de faire dans la même opération en même temps que les précédentes. Il peut y en avoir une ou deux sur la circonférence, et aussi des reprises. On emploie encore le navire, à la façon d'une machine à coudre. La soudure sur toute la longueur se commence de préférence au sommet, afin que celui-ci prenne, une fois gonflé, une forme tout à fait régulière évitant les surtensions dans la paroi, toutes les soudures se rencontrent en effet au sommet.

Il faut ensuite inspecter le ballon sur toutes ses soudures et sur toute sa surface pour trouver les trous et les boucher avec du ruban Durex. Après expérience, nous avons trouvé expédient de ne pas inspecter en détail les soudures, mais imitant en cela la pratique de General Mills, de toutes les couvrir, du haut en bas, de ruban Durex, qui bouche les trous sans qu'on ait à les chercher et qui ajoute à la solidité. Pour le ballon de 10 fuseaux, il ajoute 150 gr. au poids. Le ruban type Durex d'acétate de cellulose serait peut-être préférable à cause de sa résistance à l'eau, mais nous avons employé le ruban ordinaire, de Cellophane gommé. S'il est mouillé, le Cellophane quitte la gomme, de sorte que le passage du ballon ainsi couvert, à travers un nuage, pourrait l'endommager. Nous avons aussi décidé de renforcer latéralement le ballon de 10 fuseaux en posant deux anneaux de même ruban, à 5 et à 10 pieds du sommet. Pour le ballon de 30 fuseaux, il faudrait poser de tels anneaux à tous les trois pieds 1/2 environ, à partir du sommet jusqu'un peu au dessus de la moitié de la hauteur, pour obtenir une solidité suffisante. Les distances à partir du sommet sont marquées alors de pied en pied avec du vernis rouge, ce qui facilite la manipulation ultérieure du ballon et la mesure de la bulle.

Il faut ensuite terminer la base de la façon recommandée par Moore et Smith (5). Pour cela, on forme un anneau de diamètre 2 pieds, en fil d'acier ou corde à piano de 1/32 pouce de diamètre tenu fermé par du ruban Durex. On l'introduit dans la base du ballon à l'intérieur, et on l'y colle avec le même ruban. On colle aussi un appendice tubulaire en Polythène, de diamètre 2 pieds, de hauteur 3 pieds. Le bas est tenu fermé par l'élasticité d'un anneau circulaire de diamètre $2\pi/2$ pieds, en corde à piano pareille. Ces dimensions conviennent pour $n = 10$; pour $n = 30$, l'ouverture mesurait 3 pieds de diamètre, le fil d'acier mesurait 1/16 de pouce de diamètre, l'appendice avait 5 pieds de long.

L'appendice évite l'entrée brutale de l'air, mais doit permettre la sortie facile de l'hydrogène sans causer de surpression qui pourrait créer des tensions excessives dans la paroi et la déchirer; au moment où le ballon prend forme, la vitesse de sortie du gaz est de quelques mètres par seconde.

La charge est répartie symétriquement par cinq ou six rubans Padoue de coton tissé, sur l'anneau au sommet de l'appendice, réunis et noués, dans l'appendice même, à un seul ruban plus gros.

5. GONFLEMENT ET LANCEMENT

Nous avons amélioré et simplifié les procédés décrits par General Mills, que nous avons d'abord employés tels quels. Ils consistent à enfiler un tube de gonfle-

ment en Polythène, par la base, jusqu'au sommet. Le ballon est étalé sur un tapis de lancement de toute sa longueur, pour réduire l'action du vent qui peut le soulever et le jeter dans les cailloux ou dans les herbes, on le maintient avec des sacs de sable. On le gonfle par le tube de gonflement, en introduisant par un bout une quantité de gaz calculée pour assurer la force ascensionnelle voulue, dans la bulle maintenue au sol à l'autre bout. Le contrôle du gonflement est rendu difficile par la distance, et on ne peut pas peser la bulle pour connaître directement sa force ascensionnelle. Le lancement se fait après avoir étalé tout le train à emporter sur le sol, dans le lit du vent, et en enlevant d'un coup tous les sacs de sable.

Nous avons simplifié ces procédés. Le ballon est plié régulièrement sur la largeur d'un demi ou d'un quart de fuseau, et il est ensuite roulé en commençant par l'appendice, de sorte que le sommet est à l'extérieur. On déroule juste la longueur nécessaire pour former la bulle, augmentée d'un ou deux pieds, et on étrangle la base avec une bonne corde de nylon faisant plusieurs tours. Le gonflement se fait à travers une incision longue de 5 cm., bordée de ruban Durex, ménagée à la base de la bulle. On peut tarer la bulle, et mesurer la force ascensionnelle, avec un dynamomètre accroché à la corde, qui sert en même temps à la retenir, on connaît donc sans équivoque et sans mesure préalable des volumes gazeux, la force ascensionnelle exacte au moment du départ. L'incision est ensuite fermée avec du ruban Durex. Les longueurs marquées sur la paroi facilitent les manipulations.

Le reste du ballon est déroulé et tenu à la façon d'un câble, étranglé dans les mains de plusieurs personnes, le vent est sans influence, et on se dispense du long tapis nécessaire autrement. On attache la nacelle, le train est disposé dans le lit du vent; on défait la corde qui tenait la bulle, qu'on tient à la main, et qu'on lâche au moment voulu. On a manœuvré ainsi sans difficulté la bulle du ballon de 30 fuseaux, qui tirait avec une force nette de 30 kg. à sa base. Pour des bulles plus grosses, on peut prévoir un dispositif mécanique de retenue et de lâchement à la base de la bulle. L'enveloppe a un grand périmètre à cet endroit et ne souffre pas du tout d'être serrée par la main ou par une corde. Nous n'avons pas cherché à faire de lancements par un vent de plus de 15 km. par heure.

Voici quelques données expérimentales sur la fabrication, le lancement, et les propriétés des ballons que nous venons de décrire. Ces ballons de forme optimum ou cylindroconique sont faits en Polythène CIL épais d'environ 0.00085 pouce.

Nombre de fuseaux:	10	30
Durée de fabrication:	Un jour à trois personnes.	Une semaine à six personnes.
Nombre de ballons lancés:	2	1
Longueur du ballon étalé:	10.4 m.	31.3 m.
Volume du ballon:	116 m.^{3}	3132 m.^{3}
Poids du ballon:	2.8 kg.	25 kg.
Poids du train complet avec la nacelle:	4 kg.	28 kg.
Force ascensionnelle nette:	2.4 kg.	10 kg.
Vitesse d'ascension calculée selon (5):	Environ 350 m./min.	Environ 350 m./min.

Vitesse observée au départ:	Environ 300 m./min. (Un théodolithe, mesure de l'angle sous-tendu ou stadia.)	Environ 250 m./min. (Baromètre enregistreur.)
Pression et altitude prévues pour le ballon seul à son plafond:	0.020 atm. 26.5 km.	0.00666 atm. 33.6 km.
Idem, avec le train complet:	0.029 atm. 24.2 km.	0.00747 atm. 32.9 km.

REMARQUES:

(1) La montée s'est faite dans chaque cas tout droit sans agitation latérale.

(2) Le ballon de 30 fuseaux portait un seul anneau de ruban Durex, a 8 pieds du sommet. Ce renforcement était insuffisant, la tension dans la bulle a distendu la paroi, sans la déchirer, avant le départ, et elle l'a sans doute déchirée au cours de l'ascension, car le plafond atteint n'a été que de 7 kilomètres, et l'ascension n'a duré qu'une heure et demie. Des anneaux de ruban Durex à tous les trois pieds et demi donneraient probablement une solidité suffisante.

(3) Nous avons pu suivre pendant une demi-heure environ au théodolithe les ballons de 10 fuseaux; l'altitude atteinte était alors voisine de 9 kilomètres, et l'extrapolation de la courbe d'ascension permet de croire qu'ils ont continué de monter jusqu'au plafond prévu.

6. FORME OPTIMUM DU BALLON

Le ballon doit présenter le plus grand volume possible pour une surface donnée d'un matériel choisi. Ainsi posé de façon générale, le problème conduit à adopter la forme sphérique. Les fuseaux sont taillés selon un contour sinusoïdal. Si on ne prend qu'un fuseau dans toute la longueur d'une laize, on perd beaucoup de matériel. Si, dans le tube déjà décrit, on taille les fuseaux les uns après les autres, tous tangents l'un à l'autre par leur partie sinusoïdale, on perd moins de matériel. Cependant il ne serait pas commode de prendre ainsi les fuseaux dans le procédé de soudure multiple.

Nous avons cherché la solution du problème dans les conditions suivantes: premièrement on utilisera tout le matériel mis en jeu. Deuxièmement on taillera les fuseaux selon trois lignes droites seulement. Le ballon sera alors formé d'une portion cylindrique centrale de hauteur $2x$, et terminé par deux cônes de hauteur h l'un et l'autre. Si on ne fait qu'un ballon à la fois, on devra accepter de le faire en deux ou trois parties, et il y aura une ou deux soudures à faire séparément après le passage multiple dans le navire, sur une longueur totale égalant la circonférence du cylindre, en plus de la soudure de toute la longueur. Si on en fait plusieurs à la suite, de telles soudures complémentaires ne sont nécessaires que pour un seul ballon. Voir les patrons Fig. 4.

Cherchons par le calcul des maxima quelle est alors la forme du ballon possédant pour une surface donnée S le plus grand volume V. La forme étant définie par les dimensions x, y, h, et r, on trouve qu'il doit exister entre elles la proportion $2x: y: h: r = 2: 3: 2: 5\frac{1}{2}$. Le contour est hexagonal et circonscrit un cercle de rayon r.

7. PROPRIÉTÉS AÉROSTATIQUES, IMPORTANCE DE L'ÉPAISSEUR

Voici quelques formules calculées pour la forme cylindroconique optimum.

Le nombre de fuseaux n détermine tous les éléments géométriques si on suppose un tube large de 183 cm. une fois fendu, ce qui représente la largeur maximum du

fuseau: la hauteur H du ballon ayant pris forme, la surface S, le volume V. L'épaisseur e exprimée en millièmes de pouce et la densité 0.94 déterminent le poids W. La force ascensionnelle brute en supposant le ballon plein au départ est F_0, la pression minimum accessible est P_0, le rayon ρ_1 de la bulle supposée sphérique capable d'enlever tout juste le ballon sans charge supplémentaire est B_0/π. On a supposé invariablement l'hydrogène comme gaz de gonflement, les conditions normales au départ, et la température 0°C. dans l'air extérieur et dans le ballon au cours de l'ascension. Sauf pour e, les unités sont le mètre, le kilogramme, et l'atmosphère.

$$H = 0.806\, n$$

$$S = 1.19\, n^2$$

$$V = 0.116\, n^3$$

$$W = 0.0284\, n^2 e \tag{1}$$

$$F_0 = 0.139\, n^3 \tag{2}$$

$$\pi\rho_1 = B_0 = 0.557\, n^{2/3} e^{1/3} \tag{3}$$

$$P_0 = 0.206\, e/n. \tag{4}$$

Eliminons le paramètre n entre (1) et (4):

$$W = 0.0012\, e^3/P_0^2 \tag{5}$$

$$W = 0.00147\, e^3 \text{ densité}^3/P_0^2, \tag{6}$$

la dernière relation valant pour une substance ayant une autre densité que le Polythène. Pour atteindre une altitude déterminée par une valeur de P_0, le poids nécessaire est proportionnel au cube de l'épaisseur de la feuille employée, d'autre part le nombre de fuseaux nécessaires est proportionnel à l'épaisseur d'après (4). Cette relation est importante car elle montre que si l'on veut atteindre une grande altitude avec un ballon ouvert portant une charge faible par rapport à son propre poids, le poids du ballon décroît très rapidement lorsqu'on réduit l'épaisseur de la feuille. Une réduction de 20% sur l'épaisseur diminue le poids de moitié. Un facteur deux sur l'épaisseur signifie un facteur huit sur le poids, quatre sur la surface, et deux sur la longueur.

Cette observation permet d'envisager sérieusement la possibilité de faire plafonner des ballons ouverts relativement légers et faciles à manier, avec une charge de quelques kilogrammes à des altitudes jamais encore atteintes par ce moyen, s'il est possible de se procurer des feuilles de matière plastique comme le Polythène ou peut-être le nylon, sous des épaisseurs très faibles.

Par exemple on a déjà produit des feuilles de nylon pesant 6 gr. par m.^{2} On en trouve la mention, pour un tout autre usage, dans une publication d'Allen et Dewan (1). Par rapport au Polythène de 0.001 pouce, pesant 23.87 gr. par m.^{2}, on gagnerait un facteur 63 sur le poids, et 3.98 sur le nombre de fuseaux. Le ballon capable d'atteindre le millième d'atmosphère ou environ 150,000 pieds, ne pèserait que 19 Kg., et compterait environ 50 fuseaux avec une hauteur de 45 m. Le nylon a des propriétés mécaniques qui le rendraient probablement préférable au Polythène pour cet usage, comme aussi son imperméabilité aux gaz, probablement plus grande que celle du Polythène.

Nous allons envisager successivement ces deux aspects, tensions et perméabilité de l'enveloppe.

8. TENSIONS DANS L'ENVELOPPE

Supposons une bulle possédant un axe de symétrie vertical. La pression est plus grande à l'intérieur qu'à l'extérieur, parce qu'elle diminue avec la hauteur plus rapidement dans l'air que dans l'hydrogène. Appelons ΔP cette surpression, évaluée en kg. par m.^{2}, tandis que la hauteur h au dessus de l'ouverture à la pression extérieure P est exprimée en mètres, et que P est exprimée en atmosphères, la température étant supposée 0°C.

$$\Delta P = 1.196\, hP. \tag{7}$$

Dans les cas pratiques, la surpression ne dépasse pas le millième de la pression extérieure, de sorte qu'il est inutile de recourir à une formule exponentielle valable dans le cas général.

Cette surpression tend les parois. Considérons une calotte de base circulaire de rayon ρ, située à une hauteur h de l'ouverture. La force de pression sur la base est $\pi\rho^2\Delta P$. Des tensions T_1 dans la paroi l'équilibrent. La normale à la paroi fait un angle α avec l'horizontale. Les tensions sont exprimées en kg. par m., elles exercent sur le périmètre de la base des forces qui ont pour résultante verticale $2\pi\rho T_1 \cos\alpha$; d'où:

$$T_1 = \rho\Delta P/2\cos\alpha = 1.196\, \rho_1 hP/2, \tag{8}$$

ρ_1 est le rayon de courbure dans le plan perpendiculaire au plan méridien, $\rho_1 = \rho/\cos\alpha$. La tension T_1 est comprise dans le plan tangent à la paroi et dans le plan méridien.

Cherchons maintenant les tensions transversales T_2, horizontales, normales aux précédentes et contenues dans le plan tangent à l'enveloppe (Fig. 5). Pour cela déterminons une zone, différence de deux calottes comme la précédente, dont les bases ont des hauteurs h et $h + dh$. Divisons cette zone en moitiés par un plan méridien vertical, définissant par sa rencontre avec la paroi deux côtés obliques $ds = dh/\cos\alpha$, et avec les bases circulaires, des côtés parallèles horizontaux 2ρ et $2(\rho + d\rho)$. Ces quatre côtés forment un trapèze. L'équilibre de l'une de ces demi-zones est obtenu par (i) l'action des forces de tension T_2 dues à l'autre demi-zone, sur les deux côtés obliques ds; (ii) des forces de pression sur la paroi de cette demi-zone; (iii) des forces de tension T_1 distribuées sur le bas du pourtour, et des forces de tension $T_1 + dT_1$ distribuées sur le haut du pourtour; (iv) du poids de cette portion de la paroi. Ce dernier facteur est sans influence directe, puisque le poids fait invariablement un angle droit avec T_2. L'expression de la première et de la seconde force est comme suit:

$$2T_2 ds = 2T_2 dh/\cos\alpha \tag{9}$$

$$2\rho dh\Delta P. \tag{10}$$

Evaluons maintenant (iii). La tension T_1 s'exerce au niveau h, sur un élément du pourtour ρdu, u étant l'angle compté autour de l'axe vertical. La force ré-

sultante en cet endroit est $T_1\rho du$. Si $\cos\alpha \neq 1$, cette force a une composante horizontale $T_1\rho \sin\alpha du$. La projection de cette force sur la normale au plan méridien ou au trapèze, contribue seule à la tension horizontale, elle vaut $T_1\rho \sin\alpha \sin u\, du$. Il faut intégrer ces projections élémentaires sur toutes les valeurs de u dans un demi-tour, avec le résultat suivant:

$$-T_1\rho \sin\alpha \int_0^\pi \sin u\, du = -2T_1\rho \sin\alpha.$$

Cette force est négative si elle tend à comprimer ou à faire rentrer le matériel, elle a donc le signe opposé à celui de $\sin\alpha$, l'angle α étant compté positivement si le rayon augmente avec la hauteur, i.e. si le ballon est à cet endroit évasé vers le haut, $d\rho/dh > 0$.

Recommençons le raisonnement au niveau $h + dh$, où la résultante est du signe opposé

$$2(T_1 + dT_1)(\rho + d\rho)\sin(\alpha + d\alpha)$$

ajoutons algébriquement les deux forces précédentes et introduisons les dérivées

$$2(T_1 + dT_1)(\rho + d\rho)\sin(\alpha + d\alpha) - 2T_1\rho \sin\alpha = 2[d(T_1\rho \sin\alpha)/dh]dh.$$

Explicitons la dérivée, après avoir remplacé T_1 par sa valeur, en nous rappelant que $d\rho/dh = \operatorname{tg}\alpha$

$$\begin{aligned} 2d(T_1\rho \sin\alpha)/dh &= d(\rho^2 \Delta P \operatorname{tg}\alpha)/dh \\ &= \rho^2 \operatorname{tg}\alpha\, d\Delta P/dh + 2\Delta P \operatorname{tg}\alpha\, \rho d\rho/dh + \rho^2 \Delta P \cos^{-2}\alpha\, d\alpha/dh \\ &= \rho^2 \operatorname{tg}\alpha\, d\Delta P/dh + 2\rho\Delta P \operatorname{tg}^2\alpha - \rho_1^2 \Delta P/\rho_2 \cos\alpha, \end{aligned}$$

Avec:

$$d\alpha/dh = d\alpha/ds \,.\, ds/dh, \qquad ds/dh = 1/\cos\alpha,$$

$$d\alpha/ds = -1/\rho_2, \qquad \rho/\cos\alpha = \rho_1.$$

ρ_2 est le rayon de courbure dans le plan méridien, ρ_1, le rayon de courbure dans le plan perpendiculaire.

Ecrivons maintenant la troisième force:

$$(11) \qquad (\rho^2 \operatorname{tg}\alpha\, d\Delta P/dh + 2\rho\Delta P \operatorname{tg}^2\alpha - \rho_1^2\, \Delta P/\rho_2 \cos\alpha)dh.$$

Ecrivons que la première force fait équilibre aux deux autres, et tirons T_2.

$$T_2 = \rho\Delta P \cos\alpha + \rho_1 \Delta P \sin^2\alpha/\cos\alpha - \rho_1^2 \Delta P/2\rho_2 + \rho^2 \sin\alpha (d\Delta P/dh)/2$$

$$(12) \qquad T_2 = 2T_1(1 - \rho_1/2\rho_2) + \rho_1^2 \sin\alpha \cos^2\alpha (d\Delta P/dh)/2$$

La formule donnée habituellement pour T_2 dans les traités par exemple celui de Bouasse (2), pp. 604-605, diffère de celle-ci en deux points. Dans l'évaluation de T_1 on suppose que la surpression a partout la valeur maximum qu'elle possède au sommet, et le second terme n'existe pas puisque ΔP est supposé invariable. Cette formule simplifiée donne des tensions T_2 fausses par excès, sauf au sommet, ce qui convient pour certains calculs de résistance de la paroi. La formule actuelle tient compte de la variation avec la hauteur de la surpression.

Pour une sphère, $\rho_1 = \rho_2$, la latitude d'un point sur l'enveloppe est égale à α, et varie entre $-\pi/2$ au sommet et $+\pi/2$ au bas.

(13) $h = \rho_1(1 - \sin\alpha) \quad d\Delta P/dh = 1.196\,P$

(14) $T_1 = 0.598\,\rho_1^2 P(1 - \sin\alpha)$

(15) $T_2 = 0.598\,\rho_1^2 P(1 - \sin\alpha + \sin\alpha\cos^2\alpha) = 0.598\,\rho_1^2 P(1 - \sin^3\alpha)$

T_1 présente un maximum au sommet, pour $\alpha = -\pi/2$; T_2 présente un maximum au sommet, égal à T_1, et un point d'inflexion à l'équateur. T_1 et T_2 présentent un minimum nul au bas.

(16) $$T_{1\max} = T_{2\max} = 1.196\,\rho_1^2 P$$

Supposons qu'il se forme dans le ballon de forme optimum, une bulle sphérique de rayon ρ_1 dans le bas, raccordée à un cône dans le haut. L'angle α à la zone de raccordement est la moitié de l'angle au sommet, ou 48° 11.6′. La hauteur de la bulle est alors 2.34 ρ_1 au lieu de $2\rho_1$ comme dans une sphère. Son méridien d'un pôle à l'autre mesure 3.304 ρ_1 au lieu de 3.1416 ρ_1. La hauteur de la partie conique est 0.595 ρ_1 et le reste de la hauteur de la bulle mesure 1.745 ρ_1. Le volume est $1.0215 \times 4\pi\rho_1^3/3$. Les tensions de $h = 0$ à $h = 1.745\ \rho_1$, ou de $\alpha = 90°$ à $\alpha = -48°\ 11.6'$ sont les mêmes que dans une sphère.

(17) $$T_1 = 0.598\,\rho_1 P h = 0.598\,\rho_1^2 P(1 - \sin\alpha)$$

(18) $$T_2 = 0.598\,\rho_1^2 P(1 - \sin^3\alpha).$$

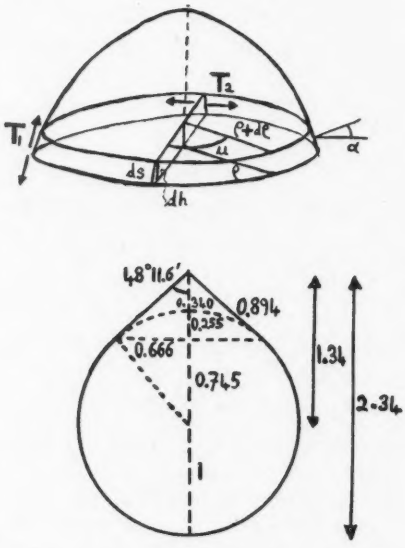

FIG. 5. Calcul des tensions transversales T_2 dans une bulle possédant un axe de symétrie vertical. Calottes ayant à la base des rayons ρ et $\rho + d\rho$, des hauteurs h et $h + dh$.—Bulle au sommet du ballon cylindroconique.

Les plus fortes valeurs se rencontrent au sommet de cette région où:

$$T_1 = 1.042\,\rho_1^2 P, \tag{19}$$

$$T_2 = 0.847\,\rho_1^2 P. \tag{20}$$

La forme est conique entre $h = 1.745\,\rho_1$ et $h = 2.34\,\rho_1$. Le rayon du cercle horizontal qui délimite une calotte conique est $\rho = 1.121(2.34\,\rho_1 - h)$, le rayon de courbure ρ_2 dans le plan méridien est infini, le rayon de courbure dans le plan perpendiculaire que nous distinguerons du rayon de la sphère ρ_1 en l'appelant ρ_3, vaut $\rho_3 = \rho/\cos\alpha = 3\rho/2 = 1.681(2.34\,\rho_1 - h)$, puisque l'angle α est constant. Dans cette région les tensions sont

$$T_1 = 1.006\,Ph(2.34\,\rho_1 - h) \tag{21}$$

$$T_2 = P(2.34\,\rho_1 - h)[2.012h - 0.56(2.34\,\rho_1 - h)]. \tag{22}$$

Les plus fortes valeurs se rencontrent à la base de cette région où:

$$T_1 = 1.043\,\rho_1^2 P, \tag{23}$$

$$T_2 = 1.89\,\rho_1^2 P. \tag{24}$$

Les tensions sont nulles au sommet. T_1 est maximum à la base du cône, T_2 est maximum juste à la base du cône, au dessus de la région sphérique.

Dans ces calculs nous n'avons fait aucune hypothèse sur la distribution des charges. La bulle réelle occupe le haut du ballon et supporte donc par sa base un certain poids, tandis que nous avons trouvé des tensions nulles à la base. L'hypothèse d'une bulle sphérique requiert une distribution spéciale de la charge. Inversement si on considére la forme réelle de la bulle, celle-ci tout en étant à peu près sphérique dans l'ensemble est très complexe, elle est plissée même près du sommet dans les ballons à tête sphérique, et elle est plissée à partir de la base de la région conique dans le ballon de forme optimum. Les tensions ne sont plus données par les formules particulières précédentes: dans la région tendue la forme ne peut pas être celle supposée, par exemple, la bulle peut être plus aplatie au sommet, et dans la région plissée, premièrement les forces verticales sont distribuées sur une paroi de périmètre accru, ce qui réduit la tension T_1, secondement la tension perpendiculaire T_2 doit être très faible puisqu'autrement les plis disparaîtraient.

Au cours de l'ascension, la pression de l'air frappant le sommet de la bulle réduit la surpression s'exerçant dans cette région, ce qui tend à réduire les tensions.

9. LIMITE DE RUPTURE ET PLAFONNEMENT

Avec une marge pour les approximations et les incertitudes dans les calculs précédents, admettons que la tension maximum dans la paroi de la bulle est $2\rho_1^2 P$. La tension maximum augmente avec la dimension de la bulle.* Comme celle-ci doit être d'autant plus grande que le ballon est plus gros, on ne peut,

* *Pour la bulle en Polythène tout juste capable de soulever le ballon, si* $P = 1$:

$$T_{\max} = 0.0632\,n^{4/3}\rho^{2/3}. \tag{25}$$

avec un matériel donné, dépasser une taille maximum, sous peine de voir la bulle se déchirer avant de pouvoir enlever le ballon. Il y a donc une limite à l'altitude accessible, imposée par la limite de rupture du matériel et par son épaisseur. Avec le Polythène, la limite de rupture exprimée en kg. par mètre, est voisine de $2e$, en général elle vaut ke, l'épaisseur e étant exprimée en millièmes de pouce. En fait avec le Polythène, la tension de rupture complète n'est pas atteinte avant $15e$ ou $20e$, mais le matériel s'allonge dès $4e$, et peut se déchirer par endroits vers $6e$. La valeur $k = 2$ assure une bonne marge de sécurité, elle correspond à une bulle de rayon maximum 1 mètre pour $e = 1$.

Eliminant n entre les relations (3) et (4), on trouve une relation entre le rayon de la bulle ρ_1, l'épaisseur et la pression minimum accessible $P_{0\min}$. En posant $T_{\max} = 2\,\rho_1{}^2P = T_{\text{limite}}$, avec $P = 1$ atmosphère, pour le Polythène on trouve:

$$P_{0\min} = 0.0153\, e^{3/4}. \tag{26}$$

Pour une substance de densité quelconque, la formule générale est:

$$P_{0\min} = 0.029\, e^{3/4}\text{densité}^{3/2}/k^{3/4}. \tag{27}$$

Cette formule est importante, car elle montre que l'altitude accessible, loin d'augmenter avec l'épaisseur du matériel, augmente plutôt quand on prend une paroi plus mince. En réduisant l'épaisseur, non seulement on élève le plafond accessible, mais on réduit le poids, comme on l'a vu plus haut Section 7. Une limite pratique est cependant imposée par la fragilité du matériel, qui, s'il est trop mince, risque de se déchirer sous la moindre manipulation. Ainsi on ne pourrait pas manipuler facilement du Polythène de $e = 0.1$. Cependant, d'autres matières plastiques pourraient servir sous des épaisseurs très réduites, comme le nylon qui a une valeur élevée de k, voisine probablement de 60.

Eliminant encore $P_{0\min}$ entre la formule générale donnée ici et une formule précédente, on obtient le poids du ballon de taille maximum pouvant se soulever:

$$W_{\max} = 1.746\,(ek)^{3/2}, \tag{28}$$

on obtient aussi le nombre de fuseaux:

$$n_{\max} = 9.87\, e^{1/4}k^{3/4}/\text{densité}^{1/2}. \tag{29}$$

D'après ces formules, un ballon en nylon, avec $e = 0.01$, une densité voisine de 1, $k = 60$, atteindrait 4×10^{-5} atmosphère, ou environ 60 km. d'altitude, pèserait 810 gr., compterait 67 fuseaux, et aurait une longueur de 229 pieds.

Ces calculs supposent d'ailleurs une paroi homogène. On peut dépasser souvent les limites indiquées en renforçant les parois d'un carrelage de rubans collés, plus solides, selon les principes généraux de constitution des structures telles que les ailes d'avion: un réseau solide supportant une surface mince. Les ballons de General Mills sont renforcés par des rubans rapprochés collés sur la longueur seulement. Dans ce cas, comme dans le cas d'un carrelage de rubans, la paroi est davantage bombée vers l'extérieur, de sorte que les rayons de courbure sont réduits, d'après les formules générales précédentes, les tensions dans la paroi T_1 et T_2 s'en trouvent aussi réduites. Les tensions sont par contre concentrées dans les rubans.

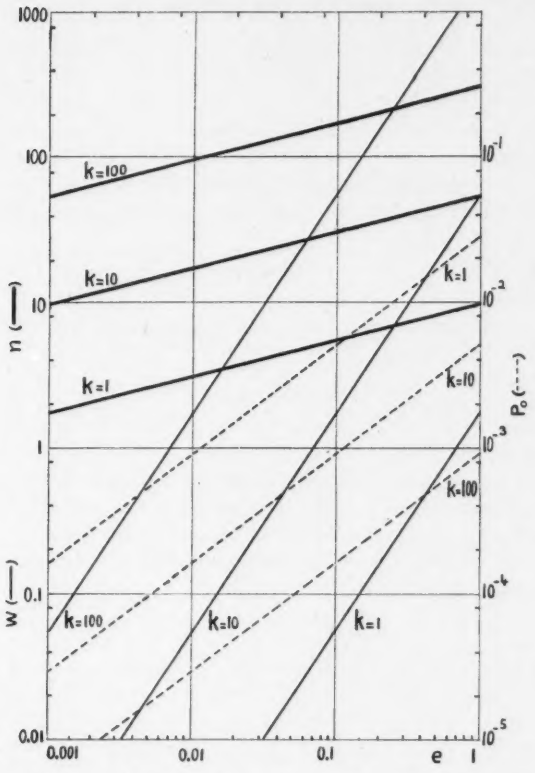

FIG. 6. Ballons cylindroconiques de taille maximum. Diagramme donnant pour trois valeurs du module de rupture k en kg. par mètre et par millième de pouce d'épaisseur, le nombre maximum de fuseaux n, le poids maximum en kg. W, du ballon pouvant tout juste se soulever sans se déchirer, et la pression minimum où il plafonne P_0, en atmosphères. L'abscisse est l'épaisseur e des feuilles employées, en millièmes de pouce. La densité est supposée égale à 1. Si on admet que la fragilité devient excessive lorsque ke vaut 1 kg. par mètre, la plus petite épaisseur utile vaut $1/k$.

Le diagramme Fig. 6 illustre les relations ci-dessus imposées par les limites de rupture.

10. TENSIONS ET ALTITUDE

Les tensions dans la paroi de la bulle diminuent à mesure que l'aérostat s'élève. Le volume de la bulle augmente comme l'inverse de la pression P, son rayon comme $P^{-1/3}$. Si on désigne par T_0 la tension maximum dans la bulle sous la pression normale, sous une autre pression la tension maximum est

$$T = T_0 P^{1/3} \tag{30}$$

elle devient donc moitié quand la pression est réduite d'un facteur huit.

11. DIFFUSION DE L'HYDROGÈNE

L'hydrogène diffuse assez rapidement à travers le Polythène; selon des indications du catalogue de General Mills (3), la perte au sol est d'environ 1 gr. par m.^{2} par heure, l'épaisseur étant d'un millième de pouce, pour un ballon gonflé d'hélium, et doit être comparable pour un ballon gonflé d'hydrogène. La vitesse de diffusion doit être proportionnelle à $1/e$, de sorte que du Polythène beaucoup plus mince présenterait une diffusion gênante. D'autres substances présentent un coefficient de diffusion sans doute plus faible, comme la cellulose et ses éthers, et le nylon.

La diffusion diminue d'importance quand on s'élève; en effet la surface de la bulle est proportionnelle à $P^{-2/3}$, la masse diffusée et la perte de force ascensionnelle sont proportionnelles à cette surface et à la pression de l'hydrogène, donc à $P^{1/3}$. Pour $P = 0.01$ atm., la diffusion est 4.65 fois plus lente qu'au sol.

12. CONCLUSION

La conclusion la plus attrayante de ce travail est probablement la possibilité de construire au laboratoire ou industriellement des ballons très légers capables d'atteindre au moins 45 ou 50 km. d'altitude et d'y plafonner. Ils constitueraient un moyen précieux pour l'étude des rayons cosmiques primaires. Le Polythène très mince, même renforcé de ruban gommé, serait trop fragile et perdrait trop rapidement son gaz, mais il devrait se trouver d'autres matières thermoplastiques solides et imperméables utilisables à cette fin.

13. REMERCIEMENTS

Nous remercions le Conseil National des Recherches, pour un octroi qui a facilité l'exécution de ce travail. Nous remercions aussi la Compagnie Canadian Industries Limited qui a gracieusement fourni des échantillons de Polythène, et qui nous a accordé une contribution pour l'étude des rayons cosmiques.

BIBLIOGRAPHIE

1. ALLEN, K. W. et DEWAN, J. T. Phys. Rev. 82:527. 1951.
2. BOUASSE, H. Cours de mécanique physique. Delagrave, Editeurs, Paris. 1912.
3. GENERAL MILLS CO. Catalogues: Technical data, Plastic balloons, Airlift to the stratosphere. Minneapolis, Minn. 1950 et antérieurement.
4. HEITLER, H. K. et KING, D. T. Experientia, 8:281. 1950.
5. MOORE, C. B. et SMITH, J. R. Constant level balloons, Sec. 2, Technical Report No. 93-02,. College of Engineering, New York University. 1949.
6. RYAN, W. Sealing of polythene, Modern Packaging Magazine. December, 1949.

TRANSFORMATION AMPLITUDES FOR VECTOR ADDITION OF ANGULAR MOMENTUM; $(j3mm'|j3JM)$[1]

By D. L. Falkoff,[2] G. S. Colladay, and R. E. Sells

ABSTRACT

The transformation amplitudes for the quantum-mechanical vector addition of angular momenta, $\vec{j} + \vec{3} = \vec{J}$ are given.

Much of the current work in nuclear spectroscopy is concerned with the angular distributions of the particles emitted in nuclear reactions or in transitions between nuclear states, for such experiments yield information about the angular momenta of the states and particles involved. The quantitative treatment of such processes invariably requires a knowledge of the transformation amplitudes for the vector addition of the relevant angular momenta (see, for example, Falkoff and Uhlenbeck, (2)). The required transformation amplitudes, $(jj'mm'|jj'JM)$, for the vector addition of the angular momenta $\vec{j} + \vec{j}' = \vec{J}$, $m + m' = M$, have been tabulated by Condon and Shortley (1) for $j' = \frac{1}{2}$, 1, 3/2, and 2, thus amply fulfilling the needs of atomic spectroscopy. To help meet the need in nuclear applications where higher angular momenta are more common, we have prepared the accompanying table* for $j' = 3$.

The transformation amplitudes for $j' = 3$ form a real, unitary matrix the seven rows of which are indexed by $\Delta j = J - j = +3, 2, \ldots, -3$, and the seven columns by $\Delta m = m' = M - m = 3, \ldots, -3$. We obtained these matrix elements by first evaluating the unnormalized Clebsch-Gordan coefficients, $C^J_{mm'}$, derived by group-theoretical methods by van der Waerden (6). Then the normalizing factors common to elements in each row were obtained from the simple closed form given by Keller (4). The phase convention is the same as that used by Condon and Shortley.

Since these matrix elements apply to the emission of any particle with $j' = 3$, they may also be used for γ-octupole radiation, and they do in fact yield the same j and $m = M - m'$ dependence as the matrix elements obtained specifically for this case by French (3) following a method which Condon and Shortley had used for quadrupole matrix elements. Their derivation has the merit that it also gives the directional and polarization properties of the radiation field in a convenient vector form. But neither the quadrupole nor octupole matrix elements so obtained may be used as they stand for transformation amplitudes for the emission of particles other than γ-rays. This is because the matrix elements are not properly normalized and the sign conventions are not such as to yield a unitary matrix. For the applications to the *pure* multipole γ-radiation these discrepancies in

[1] *Manuscript received October 15, 1951.*
Contribution from the University of Notre Dame, Notre Dame, Ind.
[2] *Now at the Lincoln Laboratory, Massachusetts Institute of Technology, Cambridge, Mass.*

**Our notation differs slightly from that of Condon and Shortley: in their notation the matrix element which we denote by $(jj'mm'|jj'JM)$ would read $(j_1j_2m_1m_2|j_1j_2jm)$ and would be tabulated in terms of j_1 and m rather than j and M as here.*

normalization and sign are of no consequence since they are compensated in the definition of the associated angular dependent factor for the electromagnetic radiation field. However, if *mixtures* of multipole fields, as for example, both octupole and quadrupole, were present in a single radiative transition, then, as shown by Ling and Falkoff (5), it would again be necessary to use the *normalized* transformation amplitudes to obtain the correct interference contribution to the angular distribution.

ACKNOWLEDGMENTS

This work was supported in part by the joint program of the AEC and ONR at the University of Notre Dame.

REFERENCES

1. CONDON, E. U. and SHORTLEY, G. H. The theory of atomic spectra. Cambridge at the University Press. 1935.
2. FALKOFF, D. L. and UHLENBECK, G. E. Phys. Rev. 79:323. 1951.
3. FRENCH, A. P. Phil. Mag. 42:263. 1951.
4. KELLER, J. M. Phys. Rev. 55:508. 1939.
5. LING, D. S., JR. and FALKOFF, D. L. Phys. Rev. 76:1639. 1949.
6. VAN DER WAERDEN, B. L. Die gruppentheoretischen Methode in der Quantenmechanik. Verlag von Julius Springer, Berlin. 1932.

TABLE OF TRANSFORMATION AMPLITUDES

$(j\,3\,mm' \mid j\,3\,J\,M)$

Column 1 ($m' = 3$)

$J = j+3$	$\sqrt{\dfrac{(j+M-2)(j+M-1)(j+M)(j+M+1)(j+M+2)(j+M+3)}{8(j+1)(j+2)(j+3)(2j+1)(2j+3)(2j+5)}}$
$j+2$	$-\sqrt{\dfrac{3(j+M-2)(j+M-1)(j+M)(j+M+1)(j+M+2)(j-M+3)}{8j(j+1)(j+2)(j+3)(2j+1)(2j+3)}}$
$j+1$	$\sqrt{\dfrac{15(j+M-2)(j+M-1)(j+M)(j+M+1)(j-M+2)(j-M+3)}{8j(j+1)(j+2)(2j+1)(2j+5)(2j-1)}}$
j	$-\sqrt{\dfrac{5(j+M-2)(j+M-1)(j+M)(j-M+1)(j-M+2)(j-M+3)}{4j(j+1)(j+2)(j-1)(2j+3)(2j-1)}}$
$j-1$	$\sqrt{\dfrac{15(j-M+3)(j-M+2)(j-M+1)(j-M)(j+M-1)(j+M-2)}{8(j+1)j(j-1)(2j+1)(2j-3)(2j+3)}}$
$j-2$	$-\sqrt{\dfrac{3(j-M+3)(j-M+2)(j-M+1)(j-M)(j-M-1)(j+M-2)}{8(j+1)j(j-1)(j-2)(2j+1)(2j-1)}}$
$j-3$	$\sqrt{\dfrac{(j-M+3)(j-M+2)(j-M+1)(j-M)(j-M-1)(j-M-2)}{8j(j-1)(j-2)(2j+1)(2j-1)(2j-3)}}$

Column 2 ($m' = 2$)

$J = j+3$	$\sqrt{\frac{3(j-M+3)(j+M-1)(j+M)(j+M+1)(j+M+2)(j+M+3)}{4(j+1)(j+2)(j+3)(2j+1)(2j+3)(2j+5)}}$
$j+2$	$-\left(j-\frac{3}{2}M+3\right)\sqrt{\frac{(j+M-1)(j+M)(j+M+1)(j+M+2)}{j(j+1)(j+2)(j+3)(2j+1)(2j+3)}}$
$j+1$	$(j-3M+4)\sqrt{\frac{5(j-M+2)(j+M-1)(j+M)(j+M+1)}{4j(j+1)(j+2)(2j+1)(2j+5)(2j-1)}}$
j	$(M-1)\sqrt{\frac{15(j+M)(j-M+1)(j-M+2)(j+M-1)}{2j(j+1)(j+2)(j-1)(2j+3)(2j-1)}}$
$j-1$	$-(j+3M-3)\sqrt{\frac{5(j+M-1)(j-M+2)(j-M+1)(j-M)}{4(j+1)j(j-1)(2j+1)(2j-3)(2j+3)}}$
$j-2$	$\left(j+\frac{3}{2}M-2\right)\sqrt{\frac{(j-M+2)(j-M+1)(j-M)(j-M-1)}{(j+1)j(j-1)(j-2)(2j+1)(2j-1)}}$
$j-3$	$-\sqrt{\frac{3(j+M-2)(j-M+2)(j-M+1)(j-M)(j-M-1)(j-M-2)}{4j(j-1)(j-2)(2j+1)(2j-1)(2j-3)}}$

Column 3 ($m' = 1$)

$J = j+3$	$\sqrt{\frac{15(j-M+2)(j-M+3)(j+M)(j+M+1)(j+M+2)(j+M+3)}{8(j+1)(j+2)(j+3)(2j+1)(2j+3)(2j+5)}}$
$j+2$	$-(j-3M+3)\sqrt{\frac{5(j-M+2)(j+M)(j+M+1)(j+M+2)}{8j(j+1)(j+2)(j+3)(2j+1)(2j+3)}}$
$j+1$	$-\left\{j(j+7)+10(M-1)\left(j-\frac{3}{2}M+1\right)\right\}\sqrt{\frac{(j+M)(j+M+1)}{8j(j+1)(j+2)(2j+1)(2j+5)(2j-1)}}$
j	$\left\{j(j+1)-5M(M-1)-2\right\}\sqrt{\frac{3(j-M+1)(j+M)}{4j(j+1)(j+2)(j-1)(2j+3)(2j-1)}}$
$j-1$	$-\left\{(j+1)(j-6)-10(M-1)\left(j+\frac{3}{2}M\right)\right\}\sqrt{\frac{(j-M+1)(j-M)}{8(j+1)j(j-1)(2j+1)(2j-3)(2j+3)}}$
$j-2$	$-(j+3M-2)\sqrt{\frac{5(j+M-1)(j-M+1)(j-M)(j-M-1)}{8(j+1)j(j-1)(j-2)(2j+1)(2j-1)}}$
$j-3$	$\sqrt{\frac{15(j+M-1)(j+M-2)(j-M+1)(j-M)(j-M-1)(j-M-2)}{8j(j-1)(j-2)(2j+1)(2j-1)(2j-3)}}$

Column 4 ($m' = 0$)

$J = j+3$	$\sqrt{\frac{5(j-M+1)(j-M+2)(j-M+3)(j+M+1)(j+M+2)(j+M+3)}{2(j+1)(j+2)(j+3)(2j+1)(2j+3)(2j+5)}}$
$j+2$	$M\sqrt{\frac{15(j-M+1)(j-M+2)(j+M+1)(j+M+2)}{2j(j+1)(j+2)(j+3)(2j+1)(2j+3)}}$
$j+1$	$-\left\{j(j+2)-5M^2\right\}\sqrt{\frac{3(j+M+1)(j-M+1)}{2j(j+1)(j+2)(2j+1)(2j+5)(2j-1)}}$
j	$-M\left\{3j(j+1)-5M^2-1\right\}\sqrt{\frac{1}{j(j+1)(j+2)(j-1)(2j+3)(2j-1)}}$
$j-1$	$(j^2-5M^2-1)\sqrt{\frac{3(j-M)(j+M)}{2(j+1)j(j-1)(2j+1)(2j-3)(2j+3)}}$
$j-2$	$M\sqrt{\frac{15(j+M)(j+M-1)(j-M)(j-M-1)}{2(j+1)j(j-1)(j-2)(2j+1)(2j-1)}}$
$j-3$	$-\sqrt{\frac{5(j+M)(j+M-1)(j+M-2)(j-M)(j-M-1)(j-M-2)}{2j(j-1)(j-2)(2j+1)(2j-1)(2j-3)}}$

Column 5 ($m' = -1$)

$J = j+3$	$\sqrt{\frac{15(j+M+2)(j+M+3)(j-M)(j-M+1)(j-M+2)(j-M+3)}{8(j+1)(j+2)(j+3)(2j+1)(2j+3)(2j+5)}}$
$j+2$	$(j+3M+3)\sqrt{\frac{5(j+M+2)(j-M)(j-M+1)(j-M+2)}{8j(j+1)(j+2)(j+3)(2j+1)(2j+3)}}$
$j+1$	$-\left\{j(j+7)-10(M+1)\left(j+\frac{3}{2}M+1\right)\right\}\sqrt{\frac{(j-M)(j-M+1)}{8j(j+1)(j+2)(2j+1)(2j+5)(2j-1)}}$
j	$-\left\{j(j+1)-5M(M+1)-2\right\}\sqrt{\frac{3(j+M+1)(j-M)}{4j(j+1)(j+2)(j-1)(2j+3)(2j-1)}}$
$j-1$	$-\left\{(j+1)(j-6)+10(M+1)\left(j-\frac{3}{2}M\right)\right\}\sqrt{\frac{(j+M+1)(j+M)}{8(j+1)j(j-1)(2j+1)(2j-3)(2j+3)}}$
$j-2$	$(j-3M-2)\sqrt{\frac{5(j-M-1)(j+M+1)(j+M)(j+M-1)}{8(j+1)j(j-1)(j-2)(2j+1)(2j-1)}}$
$j-3$	$\sqrt{\frac{15(j-M-1)(j-M-2)(j+M+1)(j+M)(j+M-1)(j+M-2)}{8j(j-1)(j-2)(2j+1)(2j-1)(2j-3)}}$

Column 6 ($m' = -2$)

$J = j+3$	$\sqrt{\frac{3(j+M+3)(j-M-1)(j-M)(j-M+1)(j-M+2)(j-M+3)}{4(j+1)(j+2)(j+3)(2j+1)(2j+3)(2j+5)}}$
$j+2$	$\left(j+\frac{3}{2}M+3\right)\sqrt{\frac{(j-M-1)(j-M)(j-M+1)(j-M+2)}{j(j+1)(j+2)(j+3)(2j+1)(2j+3)}}$
$j+1$	$(j+3M+4)\sqrt{\frac{5(j+M+2)(j-M-1)(j-M)(j-M+1)}{4j(j+1)(j+2)(2j+1)(2j+5)(2j-1)}}$
j	$(M+1)\sqrt{\frac{15(j-M)(j+M+1)(j+M+2)(j-M-1)}{2j(j+1)(j+2)(j-1)(2j+3)(2j-1)}}$
$j-1$	$-(j-3M-3)\sqrt{\frac{5(j-M-1)(j+M+2)(j+M+1)(j+M)}{4(j+1)j(j-1)(2j+1)(2j-3)(2j+3)}}$
$j-2$	$-\left(j-\frac{3}{2}M-2\right)\sqrt{\frac{(j+M+2)(j+M+1)(j+M)(j+M-1)}{(j+1)j(j-1)(j-2)(2j+1)(2j-1)}}$
$j-3$	$-\sqrt{\frac{3(j-M-2)(j+M+2)(j+M+1)(j+M)(j+M-1)(j+M-2)}{4j(j-1)(j-2)(2j+1)(2j-1)(2j-3)}}$

Column 7 ($m' = -3$)

$J = j+3$	$\sqrt{\frac{(j-M-2)(j-M-1)(j-M)(j-M+1)(j-M+2)(j-M+3)}{8(j+1)(j+2)(j+3)(2j+1)(2j+3)(2j+5)}}$
$j+2$	$\sqrt{\frac{3(j-M-2)(j-M-1)(j-M)(j-M+1)(j-M+2)(j+M+3)}{8j(j+1)(j+2)(j+3)(2j+1)(2j+3)}}$
$j+1$	$\sqrt{\frac{15(j-M-2)(j-M-1)(j-M)(j-M+1)(j+M+2)(j+M+3)}{8j(j+1)(j+2)(2j+1)(2j+5)(2j-1)}}$
j	$\sqrt{\frac{5(j-M-2)(j-M-1)(j-M)(j+M+1)(j+M+2)(j+M+3)}{4j(j+1)(j+2)(j-1)(2j+3)(2j-1)}}$
$j-1$	$\sqrt{\frac{15(j+M+3)(j+M+2)(j+M+1)(j+M)(j-M-1)(j-M-2)}{8(j+1)j(j-1)(2j+1)(2j-3)(2j+3)}}$
$j-2$	$\sqrt{\frac{3(j+M+3)(j+M+2)(j+M+1)(j+M)(j+M-1)(j-M-2)}{8(j+1)j(j-1)(j-2)(2j+1)(2j-1)}}$
$j-3$	$\sqrt{\frac{(j+M+3)(j+M+2)(j+M+1)(j+M)(j+M-1)(j+M-2)}{8j(j-1)(j-2)(2j+1)(2j-1)(2j-3)}}$

THE MEASUREMENT OF PHOTONUCLEAR CROSS SECTIONS IN ISOTOPES LEADING TO SHORT-LIVED DECAY PRODUCTS[1]

By R. N. H. Haslam, R. G. Summers-Gill,[2] and E. H. Crosby[3]

ABSTRACT

A dropping apparatus, including a new means of dosage rate monitoring, has been designed to allow the observation of short-lived activities produced by betatron irradiation of various parent materials. The photonuclear cross section for the reaction $S^{32}(\gamma, n)S^{31}$ has been measured by this means. The cross section has a peak value of 24.6 millibarns at 20.1 $\pm$ 0.5 Mev., a half width of 4.5 Mev., and an integrated cross section of 0.12 Mev-barns. The reaction threshold was found to be 15.0 $\pm$ 0.1 Mev. The experiment has also yielded a new half life for S^{31} — 2.66 $\pm$ 0.03 sec.

INTRODUCTION

While considerable work has been done in finding cross sections for photonuclear reactions in the middle-weight elements, such information is lacking for many isotopes which yield radioactive end products with half lives less than five seconds.

This paper describes an apparatus which permits the study of these short-lived activities and submits the results for the reaction $S^{32}(\gamma, n)S^{31}$.

APPARATUS

All irradiations were made using the 25 Mev. betatron at the University of Saskatchewan. In order to facilitate the rapid transfer of samples from irradiation position to counting position, a remote-controlled dropping apparatus has been designed. See Fig. 1.

The heart of the apparatus is a lucite framework $12\frac{1}{2}$ in. $\times$ 6 in. $\times$ $5\frac{1}{2}$ in. which rests on a shelf bolted to the front of the betatron shield. The collimated beam passes through a square opening in the front of this lucite structure with its center 6 in. above the base. Provision is made at the top for suspending in a vertical position a 4 ft. long brass guide rod $\frac{7}{8}$ in. in diameter. This rod passes through a hole in the base. A brass shelf is fastened to a horizontal axle conveniently mounted behind this guide rod and just below the center of the beam. Another similar shelf is positioned above the first and out of the beam. These shelves are held against gravity in the horizontal position by lever arms attached to two independent electromagnets on the top of the assembly. Cylindrical samples which slide freely on the guide rod may thus be held first above the beam, then dropped at the desired instant to a position at the center of the beam, and finally, dropped again to the bottom of the guide rod where the counting is done.

A Victoreen 1B85 thyrode counting tube is fitted within a specially machined hollow lucite rod attached as an extension of the guide rod. The two parts of the guide rod are readily separable thus facilitating the changing of samples. To keep

[1] *Manuscript received November 26, 1951.*
Contribution from the Betatron Group, University of Saskatchewan, Saskatoon, Sask.
[2] *Holder of a National Research Council of Canada bursary, 1951-52.*
[3] *Holder of a National Research Council of Canada bursary (1950-51) and studentship* (1951-52).

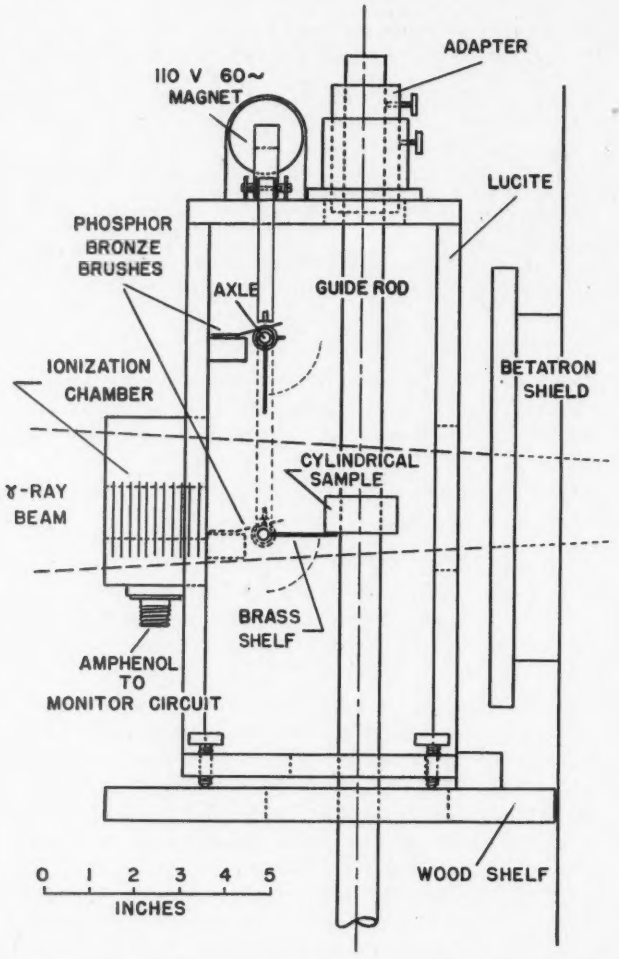

FIG. 1. The dropping apparatus viewed from the side showing a cylindrical sample in the irradiation position. For use with end-on counters, the adapter and guide rod shown are removed and a larger hollow brass guide rod installed.

the tube background to a minimum, the lower end of the guide rod, containing the tube, projects inside a cylindrical castle. The outside wall of lead is 1 in. thick. Constructional details of the inner linings of wax, cadmium, and lead are shown in Fig. 2. This special design was followed to eliminate fast neutrons present unavoidably in the photon beam. Slowed to thermal energies by the wax, they are captured in the cadmium. γ-rays emitted by the excited cadmium nuclei are absorbed in the inner lead foil. In this way, the tube background immediately

after an irradiation, owing principally to neutron capture in the aluminum of the counting tube, was reduced by a factor of five.

The Geiger–Müller tube is connected to the usual preamplifier scaler circuits. A Nuclear Instruments scaler and an Atomic Instruments scaler are arranged in series giving a scaling factor variable from 8 × 8 to 128 × 64. The outputs from these two scalers are fed to the two pens of a BL – 202 double channel oscillograph manufactured by the Brush Development Co. Fig. 3 shows a block diagram

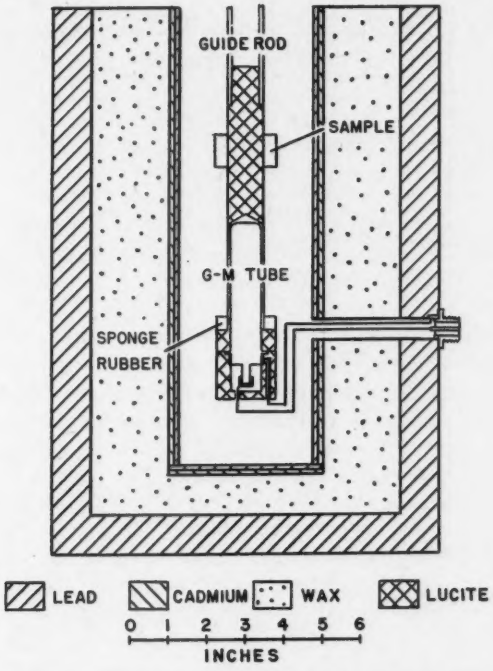

FIG. 2. The specially designed castle showing detail of thyrode tube mounting. Notice the cylindrical sample part way down the guide rod.

of the electronic equipment used in conjunction with the dropping apparatus. The oscillograph records the output pulses as pips of constant height on a tape which, for this work, traveled at 0.5 cm. per sec. The chart drive speed was checked from time to time during runs with a 60 cycle test signal.

In order to record on the tape the beginning and end of irradiation, a circuit is provided to apply a fixed d-c. bias to one of the pens at the instant the upper shelf is released. The same circuit is broken again when the lower shelf is also tripped. This is effected by means of slip rings fastened on the shelf axles. Phosphor bronze brushes make and break the circuit as the shelves are rotated.

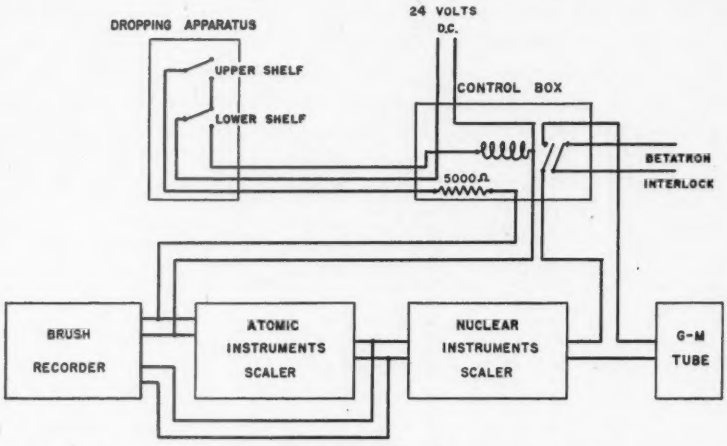

FIG. 3. Block diagram of control circuit used. The 110 volt magnets (not shown) are operated by remote control from a switchboard which is also provided with a switch to start and stop the Brush recorder chart drive.

An interlock circuit of the betatron also is broken with the release of the lower shelf, thus instantly turning off the beam.

It was found also that unpredictable tube behavior resulted if the high voltage remained on the Geiger tube during operation of the betatron. This phenomenon is due to the high photon flux present everywhere in the room. Therefore the same relay, which breaks the interlock circuit, is also wired to close the otherwise open circuit from the high tension supply to the thyrode. The time constant, governing the rise in potential of the tube, was found to be small and the tube reaches its operating voltage in approximately one second. Since the sample requires nearly this length of time to descend the four feet to the counting position, little delay in counting is caused.

In order to obtain an activation curve it is necessary to know the dosage rate and the time of irradiation for each sample. The number of radioactive atoms N present in a sample after an irradiation time t is given by

$$N = k\int_0^t D(\tau)e^{-\lambda\tau}d\tau$$

where $D(\tau)$ is the dosage rate at time τ measured backward from the end of irradiation,

λ is the transformation constant of the radioactivity being produced,

and k is a constant of proportionality and is essentially the activation value.

If $D(\tau)$ is a constant $(= D)$, the integration can be performed and

$$N = \frac{k}{\lambda}D(1 - e^{-\lambda t}).$$

Also, if $t \ll 1/\lambda$, $N \approx kD\lambda t/\lambda = kDt = kQ$ where Q is termed the total integrated dose.

In general, $D(\tau)$ is not a constant and this expression cannot be integrated. But even in this case, if $t \ll 1/\lambda$, the factor $e^{-\lambda\tau}$ is approximately unity over the entire integration and

$$N \approx k\int_0^t D(\tau)d\tau = kQ.$$

In words, if the irradiation time is much less than the half life, the activity produced is a linear function of the integrated dose only and variations in dose rate are inconsequential. This is the basis of conventional integrated-dose monitoring with a Victoreen r-meter.

Because of changes in line frequency, magnet temperature, etc., transient variations in betatron yield as large as 20% are unavoidable. Since the half lives in this work are short, near saturation irradiations are obtained in a few seconds. The dose rate near the end of irradiation is, therefore, very much more important than at the beginning of the irradiation period. Since the weighting function $e^{-\lambda\tau}$ cannot be neglected, integrated-dose monitoring is inaccurate.

Instead, a method of dynamic monitoring is used which yields a continuous graph of the varying dose rate over the entire irradiation period. The circuit is shown in Fig. 4. The output from a small multiple-plate ionization chamber, attached in fixed geometry to the rear of the dropping apparatus, is fed to the grid of a cathode follower Victoreen 5803 triode. The grid resistor normally used

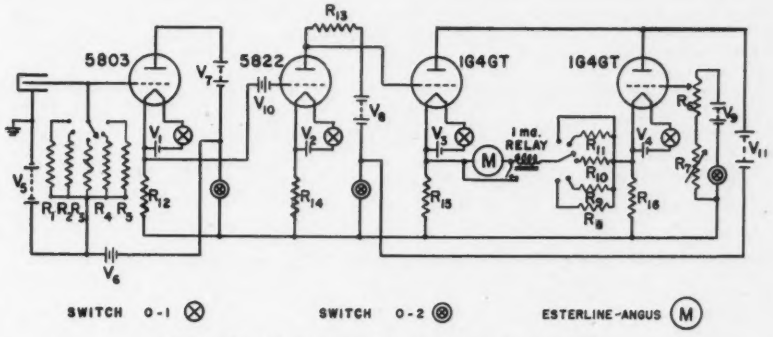

Fig. 4. Circuit diagram of dynamic monitoring device.

R_1	20 megohms	R_{10}	15 K	V_3	1.5 volt "A"
R_2	40 megohms	R_{11}	50 K	V_4	1.5 volt "A"
R_3	80 megohms	R_{12}	50 K prec.	V_5	300 volt Minimax
R_4	150 megohms	R_{13}	500 K prec.	V_6	3 volt penlight
R_5	1000 megohms	R_{14}	10 K wire wound	V_7	9 volt penlight
R_6	1 megohm pot.	R_{15}	10 K wire wound	V_8	67.5 volt Minimax
R_7	25 K variable	R_{16}	10 K wire wound	V_9	30 volt Minimax
R_8	1500 ohms	V_1	1.25 volt "A"	V_{10}	4.5 volt penlight
R_9	5000 ohms	V_2	1.25 volt "A"	V_{11}	90 volt Minimax

The 1 ma. relay shorts out the Esterline–Angus meter if the current becomes excessive. Filament supplies are turned on before plate supplies to prevent destabilization of the electrometer tubes.

is 80 megohms. The second stage Victoreen 5822 medium-mu triode has an amplification factor of 10. The balanced-output cathode-follower arrangement permits the use of an Esterline–Angus recording milliammeter with full scale deflection of 1.0 ma. The circuit is linear within 2% over the full scale of the meter. A typical dose rate chart is depicted in Fig. 5. While the above circuit was used for the work on sulphur, a recording instrument with a shorter response time would be preferable and a newer circuit using a Speedomax recorder, fully described by Johns *et al.* (5), will be used in future.

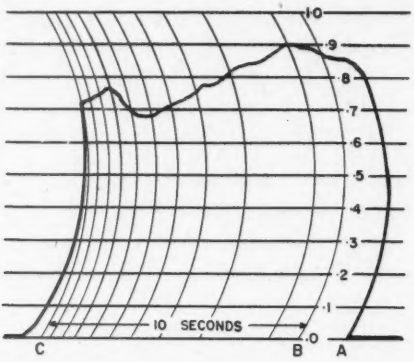

FIG. 5. Typical Esterline–Angus chart showing the dosage variation over a 10 sec. irradiation of sulphur. The light grid lines are placed at the times t_n as calculated for a half life of 2.66 sec. The effective dosage rate is 0.75 while the mean integrated dosage rate is 0.80, a difference of 6.7%. At *A* the betatron beam was turned on, at *B* the sample was dropped into place for a 10 sec. irradiation, and at *C* the beam was automatically cut off as the sample dropped to the counting position.

If one considers that the dosage rate $D(\tau)$ varies only in finite steps taking on the values $\bar{D}_1, \bar{D}_2, \ldots \bar{D}_m$ during an irradiation of length t_m (long compared to the half life), then

$$N = k \sum_{n=1}^{m} \bar{D}_n \int_{t_{n-1}}^{t_n} e^{-\lambda \tau} d\tau$$

where t_n are the points of discontinuity. Carrying out the integration,

$$N = \frac{k}{\lambda} \sum_{n=1}^{m} \bar{D}_n (e^{-\lambda t_{n-1}} - e^{-\lambda t_n}).$$

If the dosage rate were constant for the irradiation we would have

$$N = \frac{k}{\lambda} D(1 - e^{-\lambda t_m}) \approx \frac{k}{\lambda} D.$$

If the dosage rate is variable, we can define an effective dosage rate D_{eff} by the relation

$$N = \frac{k}{\lambda} D_{\text{eff}} (1 - e^{-\lambda t_m}) \approx \frac{k}{\lambda} D_{\text{eff}}.$$

It is this effective dose rate that we desire to find. Comparison of the two expressions for N yields

$$D_{\text{eff}} = \sum_{n=1}^{m} \bar{D}_n (e^{-\lambda t_{n-1}} - e^{-\lambda t_n}).$$

We now apply this equation to the analysis of a dosage rate chart. If the continuous graph could be divided into m intervals of variable duration so that the expression $(e^{-\lambda t_{n-1}} - e^{-\lambda t_n})$ would have the same value $1/m$ for each interval, considerable simplification in the calculation of D_{eff} would result. This criterion leads at once to an expression for the t_n, namely,

$$t_n = \frac{1}{\lambda} \ln\left(\frac{m}{m-n}\right) \qquad n = 1, 2, \ldots, m-1.$$

If we denote the average dose rate in the n^{th} interval from t_{n-1} to t_n by $\bar{D}_n$ where t_n is as above, then

$$D_{\text{eff}} = \frac{1}{m} \sum_{n=1}^{m} \bar{D}_n.$$

Since irradiations are only of finite duration, the m^{th} interval cannot be completely represented on the dosage rate chart. However, little error is introduced by writing $\bar{D}_m = D_{\text{eff}}$. Collecting terms, we have,

$$D_{\text{eff}} = \frac{1}{m-1} \sum_{n=1}^{m-1} \bar{D}_n.$$

The value of m can be chosen large enough to give any desired degree of accuracy. For this work m was taken as 10, so that

$$D_{\text{eff}} = \frac{1}{9} \sum_{n=1}^{9} \bar{D}_n.$$

This is readily evaluated by examining the dosage rate chart with the help of a lucite template scribed with grid lines at each of the times t_n and estimating each of the $\bar{D}_n$ values. These lines are shown superimposed on Fig. 5. The positions of the lines are, of course, functions of the half life, so that a new template is necessary for each different half life.

The Brush Oscillograph tape records the decay of each sample. To obtain the counting rate for a given sample as a function of time measured from the end of irradiation, it is necessary to measure the linear distance from the release of the d-c. bias to each of the subsequent pips in suitable groupings. If these readings are denoted by S_1, S_2, etc., then the counting rate at time $\frac{1}{2}(S_1 + S_2) \times 1/0.5$ (seconds) is given by $0.5 \times N/(S_2 - S_1)$ (counts per second), where N is the number of counts received in the interval of time between S_1 and S_2, assuming a chart speed of 0.5 cm. per sec. Initially, while the counting rate is high, pips are counted on the output track of the second scaler. As the counting rate decreases, the other track bearing the register pulses from the first scaler is used.

To facilitate the measurement of S_1, S_2, etc., a tape reader was built. As the paper is wound from one drum to another, it passes tightly over a rubber roller geared to a revolution counter. The position of each pip is recorded as the reading

on the revolution counter which is calibrated to 0.01 of a turn, and can be estimated to 0.001 of a turn. For the chart speed used, one revolution on the revolution counter corresponds to 5.32 sec. This calibration was checked from time to time by measuring the half centimeter grid lines on the tape.

Because of the inherent filtration of the above counting system (minimum tube wall of a thyrode is 30 mgm. per cm.^{2}) and for other reasons, cylindrical geometry was discarded in favor of end-on counting for the absolute determination of activities. On the other hand, cylindrical samples giving the highest possible counting rates are desirable in the relative work when irradiations near threshold are to be made. The dropping apparatus described is easily adaptable to the other form of counting geometry as shown in Fig. 6. The same castle can be fitted with an RCL end-on counting tube with a mica window 2.9 mgm. per cm.^{2} in thickness. A hollow brass rod of inside diameter 1 7/16 in. replaces the smaller guide rod of the other assembly. This is again suspended from its upper end by the lucite superstructure. Its lower end butts rigidly against the counting tube so that samples may be dropped to within 5 mm. of the window without damage to either the samples or the tube. A lengthwise slot cut in the upper end

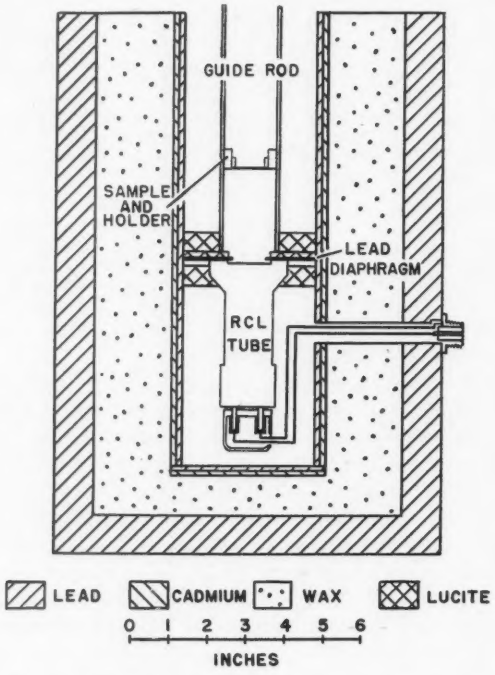

FIG. 6. The castle again, showing details of the end-on counting geometry. Notice the carbon sample holder dropping inside the guide.

of this rod permits narrow projections on the supporting shelves to extend part way inside the guide. Carbon sample holders were machined to slide freely inside this guide. Carbon was chosen because of its high (γ,n) threshold, low cross section, and long half life relative to the half lives being studied. Circular disks of the sample material are supported between layers of plastic film held flat across the end of these holders. Strings attached to the tops of the holders provide a means of recovery after the counting time has elapsed.

THE REACTION SULPHUR$^{32}(\gamma, n)$ SULPHUR^{31}

The first reaction studied with the apparatus was $S^{32}(\gamma, n)S^{31}$, whose product nucleus has a half life of 2.66 sec. The experiment readily divides itself into two parts. First, a relative activation curve as a function of maximum betatron energy was determined. Finally, the absolute magnitude of the activity was determined at one energy, namely 22 Mev. To avoid geometry and absolute dose calculations, the activity produced in sulphur was compared directly with the (γ,n) activity produced in similar copper samples.

As indicated above, cylindrical geometry was used in determining the relative activity curve. No attention was paid to geometry or self-absorption corrections and all dosage rates were left in units of ionization current. Irradiations were, in general, of 10 sec. duration. The sulphur samples were cast as cylinders 4 cm. in diameter, with a 2.4 cm. diameter hole through the center. They ranged in length from 1.5 to 2.5 cm. and had masses from 22 to 37 gm.

To permit counting over as long a period as possible, corrections for tube dead time were obtained experimentally and applied at counting rates over 6×10^4 counts per minute. Although Victoreen thyrode tubes are well adapted to high counting rates, the correction amounts to over 100% at 5×10^5 counts per minute. The correction factor was obtained by following the decay of a pure 10.1 min. Cu^{62} activity over a period of 90 min. The straight line portion (on semi-log paper) was then produced back to the time origin and the counting loss correction found as a function of observed counting rate.

Points on the activation curve were obtained at intervals of less than 0.4 Mev. and repeated many times on different days and using different samples. The maximum energy of the betatron was controlled using the circuits previously described (9). Separate plots of initial counting rate per gram sulphur per unit photon intensity were obtained for each run using one sample throughout, and the best-fitting curves normalized to each other as well as possible at all energies. The experimental points for each run were then multiplied by the appropriate normalization factor and plotted on the mean curve as shown in Fig. 7.

As already mentioned, the absolute magnitude of the above curve was determined by comparing activities obtained in sulphur and copper at 22 Mev. This energy was chosen as the one giving the largest sulphur activity with a minimum of activity produced in the carbon of the sample holders. Since only a ratio of activities was to be determined and the actual specific activity per atom Cu^{63} per 100 r. per min. obtained from previous work, the geometry factor did

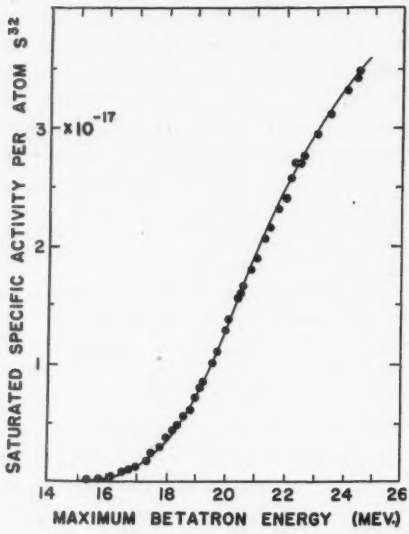

FIG. 7. Activation curve for the reaction $S^{32}(\gamma, n)S^{31}$. Experimental points shown represent the average of at least three actual determinations.

not have to be measured provided it was the same in both cases. It was essential, however, to apply self-absorption corrections.

Circular copper foils ranging in thickness from 419 mgm. per cm.^{2} to 5.9 mgm. per cm.^{2} and 4.98 cm.^{2} in area were used to determine a self-absorption curve in copper. Circular sulphur samples of the same diameter and thicknesses ranging from 987 mgm. per cm.^{2} to 15.1 mgm. per cm.^{2} were used similarly to determine the self-absorption curve in sulphur. The samples were held during both irradiation and counting in the sample holders already described above. Although rapid sample transport was not necessary to measure the Cu^{62} decay, the procedure followed was the same as for the measurement of the sulphur activity. The self-absorption curves were then extrapolated to zero thickness and the ratio of extrapolated values taken. Although S^{31} decays by positron emission, no correction need be made for unobserved K-electron capture since this effect is less than 1% (4). The probable error in the determination of points on the relative activation curve is estimated to be less than 3%. A more serious error occurs in the determination of the ratio between the activities of sulphur and copper at 22 Mev., that is, in the fixing of the absolute ordinate scale. This error is due to uncertainties in the extrapolated values of the self-absorption curves for copper and sulphur, each of which may be in error by 10%. Thus while the shape of the activation curve and therefore also of the cross-section curve is thought to be very well determined, the absolute values may be in error by as much as 20% with respect to the assumed copper activation value.

RESULTS

Half life

Of the over 300 sulphur irradiations carried out, the data of some 82 were plotted to yield decay curves. In each case, the decay was pure except for a very small fraction of longer 2.55 min. activity due to P^{30} formed by the reaction $S^{32}(\gamma, {}^{n}{}_{d}{}^{p})P^{30}$, the cross section for which has already been reported (10). The mean value of all half-life determinations is 2.66 ± 0.03 sec., a value which is in good agreement with that reported by McElhinney *et al.* (11), somewhat lower than that reported by Wäffler and Hirzel (15), and considerably lower than that indicated by the recent work of Boley and Zaffarano (2). A typical decay curve is shown in Fig. 8. The long-lived background in this case was ∽ 150 counts per minute, and hence the break in the curve does not appear.

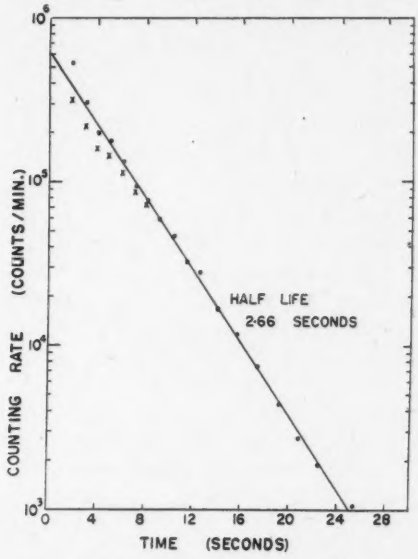

FIG. 8. A typical decay curve for S^{31}. The points marked with ×'s are those obtained before tube dead time corrections were applied.

Threshold

Using a power plot method of analysis after the manner of Parsons and Collie (12) and Sher, Halpern, and Mann (14), the initial portion of the activation curve was examined. The threshold was found to be 15.0 ± 0.1 Mev. This compares favorably with values published by McElhinney *et al.* (11) and by Becker, Hanson, and Diven (1).

Cross Section

The activation curve is similar in shape to other (γ–n) yield curves found in this laboratory. From the self-absorption work done, the ratio of the saturated

specific activity of S^{31} per atom S^{32} per 100 r. per min. to the saturated specific activity of Cu^{62} per atom Cu^{63} per 100 r. per min. was found to be 0.0585 at 22 Mev. The published value for the saturated specific activity of Cu^{62} per atom Cu^{63} per 100 r. per min. (6) after applying the 10% correction of Katz *et al.* (8) is 4.22×10^{-16} at 22 Mev. Hence the saturated specific activity of S^{31} per atom S^{32} per 100 r. per min. at 22 Mev. is 2.46×10^{-17}.

In Fig. 9 is shown the cross-section curve obtained from the activity curve by the photon difference method previously reported (7). The cross section shows the usual resonance shape with a peak value of 24.6 millibarns at 20.1 ± 0.5 Mev. The half width of the resonance peak is 4.5 Mev., and the integrated cross section $\int \sigma \, dE$ up to 24 Mev. is 0.12 Mev-barns.

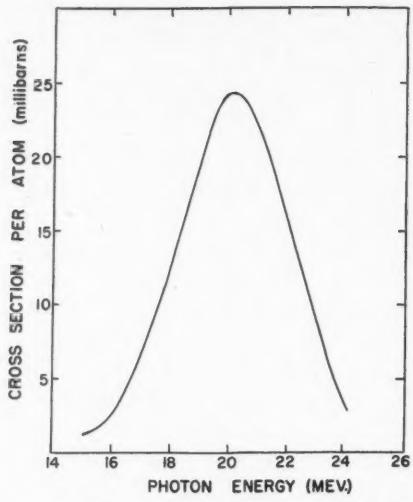

FIG. 9. The cross section for the reaction $S^{32}(\gamma, n)S^{31}$.

These values compare favorably with the data predicted empirically by Cameron and Katz (7, 3). Good agreement is obtained also with the neutron yield work of Price and Kerst (13). For $Z = 16$, their yield value is 1.4×10^5 neutrons per mole per r. at 22 Mev. Our results indicate a value of 1.5×10^5 neutrons per mole per r. at this energy.

CONCLUSIONS

With the apparatus described, the determination of the cross sections of many photonuclear reactions, previously impossible to measure because of the shortness of the half lives involved, can be carried out. In particular, included in this group are the reactions $Si^{28}(\gamma, n)Si^{27}$ and $Ca^{40}(\gamma, n)Ca^{39}$, investigation of which has already begun. In addition, $(\gamma, 2n)$ reactions in the light elements may be observed. Furthermore, with only slight changes to permit the use of a scintillation

counter to detect γ rays, many isomeric transitions in the middle-weight and heavy isotopes can be investigated.

The first results obtained using the apparatus yielded the cross section for the photoneutron process in S^{32} and a new value for the half life of S^{31}.

ACKNOWLEDGMENTS

The authors are indebted to Dr. H. E. Johns and Miss Sylvia Fedoruk for their work in designing the monitor circuit used. They also wish to acknowledge the many valuable suggestions offered by Dr. L. Katz. This work was supported through grants received from the National Research Council.

REFERENCES

1. Becker, R. A., Hanson, A. O., and Diven, B. C. Phys. Rev. 71: 466. 1947.
2. Boley, F. I. and Zaffarano, D. J. Phys. Rev. 84: 1059. 1951.
3. Cameron, A. G. W. Phys. Rev. 82: 272. 1951.
4. Feenberg, E. and Trigg, G. Revs. Modern Phys. 22:399. 1950.
5. Johns, H. E., Fedoruk, S. O., and Epp, E. R. Am. J. Roentgenol. (in press).
6. Johns, H. E., Katz, L., Douglas, R. A., and Haslam, R. N. H. Phys. Rev. 80:1062. 1950.
7. Katz, L. and Cameron, A. G. W. Can. J. Phys. 29:518. 1951.
8. Katz, L., Johns, H. E., Baker, R. G., Haslam, R. N. H., and Douglas, R. A. Phys. Rev. 82:271. 1951.
9. Katz, L., McNamara, A., Forsyth, P., Haslam, R. N. H., and Johns, H. E. Can. J. Research, A, 28:113. 1950.
10. Katz, L. and Penfold, A. S. Phys. Rev. 81:815. 1951.
11. McElhinney, J., Hanson, A. O., Becker, R. A., Duffield, R. B., and Diven, B. C. Phys. Rev. 75:542. 1949.
12. Parsons, R. W. and Collie, C. H. Proc. Phys. Soc. (London), A, 63:839. 1950.
13. Price, G. A. and Kerst, D. W. Phys. Rev. 77:806. 1950.
14. Sher, R., Halpern, J., and Mann, A. K. Private communication.
15. Wäffler, H. and Hirzel, O. Helv. Phys. Acta, 21:200. 1948.

NUCLEAR ELECTRIC QUADRUPOLE INTERACTION IN SINGLE CRYSTALS[1]

By G. M. Volkoff, H. E. Petch[2], and D. W. L. Smellie[3]

ABSTRACT

Pound's theory of the dependence of electric quadrupole splitting of nuclear magnetic resonance absorption lines in a single crystal on the orientation of the crystal in an external magnetic field is extended to cover the case of a crystal with nonaxially symmetric electric field gradient at the site of the nuclei being investigated. It is shown that an experimental study of the angular dependence of this splitting for three independent rotations of the crystal about any three mutually perpendicular axes will yield complete information about the orientation of the principal axes and the degree of axial asymmetry of the electric field gradient tensor at the site of the nuclei, and also will give the absolute value of the quadrupole coupling constant for those nuclei.

The authors' experiments on the splitting of the Li^7 absorption lines in a single crystal of $LiAl(SiO_3)_2$ (spodumene) are described and are used to illustrate the theory. The absolute value of the quadrupole coupling constant for the Li^7 nuclei in spodumene is found to be $|eQ\varphi_{zz}/h| = 75.7 \pm 0.5$ kc. per sec. The axial asymmetry parameter of the field gradient tensor at the site of the Li nuclei is found to be $\eta \equiv (\varphi_{xx} - \varphi_{yy})/\varphi_{zz} = 0.79 \pm 0.01$. One of the principal axes of this tensor (the y axis corresponding to the eigenvalue of intermediate magnitude) is experimentally found to coincide with the b crystallographic axis of monoclinic spodumene as required by the known symmetry of the crystal. The other two principal axes are in the ac plane, the z axis (corresponding to the eigenvalue φ_{zz} of greatest magnitude) lying between the a and c axes at an angle of $48° \pm 2°$ with the c axis.

1. INTRODUCTION

A study of the splitting of nuclear magnetic resonance absorption lines in single crystals by the interaction of the nuclear electric quadrupole moment eQ with the gradient $\nabla\mathbf{E}$ of the electric field existing in the crystal at the site of the nuclei in question yields information about both nuclei and crystals.

As examples of the type of information about nuclei made available by such studies we may mention the determination of the spin of Be^9 by Schuster and Pake (10), and the determination of the absolute value of the ratio of electric quadrupole moments of Li^6 and Li^7 by Schuster and Pake (9), and of Cu^{63} and Cu^{65} by Becker and Kruger (2) and Becker (1).

In this paper we discuss the information which is made available by this method about crystals, viz. the orientation of the principal axes and the degree of axial asymmetry of the field gradient tensor $\nabla\mathbf{E}$ at the site of the nuclei being investigated.

In addition to the above information about nuclei and about crystals separately one also obtains experimentally the absolute value of the quadrupole coupling constant which is the product of a nuclear property (eQ) and a crystal property (the largest in absolute value of the three eigenvalues of the tensor $\nabla\mathbf{E}$ at the site

[1] *Manuscript received February 22, 1952.*
Contribution from the Department of Physics, University of British Columbia, Vancouver, B.C. Work supported by grant from the National Research Council.
[2] *Holder of an Ontario Research Council Scholarship.*
[3] *Holder of a National Research Council of Canada Bursary. Now with the Dominion Gulf Company, Box 281, Larder Lake, Ont.*

of the nucleus). A knowledge of one of these two quantities from other sources will then permit the evaluation of the other one.

The observed splitting of any particular absorption line depends on the value of this quadrupole coupling constant, and on the orientation of the single crystal in the constant external magnetic field. Pound (7) has given the theory and has described experiments showing the influence of crystal orientation on the observed splitting in the special case of crystals in which the tensor $\nabla\mathbf{E}$ has an axis of symmetry.

The present paper deals with our extension of Pound's theory to cover the dependence of the resonance frequencies on the crystal orientation in the general case of crystals in which $\nabla\mathbf{E}$ need not necessarily have an axis of symmetry. The theory is then illustrated by our experimental determination of the dependence of the frequencies of the Li^7 absorption lines in a single crystal of spodumene ($LiAl(Si0_3)_2$) on the angles of rotation of the crystal about three mutually perpendicular axes. Preliminary results of our analysis of these rotations have been reported previously (11, 6). A simpler analysis is given here.

2. THEORY

A nucleus of spin I and magnetic moment μ placed in a constant uniform magnetic field H_0 has $2I + 1$ Zeeman levels with a constant energy difference $h\nu_0 = \mu H_0/I$. The $2I$ transitions between adjacent levels ($\Delta m = \pm 1$) under the influence of an external radio frequency magnetic field H_1 perpendicular to H_0 all correspond to a single resonance frequency ν_0, giving rise to a single absorption line.

If in addition the nucleus (with $I > \frac{1}{2}$) has a nonzero electric quadrupole moment eQ defined in the usual way, and is situated in an electric field with a nonvanishing gradient $\nabla\mathbf{E}$, then, as Pound (7) has shown, each of the Zeeman levels is perturbed, and the single absorption line of frequency ν_0 is split into $2I$ components.

In the case that the quadrupole coupling energy is small compared to the spacing of the Zeeman levels Pound (7) has shown that first order perturbation theory gives for the frequency of the transition between the perturbed Zeeman levels m and $m-1$ the value:

$$\nu(m \leftrightarrow m-1) = \nu_0 \pm K(\nabla E)'_0 = \nu_0 \pm \tfrac{1}{2}K\phi_{z'z'} \tag{1}$$

with

$$K = \frac{3eQ(2m-1)}{2I(2I-1)h}. \tag{2}$$

Here the sign is to be chosen opposite to the sign of the nuclear gyromagnetic ratio, and $\phi_{z'z'}$ is the second derivative of the electrostatic potential at the site of the nucleus in question, the z' direction coinciding with that of the constant magnetic field H_0. It is easily seen from Equation (1) that in this first order approximation the two resonance frequencies $\nu(m \leftrightarrow m-1)$ and $\nu(-(m-1) \leftrightarrow -m)$

lie equally spaced on opposite sides of ν_0, the frequency difference between them being given by twice their separation from the unperturbed line ν_0:

$$2\Delta\nu = 2K(\nabla E)_0' = K\phi_{z'z'}. \tag{3}$$

In order to have a large number of identical nuclei subject to the same H_0 and the same

$$(\nabla E)_0' = \phi_{z'z'}/2$$

so that each should have the same resonance frequencies determined by Equation (1), we consider a single crystal placed in a constant uniform magnetic field H_0. If a nucleus of the type under consideration occurs only once in each unit cell of the crystal, then it is guaranteed that the $(\nabla E)_0'$ (which is presumably due partly to the electrons in the atom containing the nucleus in question and the bonding electrons, and partly to the nuclei and the electrons of atoms at neighboring lattice points) is the same at the site of all such nuclei. If a nucleus of the type under investigation occurs more than once per unit cell, then in some cases the symmetry properties of the crystal may guarantee that $(\nabla E)_0'$ is the same for all the possible positions of the given nucleus in the unit cell. If the various possible positions in the unit cell are not equivalent in this sense, then the actual splitting observed will be a superposition of several splitting patterns due to the nuclei in each of the several nonequivalent positions. The analysis below is carried out explicitly for equivalent positions only.

If the orientation of the crystal is varied with respect to the constant magnetic field H_0 the value of $\phi_{z'z'}$ along H_0 will vary, and the observed splitting $2\Delta\nu$ will be a function of crystal orientation. Let eq denote the value of $\phi_{z'z'}$ for that particular crystal orientation which gives the greatest splitting. Then Equation (3) may be rewritten in the form

$$2\Delta\nu = K\phi_{z'z'} = \frac{3(2m-1)}{2I(2I-1)} \cdot \frac{e^2qQ}{h} \cdot \frac{\phi_{z'z'}}{eq}. \tag{3a}$$

Here the first factor depends on the spin I of the nucleus and on the particular components of the line being investigated, the second factor is the so-called quadrupole coupling constant, and the third dimensionless factor of absolute value not exceeding unity depends on the orientation of the crystal in the magnetic field. In order to determine the dependence of $2\Delta\nu$ on crystal orientation we first discuss the properties of the tensor ϕ_{ij} in a frame of reference fixed with respect to the crystal, and then show how $(\phi_{z'z'}/eq)$ depends on crystal orientation.

The tensor $\nabla\mathbf{E}$ written in rectangular coordinates (and also its negative, the tensor ϕ_{ij}) is symmetric (since $\nabla \times \mathbf{E} = 0$), and traceless (since $\nabla \cdot \mathbf{E} = 0$), and therefore has only five independent components. If we take an arbitrary externally easily identifiable set of right-handed rectangular axes XYZ fixed with respect to the crystal (for example this set may involve some of the crystallographic axes) the symmetric tensor ϕ_{ij} will have the general form

$$\begin{pmatrix} \phi_{XX} & \phi_{XY} & \phi_{ZX} \\ \phi_{XY} & \phi_{YY} & \phi_{YZ} \\ \phi_{ZX} & \phi_{YZ} & \phi_{ZZ} \end{pmatrix} \tag{4}$$

with five independent components since $\phi_{XX} + \phi_{YY} + \phi_{ZZ} = 0$. A set of axes xyz may be found to put this tensor in the diagonal form

$$\begin{pmatrix} -eq(1-\eta)/2 & 0 & 0 \\ 0 & -eq(1+\eta)/2 & 0 \\ 0 & 0 & eq \end{pmatrix}. \tag{5}$$

Here the axes have been so labeled that $\phi_{zz} = eq$ has the largest and $\phi_{xx} = -eq(1-\eta)/2$ the smallest absolute value, restricting the value of the axial asymmetry parameter $\eta = (\phi_{xx} - \phi_{yy})/\phi_{zz}$ to $0 \leqslant \eta \leqslant 1$. In the notation of Pound's paper (7):

$$\phi_{zz} = eq = \sum_j e_j(3\cos^2\theta_j - 1)r_j^{-3}. \tag{6}$$

The values of ϕ_{zz}, η, and of any three quantities (e.g. the three Eulerian angles, or any three independent ones of the nine direction cosines) specifying the orientation of the xyz system with respect to the XYZ system constitute five independent quantities defining the tensor.

Let X,Y,Z in turn be made perpendicular to the uniform external magnetic field H_0. In each case let the crystal be rotated about this axis which remains fixed in the (primed) laboratory system. Let the angle of rotation θ_X for the X rotation be measured from the position in which the Y axis coincides with H_0, which is chosen to define z' in the laboratory system. The other two directions x' and y' may be chosen in the case of the X rotation to make $x'y'z'$ coincide with the initial position of Z,X,Y. The transformation between XYZ and $x'y'z'$ is then given by:

$$\begin{aligned} X &= y' \\ Y &= \cos\theta_X z' + \sin\theta_X x' \\ Z &= -\sin\theta_X z' + \cos\theta_X x'. \end{aligned} \tag{7}$$

From Equation (7) it follows that

$$\begin{aligned} \phi_{z'z'} &= (\cos\theta_X \partial/\partial Y - \sin\theta_X \partial/\partial Z)^2 \phi \\ &= \tfrac{1}{2}(\phi_{YY} + \phi_{ZZ}) + \tfrac{1}{2}(\phi_{YY} - \phi_{ZZ})\cos 2\theta_X - \phi_{YZ}\sin 2\theta_X \end{aligned} \tag{8}$$

and consequently from Equation (3)

$$(2\Delta\nu)_X = A_X + B_X\cos 2\theta_X + C_X\sin 2\theta_X = A_X + (B_X^2 + C_X^2)^{\frac{1}{2}}\cos 2(\theta_X + \delta_X) \tag{9}$$

with

$$\begin{aligned} A_X &= \tfrac{1}{2}K(\phi_{YY} + \phi_{ZZ}) = -\tfrac{1}{2}K\phi_{XX}, \\ B_X &= \tfrac{1}{2}K(\phi_{YY} - \phi_{ZZ}), \\ C_X &= -K\phi_{YZ}. \end{aligned} \tag{10}$$

Similar relations for the Y and Z rotations may be obtained by cyclic permutation.

Pound's results in Reference (7) refer to the X rotation in the special case of a crystal with $\eta = 0$, and oriented so that the Y axis coincides with the z principal axis. In this case $\phi_{XX} = \phi_{ZZ} = -eq/2$, $\phi_{YY} = eq$, and the off-diagonal terms are zero, giving $A_X = K\,eq/4$, $B_X = 3\,K\,eq/4$, $C_X = 0$, and

$$(11)\quad 2\Delta\nu = Keq(3\cos^2\theta - 1)/2 = \frac{3(2m-1)}{2I(2I-1)} \cdot \left(\frac{e^2Qq}{h}\right) \cdot \frac{3\cos^2\theta - 1}{2}.$$

By performing the three rotations it is possible to determine from the three experimental curves of $2\Delta\nu$ as a function of θ the nine constants* A,B,C. It is clear from Equations (10) that the six A,B are not all independent, but satisfy the four independent identities:

$$(12)\qquad A_X + A_Y + A_Z = 0, \quad A_X + B_X = A_Z - B_Z,$$

plus two others obtained by cyclic permutation from the second one above. These identities are useful as a check on the experimental accuracy, and to fix the relative signs of the three curves.

From the nine experimental constants one may obtain with the aid of Equations (10):

$$(13)\qquad K\phi_{XX} = -2A_X = A_Y - B_Y = A_Z + B_Z, \quad K\phi_{YZ} = -C_X,$$

plus four more relations obtained by cyclic permutation.

The resulting tensor $K\phi_{ij}$ may be diagonalized in the usual way. The characteristic equation for the eigenvalues is the cubic equation:

$$(14)\qquad \gamma^3 - a\gamma - b = 0$$

where

$$(15)\quad \begin{aligned} a &= K^2[\phi_{XY}^2 + \phi_{YZ}^2 + \phi_{ZX}^2 - \phi_{XX}\phi_{YY} - \phi_{YY}\phi_{ZZ} - \phi_{ZZ}\phi_{XX}], \\ b &= K^3[\phi_{XX}\phi_{YY}\phi_{ZZ} + 2\phi_{XY}\phi_{YZ}\phi_{ZX} - \phi_{XX}\phi_{YZ}^2 - \phi_{YY}\phi_{ZX}^2 - \phi_{ZZ}\phi_{XY}^2]. \end{aligned}$$

A reversal of the undetermined common sign of A,B,C leaves a unchanged, but alters the sign of b, so that we may always choose $b = |b|$. The usual trigonometric solution of the cubic with three real roots gives:

$$(16)\qquad \gamma_n = 2(a/3)^{1/3}\cos[\alpha - 2\pi n/3] \qquad (n = 1,2,3)$$

with

$$(17)\qquad \cos 3\alpha = (|b|/2)(3/a)^{3/2}, \qquad 0 \leqslant \alpha \leqslant \pi/6.$$

γ_3 is positive and has the largest absolute value, the other two γ's are negative, and γ_1 has the smallest absolute value, so that in accordance with our convention we have, up to a common sign:

$$(18)\qquad \gamma_1 = K\phi_{xx}, \quad \gamma_2 = K\phi_{yy}, \quad \gamma_3 = K\phi_{zz}.$$

This leads to

$$(19)\qquad \eta \equiv (\phi_{xx} - \phi_{yy})/\phi_{zz} = (\gamma_1 - \gamma_2)/\gamma_3 = \sqrt{3}\tan\alpha.$$

$$(20)\qquad |K\phi_{zz}| = |Keq| = \gamma_3 = 2(a/3)^{\frac{1}{2}}\cos\alpha.$$

The absolute value of the quadrupole coupling constant is then given by:

$$(21)\qquad |e^2qQ/h| = |eQ\phi_{zz}/h| = [2I(2I-1)/3(2m-1)] \cdot |K\phi_{zz}|.$$

* *The relative signs of these nine constants are fixed by the experimental curves, but the absolute sign is not as long as there is no way of identifying which of the two resonance frequencies belongs to the $m \leftrightarrow m-1$, and which to the $-(m-1) \leftrightarrow -m$ transition. It might in principle be possible to make this assignment if the population of the levels could be appreciably altered by going to sufficiently low temperatures.*

The process of diagonalization also gives for the direction cosines of the principal axes x,y,z with respect to X,Y,Z:

$$\frac{\lambda_n}{D_{1n}} = \frac{\mu_n}{D_{2n}} = \frac{\nu_n}{D_{3n}} = \frac{\pm 1}{(D_{1n}^2 + D_{2n}^2 + D_{3n}^2)^{\frac{1}{2}}} \qquad (n = 1,2,3) \tag{22}$$

where

$$\begin{aligned} D_{1n} &= K^2\phi_{XY}\phi_{YZ} - K\phi_{ZX}(K\phi_{YY} - \gamma_n), \\ D_{2n} &= K^2\phi_{ZX}\phi_{XY} - K\phi_{YZ}(K\phi_{XX} - \gamma_n), \\ D_{3n} &= (K\phi_{XX} - \gamma_n)(K\phi_{YY} - \gamma_n) - K^2\phi_{XY}^2. \end{aligned} \tag{23}$$

The three values of γ_n lead to the direction cosines of the corresponding three principal axes. The relative signs of λ_n, μ_n, ν_n for each value of n are fixed by the relative signs of the D_{in}, but the absolute sign of each such set may be reversed by reversing the sign of the last term of Equation (22), corresponding to the fact that for a second rank tensor only the orientation of the principal axes is significant, but not the choice of the positive direction of each axis.

If desired, Equations (10) may be explicitly expressed in terms of these nine direction cosines, $|Keq|$ and η, as was done in our preliminary communication (6). However, the computational procedure outlined above is considerably simpler.

The largest splitting that may be obtained for any particular crystal will occur when the z principal axis is made to coincide with the magnetic field H_0. It is given by $2\Delta\nu = |Keq|$.

For a crystal with $\eta \neq 0$ and an unknown orientation of any of the principal axes of the field gradient tensor at the site of the nuclei being investigated the minimum number of readings required to completely determine this tensor is five: for instance $\theta_X = \theta_Y = \theta_Z = 45°$, and any two of $\theta_X = \theta_Y = \theta_Z = 0°$ will suffice. An increase in the number of crystal positions for which $2\Delta\nu$ is determined will increase the experimental accuracy with which the constants A,B,C and therefore the tensor $K\phi_{ij}$ is determined.

If from the symmetry of the crystal it is known that one of the X,Y,Z axes, say the X axis, coincides with one of the principal axes of the $\nabla\mathbf{E}$ tensor, then we must have $\phi_{ZX} = \phi_{XY} = 0$, so that $C_Y = C_Z = 0$, and the diagonalization remains to be performed only in the YZ subspace. In this case only one rotation about the X axis is necessary to give:

$$\begin{aligned} 2\Delta\nu &= A_X + B_X\cos 2\theta_X + C_X\sin 2\theta_X \\ &= A_X + (B_X^2 + C_X^2)^{\frac{1}{2}}\cos 2(\theta_X + \delta_X) \end{aligned} \tag{24}$$

with $\tan 2\delta_X = -C_X/B_X$ and the sign of δ_X opposite to that of C_X. The three diagonal terms of the $K\phi_{ij}$ tensor in its principal axes system are then given by:

$$-2A_X, \quad A_X \pm (B_X^2 + C_X^2)^{\frac{1}{2}}. \tag{25}$$

The principal axis corresponding to $-2A_X$ coincides with the X axis, while the other two principal axes lie in the YZ plane, the axis corresponding to the plus sign in the second expression (25) making an angle δ_X with the Y axis. The mini-

mum number of readings for a complete analysis in this case is three, say $\theta_X = 0°$, 45°, 90°. However, more θ_X readings, and also Y and Z rotations, will help to increase the accuracy attainable.

3. THE SPODUMENE CRYSTAL

We have checked the above theory experimentally in the case of the Li^7 resonance in a single crystal of $LiAl(SiO_3)_2$ (spodumene). Spodumene is a monoclinic pyroxene with diopside structure. Its space group is C^6_{2h}. It has four molecules

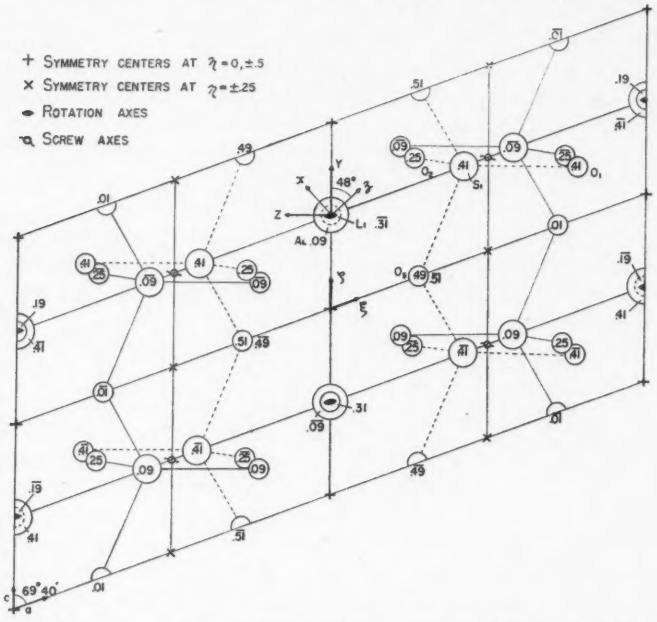

FIG. 1. Projection of a unit cell of monoclinic spodumene on the (010) plane. The b axis which is perpendicular to the page was used as the X rotation axis, and coincides with the y principal axis of the field gradient tensor at the Li sites. The Y and Z rotation axes, and the x and z principal axes of the field gradient tensor at the Li sites are shown in the diagram.

per unit cell. Fig. 1, based on the data of Warren and Biscoe (12), gives a projection of the structure on a (010) plane. The dimensions of the unit cell are:

$$a = 9.50 \text{ Å}, \quad b = 8.30 \text{ Å}, \quad c = 5.24 \text{ Å}, \quad \beta = 69°40'.$$

The atomic coordinates in decimal parts (ξ, η, ζ) of the axial lengths are given by:

$$\text{Li}(.00, -.31, .25), \text{Al}(.00, .09, .25), \text{Si}(.21, .41, .25),$$

$$O_1(.39, .41, .14), O_2(.13, .25, .32), O_3(.14, .49, .00).$$

Twofold rotation axes parallel to the b direction pass through the Li and Al positions at $\xi = 0, \pm .5, \zeta = \pm .25$. Twofold screw axes parallel to the b direction pass through $\xi = \pm .25, \zeta = \pm .25$. Symmetry centers lie at $\xi = 0,$

$\pm .5, \eta = 0, \pm .5, \zeta = 0, \pm .5$ and also at $\xi = \pm .25, \eta = \pm .25, \zeta = 0, \pm .5$. The crystal consists of -O-SiO_2-O-SiO_2-O- chains indicated by broken lines in Fig. 1 running parallel to the c direction and held together by Li and Al atoms.

Since both Li and Al nuclei lie on twofold rotation axes of the crystal, it follows that at the site of each such nucleus some one of the principal axes of the ϕ_{ij} tensor must coincide with the b direction. The existence of symmetry centers then shows that the other two axes must have the same orientation at the four Li sites (except for reversals of the positive axis directions which are immaterial for a second rank tensor), and also at the four Al sites, the latter, however, not necessarily being the same as at the Li sites. In Section 5 below it is experimentally determined that the y principal axis (corresponding to the eigenvalue of intermediate magnitude) of the ϕ_{ij} tensor at the Li sites coincides with the crystal b axis, while the x and z principal axes have the directions shown in Fig. 1.

Our sample was taken from a cleavage mass of spodumene which was milky colored and nontransparent, presumably owing to impurities. (A smaller transparent single crystal was used for some preliminary work (11) and gave results in agreement with the present ones.) A piece in the form of a rectangular prism based on a parallelogram was split off the large cleavage mass. Three of the four faces bounding the parallelogram were (110) cleavage planes, the edges formed by their intersection defining the direction of the c axis. The fourth face was ground down to give a crystal of convenient size. The bases were ground to planes perpendicular to the c axis (the right angle between the c axis and the ground base planes is believed to be accurate to about 1°). The b axis was then taken to lie in the plane of the base bisecting the parallelogram's obtuse angle ($2 \tan^{-1}(a \sin \beta/b) = 94°$) between two cleavage planes. It is believed that this direction could be identified to within perhaps two degrees. The spodumene crystal is very hard, and could not be marked with a sharp steel point, so a pencil mark was used. As the cleavage planes are not perfectly smooth there is some error introduced in bisecting the angle between them. Additional error comes from making settings on the rather thick pencil mark defining the b axis. The b direction was chosen as the externally easily recognizable X axis, the edge between the cleavage planes (c axis) as the Y axis, and the direction mutually perpendicular to the other two as the Z axis. Optical examination of our crystal showed that the crystallographic a axis lies between our Y and Z axes. The Y and Z axes are marked in Fig. 1. The dimensions of our crystal were approximately 8 by 10 mm. along the parallelogram sides, by 10 mm. along the c (or Y) axis.

4. APPARATUS AND EXPERIMENTAL PROCEDURE

The recording nuclear magnetic resonance spectrometer with an oscillating detector used in this work was designed and constructed by T. L. Collins (3). It is similar to the instrument described by Pound and Knight (8) but uses a different type of oscillating detector and lock-in detector. Fig. 2 shows a block diagram of the apparatus.

The electromagnet, with pole faces 6 in. in diameter and a gap of $1\frac{1}{2}$ in., is capable of producing flux densities up to 12,000 gauss. The pole faces were care-

fully machined with a rectangular ridge turned at the outside edge in order to make the field more uniform at the center of the magnet. A region near the center of the pole faces has an inhomogeneity of less than 0.2 gauss in 8000 gauss over

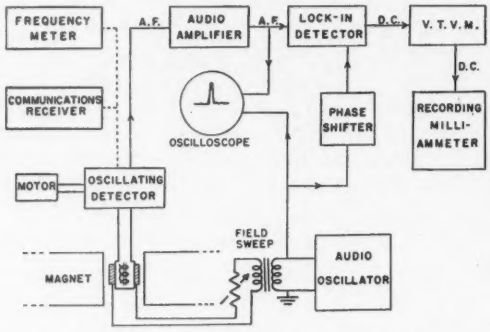

FIG. 2. Block diagram of the nuclear magnetic resonance spectrometer.

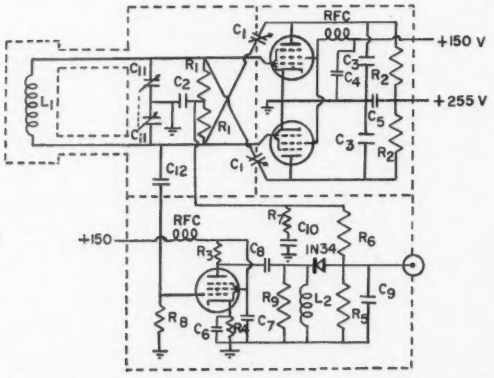

FIG. 3. Circuit diagram of the oscillating detector: $R_1 = 68$ K, $R_2 = 10$ K, $R_3 = 1.5$ K, $R_4 = 220\ \Omega$, $R_5 = 12$ K, $R_6 = 220$ K, $R_7 = 10$ K, $R_8 = 1$ meg., $R_9 = 1.2$ K, $C_1 = 2\text{-}7\mu\mu F$, $C_2 = 0.001\ \mu F$, $C_3 = 300\ \mu\mu F$, $C_4 = 0.01\ \mu F$, $C_5 = 0.01\ \mu F$, $C_6 = 0.005\ \mu F$, $C_7 = 0.002\ \mu F$, $C_8 = 0.001\ \mu F$, $C_9 = 0.001\ \mu F$, $C_{10} = 0.25\ \mu F$, $C_{11} = 140\ \mu\mu F$, $C_{12} = 20\mu\mu F$. L_1 tunes 9 − 17.5 Mc. per sec. L_2 resonates with 10 $\mu\mu F$ at 17 Mc. per sec.

the area of samples normally used (approx. 1 cm.^{2}). The electromagnet is supplied with electronically regulated current and in addition the magnetic field is itself further stabilized by a control voltage derived from a proton resonance signal as first suggested by Packard (5).

The oscillating detector, Fig. 3, consists of a pair of 6AG5's operating in "push-pull" in a Colpitts circuit. The tank coil containing the sample under investigation is placed between the poles of the electromagnet while the rest of the

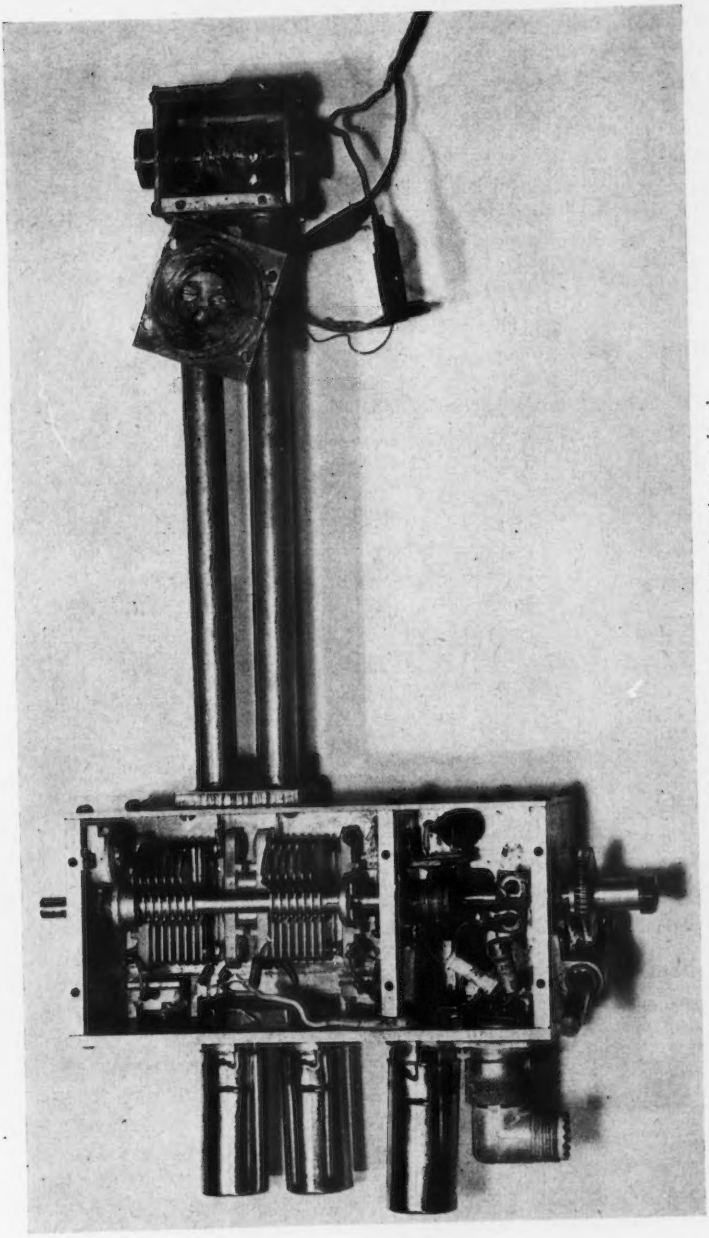

FIG. 4. Photograph of the oscillating detector head.

oscillator is assembled in a brass box outside the magnet. The oscillator's tuning condensers are driven by a synchronous motor and chain of reduction gears so that the frequency can be varied at the desired rate. (Actual rate used was in the neighborhood of 160 kc. per sec. per hr.) One stage of r-f. amplification is used before the crystal rectifier. An A.V.C. network feeds part of the d-c. rectified voltage back through an R.C. filter in such a way as to keep the level of oscillation very low. Thus the circuit will be extremely sensitive to small changes in the shunt resistance of the tank coil such as occur on passing through a nuclear resonance in the sample placed inside the coil. The r-f. voltage across the coil may be adjusted by varying the capacities C_1. Fig. 4 is a photograph of the oscillating detector head.

The large static magnetic field is modulated (by means of a pair of pancake field coils in the gap of the magnet) at 200 c.p.s. with a constant amplitude much smaller than the resonance line width. As the frequency of the oscillator slowly passes through a nuclear resonance, the level of oscillation is modulated with an amplitude which varies as the slope of the absorption curve, first in phase with

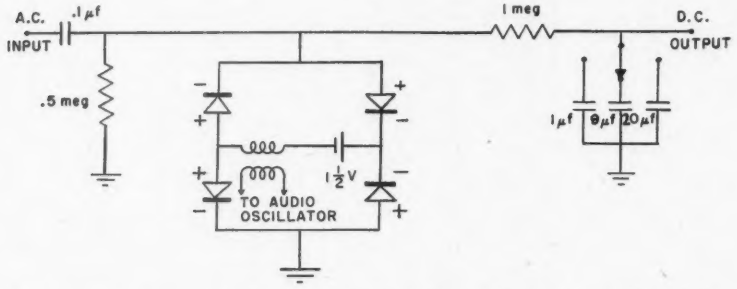

FIG. 5. Circuit diagram of the lock-in detector. Crystal rectifiers Sylvania Type 1N40.

the 200 c.p.s. modulation signal then reversing its phase at the center of the resonance line. The lock-in detector, Fig. 5, which is also fed the 200 c.p.s. modulation signal through an adjustable phase network, converts the amplified audio signal into a d-c. voltage which is approximately proportional to the first derivative of the resonance absorption line with respect to frequency. This derivative signal is recorded by a vacuum-tube voltmeter and recording milliammeter. Examples of such recorded absorption derivative curves are shown in Fig. 6. An R.C. filter circuit with adjustable time constant (ordinarily 9 sec.) precedes the V.T.V.M. The lock-in detector, Fig. 5, has a zero signal voltage of great stability, a necessary property where extended searches for unknown or poorly known resonances are involved.

Frequency measurements were made by means of a General Radio Type 620*A* Heterodyne Frequency Meter with the aid of a standard communications receiver. As the oscillator passed through zero beat with a series of settings of the frequency meter, markers were made on the recorder chart. Over the small

frequency ranges used, the sweep rate was linear and the splitting ($2\Delta\nu$) for well resolved resonances was measured directly from the recorder charts. For poorly

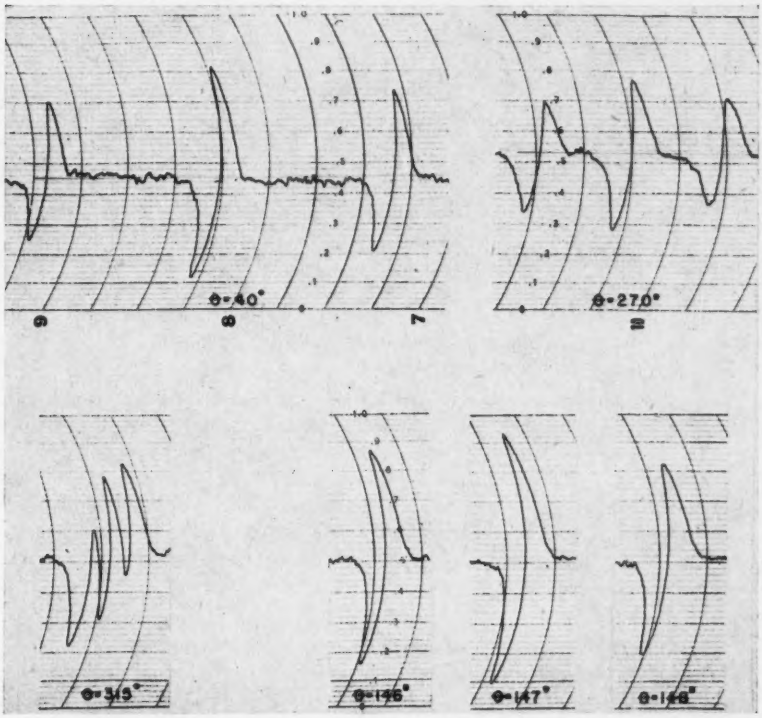

FIG. 6. Examples of recorded absorption derivative curves. The first three show selected splittings for the X rotation. The last three demonstrate the accuracy with which the position of zero splitting at $\theta_Y = 147°$ was determined for the Y rotation. A change of θ_Y by $\pm 1°$ produces a marked decrease in the maximum of the derivative curve. The sweep rate in all cases is 10 kc. per sec. per division.

resolved and unresolved resonances the composite derivative curve was graphically broken up into its three component derivative curves and the splitting estimated from these.

The crystal mount, Fig. 7, locks tightly between the ridges of the pole faces so that the axis of rotation is perpendicular to the magnetic field. The dial is calibrated in one-degree intervals and relative measurements can be repeated consistently to better than half a degree. The two chief crystal position errors arise first in determining the crystal axes, and secondly in aligning the crystal axes with respect to the axis of rotation, and to the magnetic field H_0.

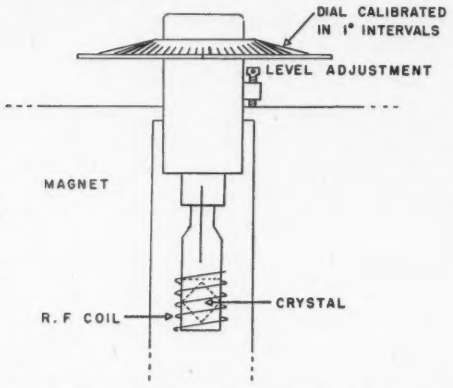

FIG. 7. Diagram of the crystal mount (not to scale).

Using the above apparatus we have studied the splitting of the Li^7 resonance line in spodumene as a function of crystal orientation. The spin of Li^7 is $I = 3/2$, so that its resonance line breaks up into $2I = 3$ components as shown in Fig. 6. The central component ($m = \frac{1}{2} \leftrightarrow -\frac{1}{2}$) corresponds to the unperturbed frequency $\nu_0 = \mu H_0/Ih$. Our measurements were made in a magnetic field of approximately $H_0 = 7190$ gauss calculated from the known value of the Li^7 gyromagnetic ratio and the measured value of $\nu_0 = 11.90$ Mc. per sec. The frequency difference $2\Delta\nu$ between the two outer components ($m = 3/2 \leftrightarrow 1/2,\ -1/2 \leftrightarrow -3/2$) of the absorption line was measured as a function of the angle of rotation of the crystal about the three orthogonal XYZ axes each in turn kept perpendicular to the magnetic field H_0.

To verify that the observed splitting $2\Delta\nu$ is actually independent of the values of H_0 and ν_0 as required by Equation (3*a*) a series of measurements was taken for one particular crystal position ($\theta_X = 40°$) which gave a large value of $2\Delta\nu$ in magnetic fields varying over the range of 6500 to 8000 gauss. The observed frequency difference $2\Delta\nu$ remained constant well within our experimental error of about 1 kc. per sec.

5. RESULTS

Figs. 8, 9, and 10 represent (up to a possible common minus sign) the frequency difference $2\Delta\nu$ between the two outer components of the Li^7 line in spodumene as a function of θ for the X,Y,Z rotations about the b and c axes and the third perpendicular direction respectively. Each circled point in these figures corresponds to a recorded absorption derivative curve of the type shown in Fig. 6. The crystal position could in each case be determined to better than half a degree with respect to the zero on the crystal mount scale. However, a somewhat larger error could have been made in aligning the zero of the scale with respect to the magnetic field H_0 and also with respect to the crystallographic axes, in view of the difficulty mentioned in Section 3 of precisely locating and marking the direction of the axes, particularly of the b axis. The frequency difference could in each case

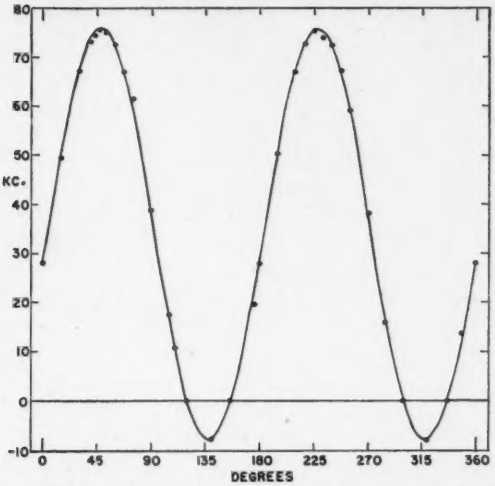

FIG. 8. Frequency difference between the two outer components of the Li^7 line for the X rotation about the b axis of spodumene. The circles are the experimental points. The solid curve represents $(2\Delta\nu)_X = 34.0 + 41.8 \cos 2(\theta_X - 48°)$. $\theta_X = 0$ when the c axis of spodumene coincides with the magnetic field H_0. The 48° phase shift indicates that the z principal axis, which corresponds to the maximum possible splitting, makes that angle with the c axis.

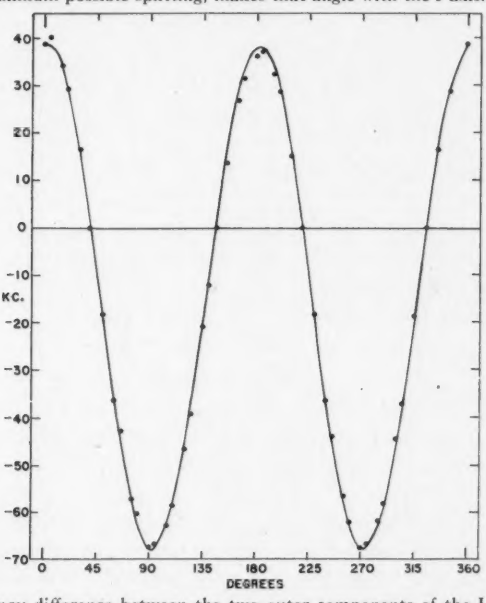

FIG. 9. Frequency difference between the two outer components of the Li^7 line for the Y rotation about the c axis of spodumene. The circles are the experimental points. The solid curve represents $(2\Delta\nu)_X = -14.8 + 53.2 \cos 2(\theta_Y - 3°)$. $\theta_Y = 0$ was meant to mark the position of the crystal when the b axis is at 90° to the magnetic field H_0, but the 3° phase shift shows a small alignment error.

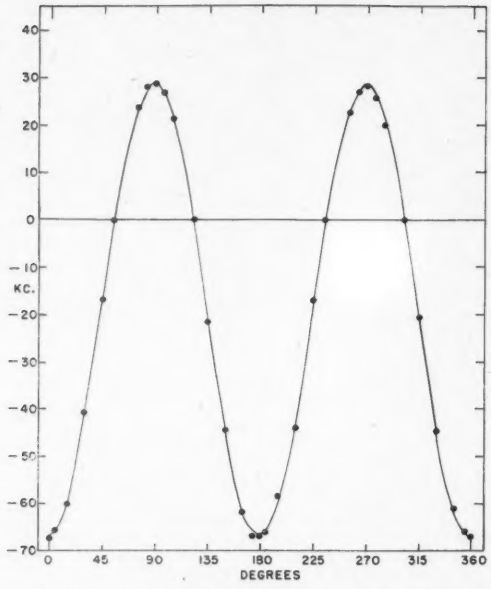

FIG. 10. Frequency difference between the two outer components of the Li^7 line for the Z rotation about the direction orthogonal to the b and c axes of spodumene. The circles are the experimental points. The solid curve represents $(2\Delta\nu)_Z = -19.2 - 47.8\cos 2(\theta_Z + 1°)$. $\theta_Z = 0$ was meant to mark the position of the crystal when the b axis coincides with the magnetic field H_0 but the 1° phase shift shows a small alignment error.

be measured to somewhat better than 1 kc. per sec. Curves of the theoretically expected form $A + D \cos 2(\theta + \delta)$ given by Equation (9) were fitted to the experimental points graphically, as for the purposes of this paper it was not considered worth-while to expend the effort for a least squares fit. The solid curves in Figs. 8-10 are given respectively by:

$$\begin{aligned} (2\Delta\nu)_X &= \quad 34.0 + 41.8 \cos 2(\theta_X - 48°), \\ (2\Delta\nu)_Y &= -14.8 + 53.2 \cos 2(\theta_Y - 3°), \\ (2\Delta\nu)_Z &= -19.2 - 47.8 \cos 2(\theta_Z + 1°), \end{aligned} \tag{26}$$

where the constants A and D are in kilocycles per second. Our rough estimate of the errors, based on graphical fitting of the curves, is that the A and D constants are accurate to about half a kilocycle per second and the phase angles δ (with respect to the zero of the scale) to about half a degree.

Only three components of the absorption line appear in each of the three rotations, with the dependence of the frequency splitting $2\Delta\nu$ between the two outer components being given in each case by curves (26) of the expected form (9). This corroborates the deduction made in Section 3 on the basis of the known symmetry properties of spodumene that the field gradient tensor has the same eigenvalues and principal axes at all four Li sites in the unit cell.

The discussion of symmetry properties of spodumene in Section 3 showed that the twofold symmetry axis in the b direction must be one of the principal axes of the ϕ_{ij} tensor at the sites of the Li nuclei. Consequently if we had succeeded both in precisely identifying and marking the b axis, and also in making it coincide with H_0 for $\theta_Y = -90°$, and for $\theta_Z = 0°$, we should have obtained zero phase angles δ for the Y and Z rotations in Equations (26). The small deviations of δ_Y and δ_Z from zero indicate the presence of one or both of these errors: (1) the crystallographic axes were properly identified, but an error was made in lining them up with respect to the axis of rotation of the crystal mount and the magnetic field H_0, or (2) the X,Y,Z, axes as actually picked out were lined up properly with respect to the crystal mount and the magnetic field, but did not quite coincide with the b and c crystallographic axes and the third perpendicular direction.

The analysis of the results will differ slightly depending on which of the above two sources of error is assumed to be the dominant one. In Case (1) we assume that the b axis was properly identified. Then the $-3°$ and $1°$ phase angles indicate that errors of that magnitude were made in determining the reference positions of the crystal in which the b axis is supposed to be perpendicular to H_0 for $\theta_Y = 0°$, and along H_0 for $\theta_Z = 0°$. To compensate for these errors we merely shift the zeros of the θ_Y and θ_Z scales to make $\delta_Y = \delta_Z = 0°$ in Equation (26). The phase angle $\delta_X = -48°$ can presumably also be in error by a comparable amount but we have no direct indication as to the possible magnitude and sign of this error. We then obtain the following set of constants (in kc. per sec.) for Equations (9):

$$\begin{array}{lll} A_X = 34.0, & B_X = -4.7, & C_X = 41.6, \\ A_Y = -14.8, & B_Y = 53.2, & C_Y = 0, \\ A_Z = -19.2, & B_Z = -47.8, & C_Z = 0. \end{array} \tag{27}$$

The consistency of the set of six constants A,B above may be checked with the aid of Identities (12). Since from these identities the three quantities:

$$A_X = 34.0, \quad (B_Y - A_Y)/2 = 34.0, \quad -(B_Z + A_Z)/2 = 33.5$$

and also the three quantities:

$$B_X = -4.7, \quad -(3A_Y + B_Y)/2 = -4.4, \quad (3A_Z - B_Z)/2 = -4.9$$

should be equal, we choose the average values $A_X = 33.8$, $B_X = -4.7$. The spread of the values obtained from the three rotations is within our estimate of half a kilocycle per second error for the individual constants. Using these averages and $C_X = 41.6$ in Equations (25) we obtain the following results. The three eigenvalues of the $K\phi_{ij}$ tensor (up to a common sign) are:

$$K\phi_{zz} = -7.9, \quad K\phi_{yy} = -67.6, \quad K\phi_{zz} = 75.7.$$

The y axis lies along the b (or X) axis and the x and z axes lie in the ac (or YZ) plane with the z axis making an angle $\delta_X = -48°$ with the c (or Y) axis, as

shown in Fig. 1. The values of the axial asymmetry parameter η and of the magnitude of the quadrupole coupling constant are:

$$(28) \qquad \eta = (\phi_{xx} - \phi_{yy})/\phi_{zz} = 0.789, \quad |e^2qQ/h| = |K\phi_{zz}| = 75.7 \text{ kc./sec.}$$

In Case (2) we assume that the error lies principally in the identification of the position of the crystallographic axes, and that there is no error in aligning the chosen XYZ directions with respect to the crystal mount and the magnetic field. In this case Equations (26) should be used as they stand. The $-3°$ and $1°$ phase angles in Equations (26) indicate that an error of approximately $3°$ has been made in locating the b axis in the plane perpendicular to the c axis, and an error of approximately $1°$ has been made in locating the b axis in the bc plane. The following set of A,B,C (in kc. per sec.) is obtained from Equations (26):

$$(29) \qquad \begin{array}{lll} A_X = \ 34.0, & B_X = -\ 4.7, & C_X = 41.6, \\ A_Y = -\ 14.8, & B_Y = \ 53.0, & C_Y = \ 5.4, \\ A_Z = -\ 19.2, & B_Z = -\ 47.8, & C_Z = \ 1.9. \end{array}$$

The relative signs of these nine quantities are determined by the experiment, but not the absolute signs. The above values of A and B lead, in accordance with Equations (13), to the following alternative expressions for the diagonal terms of the tensor $K\phi_{ij}$:

$K\phi_{XX}$	$K\phi_{YY}$	$K\phi_{ZZ}$
$-2A_X = -68.0$	$-2A_Y = 29.6$	$-2A_Z = 38.4$
$A_Y - B_Y = -67.8$	$A_Z - B_Z = 28.6$	$A_X - B_X = 38.7$
$A_Z + B_Z = -67.0$	$A_X + B_X = 29.3$	$A_Y + B_Y = 38.2.$

The spread of values in each column is consistent with our estimated error of about half a kilocycle per second for the individual constants. Averaging the three columns we obtain:

$$K\phi_{XX} = -67.6, \quad K\phi_{YY} = 29.2, \quad K\phi_{ZZ} = 38.4$$

which add up to zero as required. From the C's and Equation (13) we have for the off-diagonal terms:

$$K\phi_{YZ} = -41.6, \quad K\phi_{ZX} = -5.4, \quad K\phi_{XY} = -1.9.$$

The process of diagonalization outlined in Equations (15) to (21) of Section 2 gives:

$$(30) \qquad \begin{array}{lll} a = 5.21 \times 10^3, & b = 3.93 \times 10^4, & \alpha = 24°25', \\ \eta = 0.798, & |e^2qQ/h| = 75.7 \text{ kc./sec.} & \end{array}$$

Substituting the three values of γ_n ($n = 1,2,3$) from Equations (16) and (18) into Equations (23) we obtain from Equations (22) the three sets of direction cosines λ_n, μ_n, ν_n each set defining the direction of one of the principal axes x,y,z, with respect to the rotation axes X,Y,Z. These direction cosines are:

$$(31) \qquad \begin{array}{llll} \lambda_1 = -.083, & \lambda_2 = .996, & \lambda_3 = \ .019, \\ \mu_1 = \ .744, & \mu_2 = .050, & \mu_3 = \ .666, \\ \nu_1 = \ .663, & \nu_2 = .070, & \nu_3 = -.746. \end{array}$$

Here only the relative signs within each set λ_n, μ_n, ν_n are significant, as the absolute signs defining the positive directions of the principal axes are immaterial for a second rank tensor. The deviations of λ_2 from unity and of λ_1, λ_3, μ_2, ν_2 from zero correspond to the deviation of the actual direction of the y principal axis from that of the X rotation axis, which was meant to coincide with the crystallographic b axis. This small deviation is within our experimental error of identifying the b axis, and is consistent with the symmetry requirement that the b axis should coincide with one of the principal axes. The other four cosines μ_1,ν_1, μ_3,ν_3 indicate that the z,x axes are rotated away from the YZ axes through an angle $\delta_X = -48°$.

Combining the results of our two alternative analyses given by Equations (28), (30), and (31) we conclude finally that the y principal axis coincides with the b axis, and that:

(32) $|e^2qQ/h| = 75.7 \pm 0.5$ kc./sec., $\eta = 0.79 \pm 0.01$, $\delta_X = -48° \pm 2°$.

The uncertainties shown are our estimates of our limits of error.

6. DISCUSSION

Our measurements confirm within experimental error the only available theoretical results about the field gradient tensor at the Li sites in spodumene: the field gradient tensor is the same at the four Li sites in the unit cell, and one of the principal axes of this tensor does coincide with the b twofold axis of symmetry. Our other experimental results, i.e. the determination of which particular principal axis coincides with the b axis, the orientation of the other two principal axes, the degree of axial asymmetry of this tensor, and the absolute value of the quadrupole coupling constant for Li in spodumene, have at present no theoretical counterparts with which they might be compared. To our knowledge this represents the first complete experimental analysis of the field gradient tensor at a nuclear site in a single crystal in the general case of axial asymmetry.

The following possible applications of the technique outlined in this paper suggest themselves. From the point of view of crystal physics it is of interest to learn as much as possible about all the properties of the field gradient tensor at the nuclear sites. From the point of view of nuclear physics it is of particular interest to obtain by calculation, or otherwise, the largest eigenvalue $|\phi_{zz}|$ of this tensor for with its aid the magnitude $|eQ|$ of the nuclear quadrupole moment could be determined from the experimental absolute value of the quadrupole coupling constant $|eQ\phi_{zz}/h|$.

Presumably the tensor ϕ_{ij} at a nuclear site can be broken up into two contributions: a "local" one arising from the atomic and bonding electrons in the immediate vicinity of a given nucleus, and a "distant" one arising from charge distributions at other lattice points. The calculation of the former would require a detailed knowledge of the electronic wave functions. The latter might perhaps be easier to estimate, for it might turn out that sufficient accuracy is attained by replacing the atoms at more distant lattice points by equivalent point charges. At present it does not seem to be definitely known as to which is the predominant

contribution. If one succeeded in obtaining a theoretical estimate of only the "distant" contribution to ϕ_{ij} in some crystal it would be interesting to compare the theoretical value of the asymmetry parameter η and the principal axes orientation of this "distant" contribution with the experimentally observed ones. A marked discrepancy between the two would definitely indicate that the "local" contribution predominates. Alternatively, two isomorphic crystals in which, say, only Li is replaced by Na, everything else remaining the same, could be experimentally compared to each other. A marked difference in the two values of η and in the orientations of the principal axes at the Li and Na sites would again indicate the importance of the "local" as against the "distant" contributions to ϕ_{ij}.

If one succeeded in theoretically estimating both the "local" and the "distant" contributions to ϕ_{ij} in some crystal, greater confidence could be placed in the theoretical estimate of the largest eigenvalue $|\phi_{zz}|$ if the calculated value of η and the principal axes orientation could be checked directly experimentally. Such a calculated value of $|\phi_{zz}|$ could then be used to obtain $|eQ|$ from the quadrupole coupling constant $|eQ\phi_{zz}/h|$.

As long as a theoretical estimate of the largest eigenvalue $|\phi_{zz}|$ is unavailable one can only obtain ratios of the magnitudes of the quadrupole moments of two nuclei. When comparing two isotopes of the same element in the same crystal (e.g. Li^6 and Li^7 in Reference (9), or Cu^{63} and Cu^{65} in References (1) and (2)) one presumes that ϕ_{zz} is the same for both isotopes, and compares the observed splittings for the two isotopes. It is advantageous to have these splittings as large as possible, and the method of this paper enables one to determine uniquely the position of the crystal which will give the maximum splitting. The ratio of the magnitudes of eQ for two different elements may be approximately obtained by assuming (as Hatton, Rollin, and Seymour (4) have done for Be^9 and Al^{27} in beryl) that the largest eigenvalue ϕ_{zz} is approximately the same at the sites of the two different but somewhat similarly situated nuclei. One would have greater confidence in this assumption if in the case of a nonaxially symmetric ϕ_{ij} it could be shown that the value of η and the principal axes orientation are roughly the same at the sites of the two kinds of nuclei.

7. ACKNOWLEDGMENTS

The authors would like to express their thanks to Mr. J. F. Brydle, and Mr. A. J. Fraser of the Physics Department machine shop for their help in constructing parts of the apparatus, to Dr. K. C. McTaggart and Dr. R. M. Thompson of the Geology Department, U.B.C., for their advice and aid in identifying the crystal axes, to Mr. J. A. Donnan of the same department for aid in grinding the crystal, and to the Geology Department, U.C.L.A., for providing a large spodumene sample. This work was made possible by continuing financial support from the National Research Council. One of the authors (H. E. P.) held a Scholarship from the Research Council of Ontario, and another (D. W. L. S.) held a Bursary from the National Research Council of Canada.

REFERENCES

1. BECKER, G. Z. Physik, 130:457. 1951.
2. BECKER, G. and KRUGER, H. Naturwissenschaften, 38:121. 1951.
3. COLLINS, T. L. Ph.D. Thesis, University of British Columbia, Vancouver, B.C. 1950.
4. HATTON, J., ROLLIN, B. V., and SEYMOUR, E. F. W. Phys. Rev. 83:672. 1951.
5. PACKARD, M. Rev. Sci. Instruments, 19:435. 1948.
6. PETCH, H. E., SMELLIE, D. W., and VOLKOFF, G. M. Phys. Rev. 84:602. 1951.
7. POUND, R. V. Phys. Rev. 79:685. 1950.
8. POUND, R. V. and KNIGHT, W. D. Rev. Sci. Instruments, 21:219. 1950.
9. SCHUSTER, N. A. and PAKE, G. E. Phys. Rev. 81:157. 1951.
10. SCHUSTER, N. A. and PAKE, G. E. Phys. Rev. 81:886. 1951.
11. SMELLIE, D. W. and PETCH, H. E. Phys. Rev. 83:891. 1951.
12. WARREN, B. E. and BISCOE, J. Z. Krist. 80:391. 1931.

CANADIAN JOURNAL OF PHYSICS

Notice to Contributors

GENERAL: Manuscripts should be typewritten, double spaced, and the **original and one extra copy** submitted. Style, arrangement, spelling, and abbreviations should conform to the usage of this Journal. Names of all simple compounds, rather than their formulas, should be used in the text. Greek letters or unusual signs should be written plainly or explained by marginal notes. Superscripts and subscripts must be legible and carefully placed. Manuscripts should be carefully checked before being submitted, to reduce the need for changes after the type has been set. If authors require changes to be made after the type is set, they will be charged for changes that are considered to be excessive. **All pages, whether text, figures, or tables, should be numbered.**

ABSTRACT: **An abstract of not more than about 200 words, indicating the scope of the work and the principal findings, is required.**

ILLUSTRATIONS:

(i) *Line Drawings:* All lines should be of sufficient thickness to reproduce well. Drawings should be carefully made with India ink on white drawing paper, blue tracing linen, or co-ordinate paper **ruled in blue only**; any co-ordinate lines that are to appear in the reproduction should be ruled in black ink. Paper ruled in **green, yellow, or red should not be used** unless it is desired to have all the co-ordinate lines show. Lettering and numerals should be neatly done in India ink preferably with a stencil (**do not use typewriting**) and be of such size that they will be legible and not less than one millimeter in height when reproduced in a cut three inches wide. All experimental points should be carefully drawn with instruments. Illustrations need not be more than two or three times the size of the desired reproduction, but the ratio of height to width should conform with that of the type page. **The original drawings and one set of small but clear photographic copies are to be submitted.**

(ii) *Photographs:* Prints should be made on glossy paper, with strong contrasts; they should be trimmed to remove all extraneous material so that essential features only are shown. Photographs should be submitted **in duplicate**; if they are to be reproduced in groups, one set should be so arranged and mounted on cardboard with rubber cement; the duplicate set should be unmounted.

(iii) *General:* **The author's name, title of paper, and figure number should be written in the lower left hand corner (outside the illustration proper) of the sheets on which the illustrations appear.** Captions should not be written on the illustrations, but typed together at the end of the manuscript. All figures (including each figure of the plates) should be numbered consecutively from 1 up (arabic numerals). **Each figure should be referred to in the text.** If authors desire to alter a cut, they will be charged for the new cut.

TABLES: Each table should be typed on a separate sheet. Titles should be given for all tables, which should be numbered in Roman numerals. Column heads should be brief and textual matter in tables confined to a minimum. **Each table should be referred to in the text.**

REFERENCES: **These should be listed alphabetically by authors' names, numbered in that order, and placed at the end of the paper.** The form of literature citation should be that used in this Journal. **Titles of papers should not be given.** The first page only of the references cited should be given. **All citations should be checked with the original articles.** Each citation should be referred to in the text by means of the key number.

REPRINTS: A total of 50 reprints of each paper, without covers, are supplied free to the authors. Additional reprints will be supplied according to a prescribed schedule of charges. On request, covers can be supplied at cost.

Approximate charges for reprints may be calculated from the number of printed pages, obtained by multiplying by 0.6 the number of manuscript pages (double-spaced typewritten sheets, 8½ in. by 11 in.) and making allowance for space occupied by line drawings and half-tones (not inserts). The cost per page is tabulated at the back of the reprint request form sent with the galley.

Contents

Page

Gamma-Neutron Reactions in O^{16} and N^{14}—*R. J. Horsley, R. N. H. Haslam, and H. E. Johns* - - - - - - - - - - - 159

Fluorescent Spectra of Some Organic Solid Solutions—*F. R. Lipsett and A. J. Dekker* - - - - - - - - - - - - - 165

Surface Losses in Electromagnetic Cavity Resonators—*I. Paghis* - 174

Forbidden Transitions in Diatomic Molecules. II. The $^3\Sigma_u^+ \leftarrow {}^3\Sigma_g^-$ Absorption Bands of the Oxygen Molecule—*G. Herzberg* - - 185

Symmetrically Placed Inductive Posts in Rectangular Wave Guide —*H. Gruenberg* - - - - - - - - - - - - - - 211

The Dynamical Theory of Magnetic Monopoles—*S. Shanmugadhasan* - - - - - - - - - - - - - - - - 218

Spinors in the Dynamical Theory of Spinning Particles—*S. Shanmugadhasan* - - - - - - - - - - - - - - - 226

Ballons de Matière Plastique Fabriqués par un Nouveau Procédé— *Pierre Demers et Jean-Louis De Grandpré* - - - - - - 235

Transformation Amplitudes for Vector Addition of Angular Momentum; $(j3mm' | j3JM)$—*D. L. Falkoff, G. S. Colladay, and R. E. Sells* - - - - - - - - - - - - - - - 253

The Measurement of Photonuclear Cross Sections in Isotopes Leading to Short-lived Decay Products—*R. N. H. Haslam, R. G. Summers-Gill, and E. H. Crosby* - - - - - - - 257

Nuclear Electric Quadrupole Interaction in Single Crystals— *G. M. Volkoff, H. E. Petch, and D. W. L. Smellie* - - - 270

Printed in Canada *by* University of Toronto Press